7-2018

MULTI-OBJECTIVE DESIGN OPTIMIZATION OF REVERSE TOTAL SHOULDER ARTHROPLASTY TO MAXIMIZE RANGE OF MOTION AND JOINT STABILITY

Josie A. Elwell
Binghamton University--SUNY, jelwell3@binghamton.edu

MULTI-OBJECTIVE DESIGN OPTIMIZATION OF REVERSE TOTAL SHOULDER ARTHROPLASTY TO MAXIMIZE RANGE OF MOTION AND JOINT STABILITY

BY

JOSIE ELWELL

BS, Binghamton University, 2013

DISSERTATION

Submitted in partial fulfillment of the requirements for
the degree of Doctor of Philosophy in Mechanical Engineering
in the Graduate School of
Binghamton University
State University of New York
2018

Accepted in partial fulfillment of the requirements for
the degree of Doctor of Philosophy in Mechanical Engineering
in the Graduate School of
Binghamton University
State University of New York
2018

July 17, 2018

Roy TR McGrann, Chair
Department of Mechanical Engineering, Binghamton University

Ryan Willing, Faculty Advisor
Department of Mechanical Engineering, Binghamton University

Frank Cardullo, Member
Department of Mechanical Engineering, Binghamton University

Joseph Choi, Member
Department of Orthopaedic Surgery, Guthrie

Nagen Nagarur, Outside Examiner
Department of Systems Science and Industrial Engineering, Binghamton University

ACKNOWLEDGMENTS

I would first like to thank Dr. Ryan Willing. I could not have asked for a better advisor and mentor. Your support and guidance have been absolutely invaluable to me over these last few years. You have encouraged me to always ask more questions and look for more answers and my interest in research has only grown from the time you first agreed to be my advisor. I can't thank you enough for all the time you spent teaching me. From learning how to find the right button in a program (after I spent hours looking and you would find it in 2 minutes), to all the reminders to stay out of the weeds, your knowledge, experience, and commitment to your research and your students is inspiring.

I would also like to thank my lab mates, Melissa, Danial, Vishnu, and Chaochao. Having you guys around every day always made things easier, whether it was to vent, solve problems together, practice presentations, or just talk about life to escape research for a few minutes. I've enjoyed working with you all and wish you all the best in the future. On that note, I'd also like to thank all the faculty and staff in the Mechanical Engineering Department and Engineering Design Division at BU. You all helped make BU a place I was happy to be for nine years.

To all of my friends, thank you. From getting beers after a long day, to going on adventures and making memories I'll never forget, you were all apart of helping survive grad school. Sarah, thanks for dealing with me in the few months leading up to finishing school and always reminding me that there was a light at the end of the tunnel.

And finally, thank you to my family. Mom, Dad, Ritchie, and Jesse, I can say for sure that I would not be where I am today without you all and I'm not sure thank you will ever be enough. Mom, thanks for, well…everything, because that's what you have been to me. Dad, there's much more, but thanks specifically for all the science lessons and helping me find my passion. Ritchie, thanks for always being my partner in crime. Jesse, you're the best role model I could have asked for, even when that meant dying my hair crazy colors as a teenager, just because I wanted to be like you. To all my aunts, uncles, cousins, and grandparents, you guys are the best. Thank you for all your support and pushing me to finish just by asking the question "So, when are you going to be done with school?" To answer that, I am finally done with school, and will be forever grateful for everyone that got me here.

ABSTRACT

Reverse total shoulder arthroplasty was developed to restore range of motion (ROM) and joint stability to patients with pre-operative conditions that are not addressed by conventional replacements. Although reverse total shoulder arthroplasty is the current gold standard for treating a range of indications, the effects of varying its design on functional outcomes of the procedure are still not well understood.

To that end, it is not yet clear which configurations, in terms of both design and surgical placement parameters, maximize range of motion and stability of the joint. It was hypothesized that there is trade-off between the two. These types of relationships may be elucidated using multi-objective design optimization to generate a Pareto front. Pareto optimal points represent those where neither performance metric can be further improved without detriment to the other.

Multi-objective optimization requires 1) metrics to characterize the objectives to be optimized and 2) an automated computational framework capable of assessing the metrics for any candidate implant design. As such, the pre-cursory goals to performing multi-objective optimization involved the development, validation, and automation of computational tools to predict the performance of reverse should designs with respect to range of motion and joint stability.

Characterization of the Pareto front with multi-objective optimization confirmed that there is in fact a trade-off between range of motion and stability. Designs that maximize one functional outcome differ from those that maximize the other. Designs that resulted in

intermediate performance in terms of both objectives were variable. This indicates that functional factors other than range of motion and stability, such as mechanical implant stability (fixation) and avoidance of inferior impingement, could serve as deciding factors between implant configurations that achieve similar range of motion and stability results.

Table of Contents

List of Tables

List of Figures

List of Abbreviations

ADL: Activities of daily living
COR: Center of rotation
COR_{inf}: Inferior offset of center of rotation
CTA: Cuff tear arthropathy
DOF: Degree of freedom
FE: Finite element
FTD: Force to dislocation
GC-ROM: Global circumduction range of motion
GLat: Glenoid lateralization
HA: Hemiarthroplasty
HLat: Humeral lateralization
ICC: Intra-class correlation
IE: Internal/external
JCF: Joint contact force
MOO: Multi-objective optimization
NS angle: Neck-shaft angle
OA: Osteoarthritis
PSCA: Physiological cross-sectional area
ROM: Range of motion
RMS: Root-mean-square
RSM: Response surface method
rTSA: Reverse total shoulder arthroplasty
STL: Stereolithographic
TSA: Total shoulder arthroplasty

Chapter 1. Introduction

1.1 Motivation

The number of primary shoulder replacement procedures, of which there are several types, performed in the United States rose by an estimated 169% between 2002 and 2011, from 24,677 to 66,485[1]. Of those performed in 2011, 33% were a type of shoulder replacement known as reverse total shoulder arthroplasty (rTSA)[1,2], which was developed to address pre-operative conditions that contributed to poor outcomes with the use of conventional total shoulder arthroplasty (TSA) and hemiarthroplasty (HA).

The ball-and-socket joint between the humeral head and glenoid on the scapula has the largest range of motion (ROM) of any joint in the body, owing to the lack of osseous constraint provided by a shallow socket depth. As such, both motion and stability of the joint are provided mainly by soft tissues spanning the joint. A group of four muscles, known collectively as the rotator cuff, is responsible for stabilizing the joint in the presence of torque-generating forces via what is known as the concavity-compression mechanism[3–5]. Forces resulting from muscle action to initiate motion, that would otherwise dislocate the joint, are opposed by forces of the rotator cuff, providing a fixed fulcrum for joint rotation. Rotator cuff deficiency presents a challenge in replacing the shoulder with TSA or HA, as the pre-operative disruption of the concavity-compression mechanism, leading to instability of the joint, is not inherently addressed by using components that replicate natural anatomy. Thus, the concept of reversing joint anatomy with rTSA was developed

in the late 1980's by Paul Grammont to address the need for an implant that could be used to treat indications involving rotator cuff deficiencies, which gained FDA approval in 2003[1,6–9].

The leading indication for shoulder replacement is osteoarthritis (OA), which involves degeneration of the articular cartilage, causing pain during joint motion. Of all primary shoulder replacements performed in 2011, 71% were indicated by OA[2]. There are several indications involving rotator cuff deficiencies that are specific to rTSA. The loss of a fixed fulcrum results in migration of the humeral head within the glenoid during motion, which eventually leads to a condition known as cuff tear arthropathy (CTA). CTA is a type of arthritis that involves the abnormal wear of articular cartilage due to altered joint biomechanics in the presence of the rotator cuff deficiency. As such, the main indications for rTSA are massive, irreparable cuff tears, with and without OA, and CTA. Together, they accounted for 82.3% of procedures performed in 2010 and 2011[10].

As with any other joint replacement, two of the primary goals of rTSA are to relieve pain and restore ROM to the joint. The functional success of rTSA is partially gauged using the Constant-Murley score, a 100 point scale comprised of subdivisions related to pain, ability to perform activities of daily living (ADL), strength, and ROM. Pain and ability to perform ADL are patient reported outcome measures, while strength and ROM are assessed clinically. Favard et al.[11] reported a significant improvement in Constant-Murley scores after rTSA for 148 shoulders with average pre- and post-operative scores of 23.9 ± 9.9 and 61.5 ± 16.9, respectively, where the minimum follow-up was five years. The relative improvements in terms of functional category in the order of most improved to least were: pain, ADL, ROM, and strength. This was the largest multi-center study as of 2012[12].

Another study reported that improvements in the Constant-Murley score may be related to indication, where average improvements were 41 and 49.8 points in groups presenting with CTA and irreparable rotator cuff tears (without arthritis), respectively[13]. The reported increases in Constant-Murley score following rTSA are indicative of the efficacy of the procedure, especially in relieving pain. However, further improvements in categories such as ROM and strength could contribute to higher success and patient satisfaction rates.

Due to the nature of the most common indications, rTSA may also be required to mitigate the lack of pre-operative joint stability, a factor that is not accounted for in the assessment of the Constant-Murley score. According to a study that reviewed 782 rTSAs, persistent instability following the procedure was the most common complication requiring revision of the prosthesis, with a rate of 4.7%, followed by infection and aseptic loosening of implant components from the bone[14]. A review by Cheung et al.[15] reported instability rates between 2.4% and 31%, citing that the causes are both directly and indirectly related to implant design.

The selection of implant design and surgical placement parameters of rTSA play a key role in the performance of rTSA as it relates to functional outcomes, namely ROM and stability of the joint. The ROM that can be restored is a function of both passive and active factors. Passively, impingement between the humeral and scapular sides of the joint, whether implant-bone or bone-bone, can limit ROM. Actively, the ROM depends on biomechanical changes affecting muscle action, which are imparted by reversing the anatomy of the joint. Muscle action is also related to the stability of the joint, as it can result in joint contact forces (JCFs) that dislocate the joint or provide little resistance to external forces with the potential to initiate dislocation. The amount of force required to initiate

dislocation is partially dependent on the intrinsic stability provided by the geometry of the implant. Many studies have elucidated relationships between implant design, surgical parameters, and factors that affect functional outcomes of rTSA, however, the common limitations of these studies include: discrete sets of implant parameters, analysis of a subset of factors affecting functional outcomes, and analysis of a subset of motions, neglecting the broad ROM of the shoulder. It is likely that there exists a trade-off between ROM and stability of rTSA. Increasing constraint of the joint can be achieved by altering parameters such as humeral cup depth (Figure 1.1). However, it is likely that this comes at the cost of decreasing ROM, as the impingement-free range is decreased[16]. This trade-off has yet to be characterized, and the combinations of implant and surgical parameters that maximize ROM and stability, evaluated based on passive *and* active factors, following rTSA has yet to be determined.

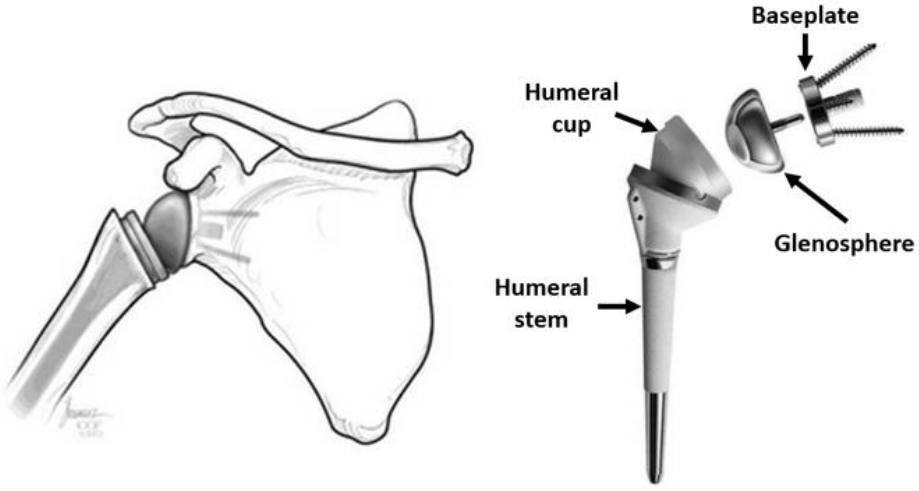

Figure 1.1. Functional outcomes of rTSA, such as stability, can be improved via the selection of implant design parameters, for example, increased humeral cup depth, but this likely comes at the cost of comprising other functional outcomes like ROM. Note: left image adapted from [17] and right image adapted from Journal of Shoulder and Elbow Surgery, 14(1 Suppl), Boileau P, Watkinson DJ, Hatzidakis AM, Balg F, Grammont reverse prosthesis: design, rationale, and biomechanics, 147S-161S, © 2005, with permission from Elsevier.

Given the efficacy of rTSA in treating conditions for which no other options are yet available, the expansion of the list of indications for the procedure, and the rise in the number of rTSAs implanted per year, an increased understanding of the effect of implant design and surgical placement on the functional outcomes of the procedure could serve as a basis for improved success rates and patient-satisfaction.

1.2 Objective

The objective of this research is to characterize trade-offs between ROM and stability of rTSA using multi-objective design optimization to define a Pareto curve, where moving along the curve to improve one outcome comes at a detriment to the other. Multi-objective optimization (MOO) requires objective functions to characterize the outcomes that are to be optimized in the context of selected design parameters. In the case of optimizing ROM and stability of rTSA, this necessitates 1) the development of metrics representing the performance of a given implant configuration and 2) the development and validation of computational (numerical) methods capable of evaluating the metrics, as they cannot be determined by direct, analytical evaluation. As such, several research objectives serve as predecessors to the final goal of MOO:

1. Development and validation of computational methods capable of evaluating factors affecting ROM and stability of rTSA
2. Development of a single, comprehensive metric to characterize ROM
    a. Implementation of computational methods to evaluate ROM in calculation of developed metric

b. Small-scale sensitivity analysis investigating the effects of varying a subset of implant parameters on the developed metric

3. Single objective optimization of ROM
    a. Selection and parameterization of included design and surgical parameters
    b. Compilation of computational tools for evaluating ROM into an automated pipeline capable of evaluating developed ROM metric given an implant configuration
    c. Optimization of ROM of rTSA for different motion envelopes (comprehensive ROM vs those most commonly performed in ADL)
4. MOO considering ROM and stability
    a. Development of an additional metric to characterize functional stability of rTSA
    b. Quantification of trade-offs between ROM and stability

1.3 Hypotheses

Based on the existing body of work relating to the effect of implant design and placement on ROM and stability of rTSA, it is hypothesized that there exists a trade-off between the two functional outcomes. Increasing ROM likely depends on sacrificing stability of the joint, and vice versa.

Additionally, it is hypothesized that there exists a trade-off between maximizing certain envelopes (i.e. forward or backward reaching motions) versus the comprehensive ROM. In other words, the implant configuration that maximizes the comprehensive ROM versus those motions most likely to be performed in ADL are not one in the same.

1.4 Contribution

To the best of the author's knowledge, this research is the first to utilize MOO techniques to maximize functional outcomes of rTSA (ROM and stability) and characterize trade-offs between the two. Furthermore, the effects of multiple passive and active factors throughout the comprehensive ROM of the joint have not been considered simultaneously before. Understanding the effects of implant design and surgical parameters as they relate to the trade-off between ROM and stability could play a vital role in informing clinical decisions related to maximizing one, or both, outcomes of the surgery. Due to the complex and variable nature of indications of rTSA, patient-specific needs are consequently also variable. Some patients may require rTSA to provide stability in lieu of ROM, while others may benefit from a design that provides a balance of both. Access to information regarding functional trade-offs could provide surgeons with necessary insight into which implant configurations would best suit their patients' needs. Additionally, values of design parameters of optimized designs could help determine whether or not commercially available implant systems are providing enough configuration options to allow maximization of surgical outcomes.

Single objective optimization of various envelopes of motion will aid in elucidating whether or not there are trade-offs between maximizing certain post-operative motions of the shoulder. rTSA has been shown to restore limited amounts of certain motions[8,18–21], and this research will help to characterize whether addressing the restoration of these motions will come at the cost of sacrificing ranges of other motions that may or may not be performed more frequently.

Additionally, in developing the computational tools and framework to perform MOO of rTSA, a major challenge relevant to musculoskeletal modeling and the assessment internal (i.e. muscle) forces of the musculoskeletal system, is addressed. Specifically related to joints with complex ROM and bony anatomy, determining anatomically feasible muscle paths with current, computationally efficient methodologies is difficult, especially in an automated manner required by MOO. Therefore, a computational model developed to address this concern is not only applicable to the shoulder and rTSA, but other joints and scenarios that require a reliable method of producing anatomically feasible muscle paths based on variable joint geometry.

The potential future applications of the computational tools presented here are numerous. They could easily be adapted to investigate the effects of variable pre-operative scenarios that could affect the outcomes of the procedure. Namely, the effects of patient-specific bony geometry, muscle strength, and degree of rotator cuff deficiency on the designs that optimize ROM and stability could be characterized with minimal adjustment of the computational framework. Thus, a robust basis is provided for future investigations.

Chapter 2. Background

2.1 Shoulder Anatomy and Motions

The articulation of the shoulder (glenohumeral joint) occurs between the humeral head and the glenoid on the scapula (Figure 2.1); these are the portions of the bones replaced by rTSA components.

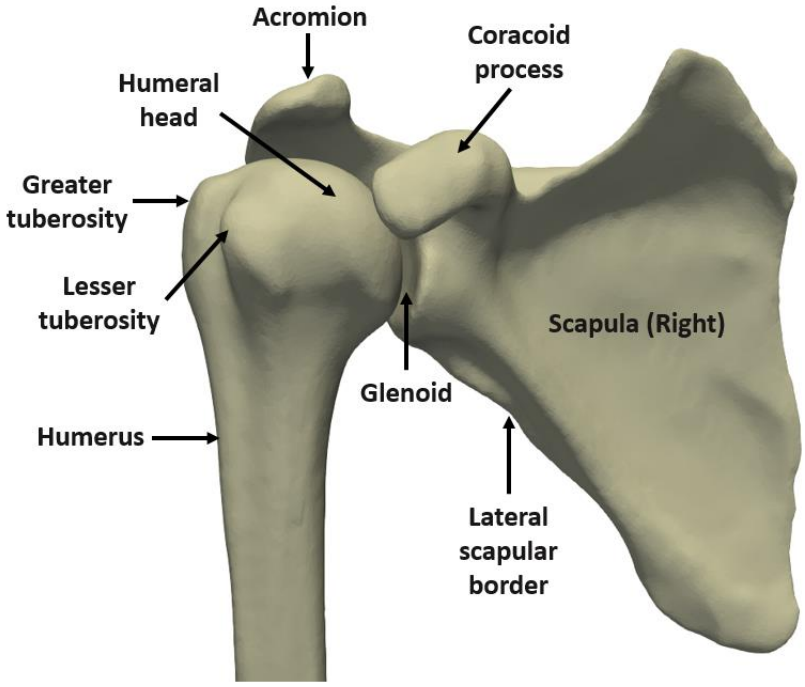

Figure 2.1. Relevant parts of the humerus and scapula

The anatomic planes and relative directional descriptions of the body are shown in Figure 2.2. For the purposes of describing shoulder motion in this document, the neutral position of the arm will be considered as that where the long axis of the humerus lies in the coronal plane, perpendicular to ground, and the palm of the hand faces medially.

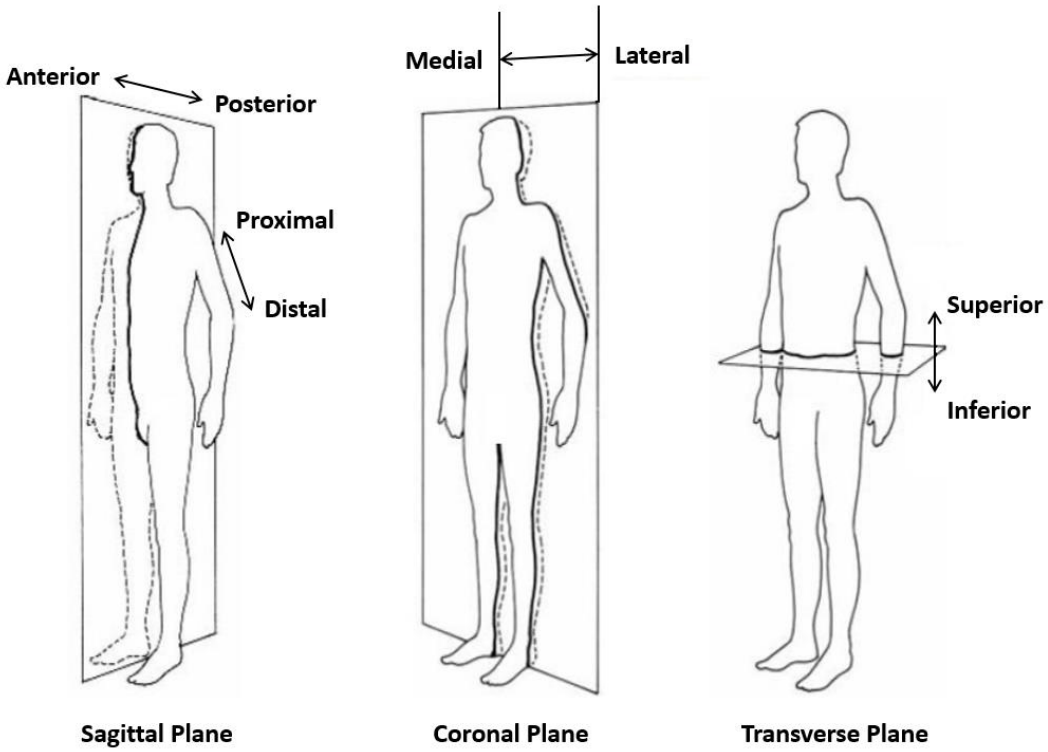

Figure 2.2. The anatomic planes and directions. Note: image adapted from [22].

The shoulder joint has three rotational degrees of freedom with a center of rotation positioned roughly at the center of the humeral head in natural anatomy. Consequently, any position of the arm can be described using spherical coordinates[23,24]. Elevation of the arm correlates to lifting the arm away from the neutral position, from which the elevation angle is measured (Figure 2.3A). Elevation results from rotation of the humerus with respect to the scapula, known as glenohumeral motion, in addition to rotation of the scapula with respect to the thorax, known as scapulothoracic motion. The relative contribution of each type of rotation to elevation is quantified by the scapulothoracic rhythm, which is the ratio of glenohumeral to scapulothoracic motion required to accomplish a degree of elevation. In the healthy shoulder, the scapulothoracic rhythm is generally accepted to be 2:1, meaning that for 90° of arm elevation, 60° and 30° are contributed by glenohumeral and scapulothoracic rotations, respectively.

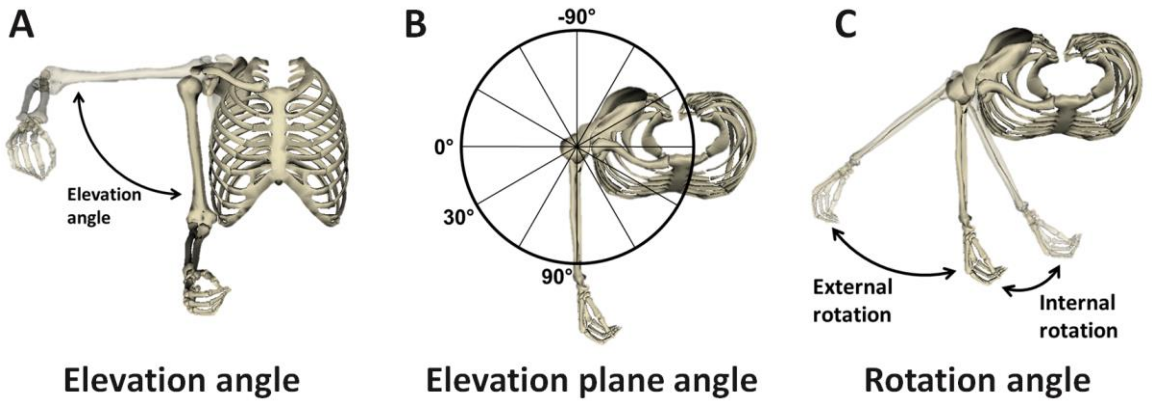

Figure 2.3. The coordinates that describe a given position of the arm are elevation angle(A), elevation plane angle (B), and axial rotation angle (C), otherwise known as internal/external (IE) rotation angle.

The direction (plane) in which elevation occurs is described as the elevation plane. From a viewpoint perpendicular to the transverse plane, elevation plane angle is measured from the coronal plane (Figure 2.3B). Common names for specific elevation motions of the arm are based on the elevation plane in which they occur. Abduction, scaption, flexion, and extension occur in elevation planes with angles of 0°, 30°, 90°, and -90°, respectively. An additional rotational degree of freedom, known as axial rotation, corresponds to the rotation of the humerus about its long axis (Figure 2.3C).

Shoulder motions are driven by nine musculotendon units that cross the joint (Figure 2.4), which are also responsible for stability. Muscles are connected to bone at locations known as the origin and insertion sites via tendons. Origins and insertions correspond to the proximal and distal sites (Figure 2.2), respectively.

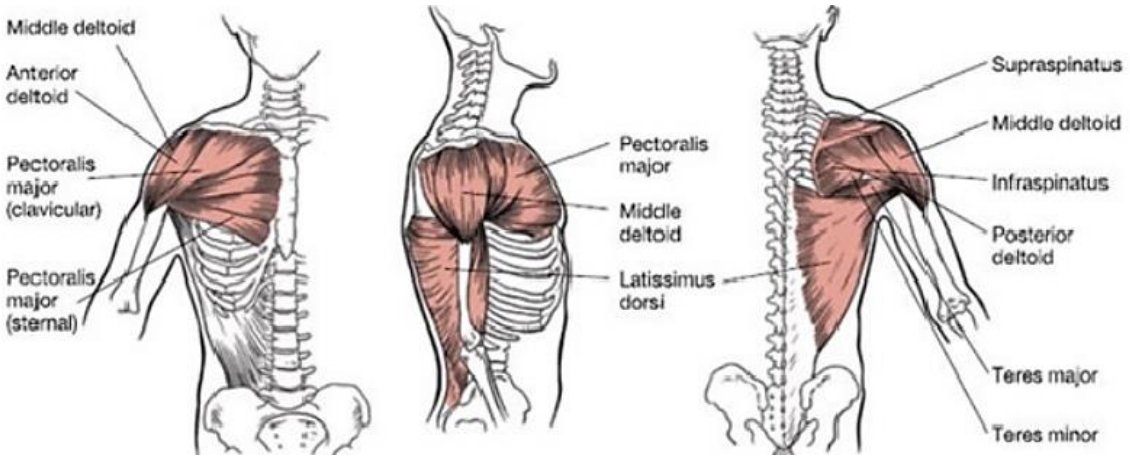

Figure 2.4. The nine musculotendon units that cross the shoulder drive motion of the joint [25]. Note: the subscapularis, which is underneath the anterior deltoid and pectoralis major, is not shown.

The deltoid is the primary driver of arm elevation and is commonly described using three sections due to the breadth of its origin footprint which wraps from the clavicle (anterior section) around the acromion (middle section) to the scapular spine (posterior section). The anterior, middle, and posterior sections contribute to flexion, abduction, and extension, respectively. The anterior and posterior sections also aid in internal and external rotation, respectively. The supraspinatus, infraspinatus, subscapularis, and teres minor comprise the rotator cuff. Each contributes to different motions. The supraspinatus aids in elevation, more specifically abduction. While the subscapularis, infraspinatus, and teres minor contribute to elevation, they also provide forces conducive to axial rotation. The subscapularis serves as an internal rotator, while the infraspinatus and teres minor act as external rotators.

Perhaps the most important role of the rotator cuff as a unit relates to joint stability. During motion initiation, the deltoid produces superiorly-directed forces, which could potentially dislocate the joint (Figure 2.5). Simultaneous contraction of the muscles comprising the rotator cuff provides a net force that is medially-directed, to oppose the

deltoid forces and keep the humeral head seated in the glenoid during motion, termed the concavity-compression mechanism.

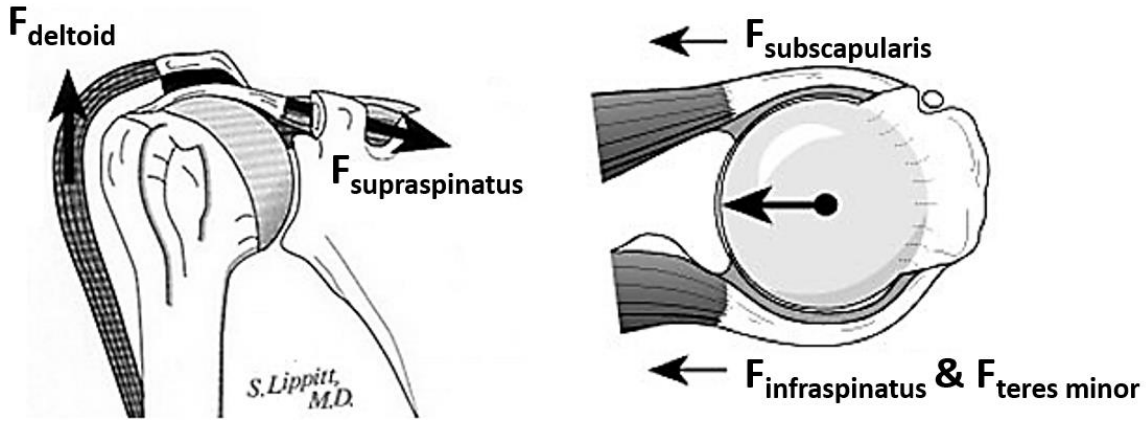

Figure 2.5. As motion of the arm is initiated, the deltoid produces superiorly-directed forces. Without sufficient opposition from the medially-directed forces imparted by the rotator cuff muscles, the shoulder can become unstable. Note: figure adapted from [26].

Rotator cuff deficiencies can lead to several conditions, notably CTA, a specific arthritic pattern resulting from superior migration of the humeral head due to the disruption of the concavity-compression mechanism. In situations where replacement of the joint is required, conventional TSA or HA has performed poorly, because the underlying biomechanical factors that lead to pre-operative joint instability are not addressed. Thus, post-operative instability and migration of the humeral head within the joint are likely to persist. As a result, repeated eccentric loading on the glenoid component (Figure 2.6) may cause premature failure of the implant via the "rocking horse effect," which initiates premature loosening of the implant from the bone.

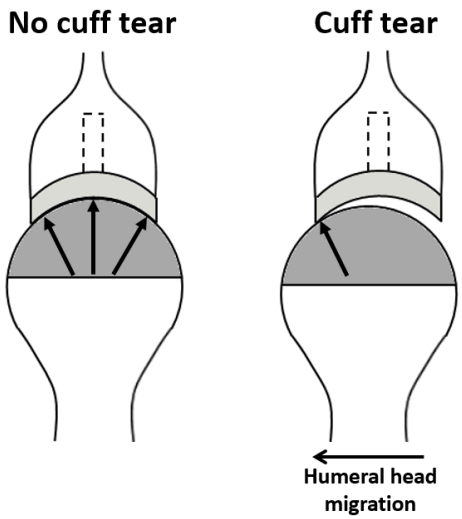

Figure 2.6. The mechanism responsible for the rocking horse effect.

2.2 rTSA

2.2.1 Biomechanics of rTSA

The concept of reversing the anatomy of the joint was developed specifically to address limited pre-operative ROM and joint stability in the presence of a rotator cuff deficiency. Several early reverse shoulder designs were developed beginning in the early 1970's starting with the Mark I reverse prosthesis developed by Charles Neer[6,7,27]. It included spherical and concave components fixed to the glenoid and humeral head, respectively.

The concept of reversing the anatomy was intended to restore range of motion and stability to the joint by preventing superior migration of the humeral head via constraint inherent to the conformity of implant components[27]. Several iterations of the design were developed to address issues including limited range of motion restoration and persistent joint instability. The glenoid component was designed in a manner that placed the joint center of rotation (COR) close to where it would have been naturally. Consequently, ROM restoration was based on rotator cuff function, because there were no significant

biomechanical changes that would mitigate weakness caused by a cuff deficiency. However, the worst results involved consistent implant failure via aseptic loosening of the glenoid component. Loosening occurred because a joint COR lateral to the bone-implant interface of the glenoid component caused joint contact forces, which pass through the joint COR, to introduce torque at the bone-implant interface. This torque resulted in micromotions of the implant exceeding the levels that allow for stable fixation. Although various glenoid fixation strategies were utilized, Neer's designs as well as a multitude of others developed by various groups, were subject to implant failure via loosening. Those that were not plagued by loosening issues permitted unsatisfactory improvements in functional outcomes of the procedure due to their dependence on rotator cuff function, and thus all early designs were eventually abandoned by 1980[27].

Reversing joint anatomy was reintroduced by Paul Grammont in 1985, with a reverse shoulder design relying on several innovative concepts to restore ROM and provide stability to the joint while avoiding catastrophic failures due to implant loosening. Grammont's initial design consisted of only two components, both which were cemented (Figure 2.7).

Figure 2.7. Paul Grammont's original reverse shoulder design. Reprinted from Journal of Shoulder and Elbow Surgery, 14(1 Suppl), Boileau P, Watkinson DJ, Hatzidakis AM, Balg F, Grammont reverse prosthesis: design, rationale, and biomechanics, 147S-161S, © 2005, with permission from Elsevier.

The glenosphere, two-thirds of a sphere made of cobalt-chrome, was designed to fit over the glenoid. The humeral component was made entirely of polyethylene and the depth was one-third of the glenosphere diameter. As with earlier designs, Grammont relied on implant constraint to provide joint stability, but introduced the idea of altering joint anatomy in a manner that allowed for the deltoid to compensate for the deficient rotator cuff in terms of motion restoration. With the glenosphere design and placement, the COR of the joint was medialized and distalized with respect to natural anatomy. Functionally, this has several effects. Specifically related to medialization, the moment arm of the deltoid is increased, thereby reducing necessary force production to generate levels of torque necessary to initiate motion, as well as achieve and maintain arm positions. Additionally, more deltoid fibers can be recruited for elevation. Distalizing the COR and using a non-anatomical neck-shaft angle for the humeral component effectively lowers the humerus, which tensions the deltoid to aid in force production. In combination, these factors

essentially allow the deltoid to perform more efficiently than in natural anatomy, which compensates for missing motion-driving torques that would have been contributed by the rotator cuff.

Grammont reported results on his initial design for 8 patients in 1987 with functional results exceeding any of the early designs; however, he was still concerned with glenoid-side fixation. Since COR was medialized with respect to natural anatomy, torque at the bone-implant interface was reduced in comparison to previous designs, but was not eliminated since using two-thirds of a sphere still placed the COR lateral to the interface. Grammont altered his initial design by introducing a new fixation strategy, which involved two components on the glenoid-side. The spherical component, now half of a sphere, was screwed onto the peripheral edge of a cylindrical plate that was impacted into the glenoid and supported further by divergent screws pointing superiorly and inferiorly. Using half of a sphere placed the COR directly on the bone-implant interface, thereby eliminating torque introduced by JCFs, and provided more rigid fixation as opposed to the first cemented version. This design, called the DELTA III prosthesis, was the first reverse shoulder reaching the market in 1991. Improvements were made over the span of several years to address fixation issues and maximize functional outcomes. The third generation of the DELTA III prosthesis (Figure 2.8) became available in 1994 and is still in use today.

Figure 2.8. The design of Grammont's Delta III prosthesis. Reprinted from Journal of Shoulder and Elbow Surgery, 14(1 Suppl), Boileau P, Watkinson DJ, Hatzidakis AM, Balg F, Grammont reverse prosthesis: design, rationale, and biomechanics, 147S-161S, © 2005, with permission from Elsevier.

Grammont's DELTA III design, although still available, has served as the basis for the development of the many other reverse shoulder systems most of which have the same basic components pictured in Figure 2.8. Among different the more than 29 commercially available rTSA designs[29], the general principle of leveraging muscles for motion differently than in natural anatomy and providing inherent stability via implant design in place of what would be provided by a fully functional rotator cuff is consistent. However, as a result of increased understanding pertaining to the effects of implant design and surgical placement parameters on functional outcomes of the procedure since the inception of Grammont's design, variations in implant configuration have become available.

2.3 Factors Affecting Functional Outcomes of rTSA

As with any joint replacement, there has been a significant amount of research dedicated to investigating the effects of varying implant design and surgical placement parameters on the outcome of rTSA. Evaluating functional outcomes of the procedure is

particularly complex in the case of rTSA, as the effects of reversing the anatomy of the joint are multi-faceted, and the ROM of the shoulder is complicated.

There are three basic requirements for any arm position within the potential ROM of the shoulder to be attainable after rTSA, including 1) there must not be impingement between the humeral and scapular sides of the joint, whether bone-bone or bone-implant, 2) the viable musculature spanning the joint must be capable of generating sufficient forces to maintain the position, and 3) JCFs developed as a result of muscle action must not dislocate the joint. Dislocation in the context of muscle forces, and therefore JCFs, developed to overcome gravity in the maintenance of a static arm position plays a role in limiting ROM. In other words, any arm position where the joint will dislocate as a result of achieving the position is not considered a part of the ROM. Functional stability, which will be considered as a performance metric to maximize in MOO, relates to the ability of the implant to resist dislocation in the presence of external forces on the joint resulting from interaction with the environment.

In the following sections, relevant implant design and surgical parameters (i.e. those investigated in this body of work) will be introduced, and their effects on the various factors relating to ROM and stability will be discussed. It should be noted that in general, studies characterize the effects of varying implant design parameters on specific motions, including: abduction/adduction, scaption, flexion/extension, and internal/external rotation (Figure 2.9). Therefore, the effect of implant design will be discussed in the context of these motions.

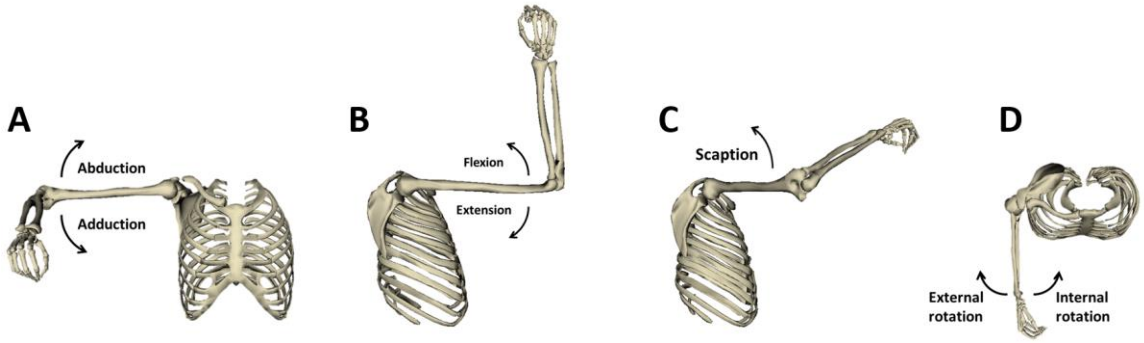

Figure 2.9. Motions commonly included in the study of the effect of rTSA on ROM include A) abduction/adduction B) flexion/extension C) scaption and D) internal/external rotation.

2.3.1 The Effect of Varying Implant Parameters on Impingement-free ROM

Perhaps the most studied aspect of the relationships between implant design and the functional outcome of rTSA is the effect of varying implant parameters on impingement-free passive ROM. Several studies, both experimental and computational, have elucidated relationships between implant parameters and resulting passive ROM. They have provided some insight into which implant configurations have the potential to maximize ROM.

There is agreement across several studies that inferior placement of the glenosphere (Figure 2.10) increases ROM. Computational studies by Roche et al.[16] and Kontaxis and Johnson[30] concluded that inferior offset of the glenosphere increases overall ROM in scaption. A cadaveric study performed by Nyffeler et al.[31] also confirmed that, of four different glenosphere positions, the only configuration with an inferior overhang of the glenosphere with respect to the glenoid allowed the greatest ROM in scaption. Similar findings have been reported for abduction using computational models, where increasing inferior offset of the glenosphere increases the magnitude of the range between inferior and superior impingement points[30,32–35].

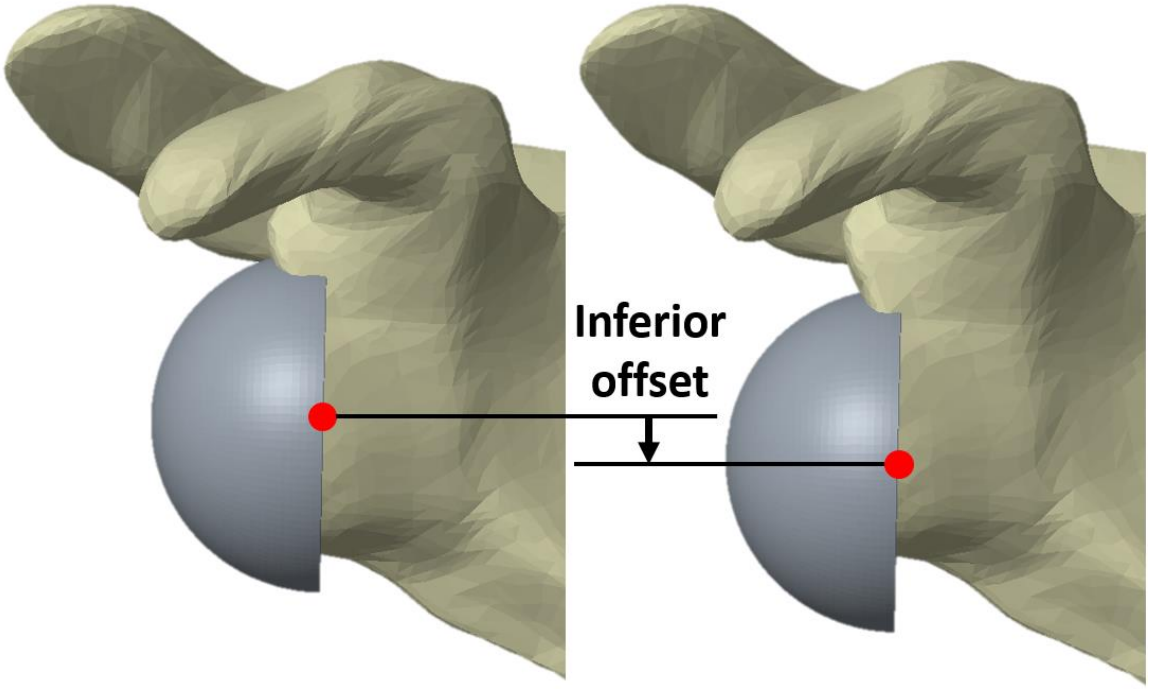

Figure 2.10. A depiction of inferior placement of the glenosphere, which has been reported to increase ROM.

Neck-shaft (NS) angle of the humeral stem (Figure 2.11) has also been shown to have an effect on ROM, such that decreasing NS angle increases ROM in abduction, adduction and scaption[32–39]. Virani et al.[35] concluded that NS angle was the most predictive parameter in terms of increasing abduction. Gutiérrez et al.[32,33] reported that NS angle had the greatest effect of other parameters studied on increasing adduction ROM, while de Wilde et al.[36] reported that it had the least effect. Interestingly, Virani et al.[35] found that while decreasing NS angle improved abduction ROM, it also decreased ROM in both flexion/extension and internal/external rotation. In contrast, Oh et al.[37] found that NS angle did not affect internal/external rotation ROM.

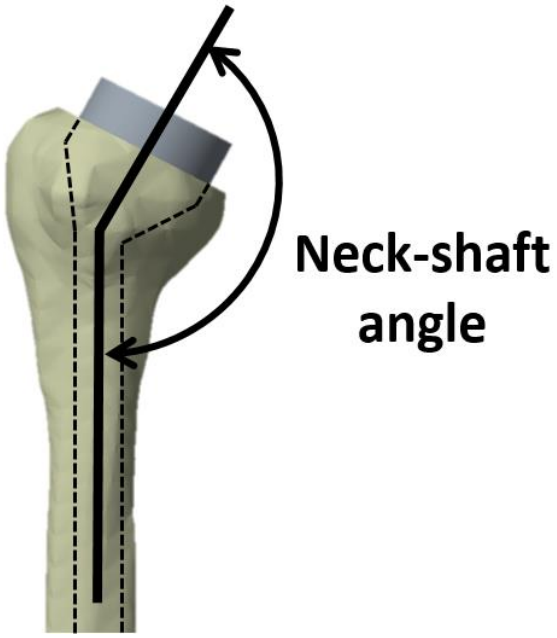

Figure 2.11. A depiction of the definition of NS angle as it relates to rTSA design.

Several studies suggest that lateralizing the COR with respect to a fully medialized location on the bone-interface (Figure 2.12) increases abduction, flexion/extension, and internal/external rotation[32,33,35,38–40]. Others have concluded that lateralization significantly increases adduction ROM, and may be a viable option for avoiding inferior impingement[30,33]. De Wilde et al.[36] reported that lateralization increased adduction ROM before impingement, but the effect was negligible when the glenosphere was placed inferiorly. It should be noted that present techniques for COR lateralization, which involve spacers behind the glenosphere (Figure 2.12), or glenospheres that comprise more than half of a sphere, do not lateralize the COR to the same levels as early reverse shoulder designs; this decreases the risk of loosening due to torque at the bone-implant interface, however it is still a concern.

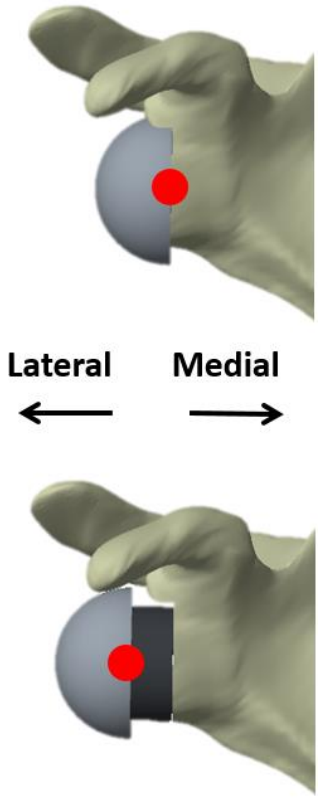

Figure 2.12. A depiction of lateralizing the COR of rTSA from the bone-implant interface.

2.3.2 The Effect of Varying Implant Parameters on Joint Stability

In addition to the ROM allowed by an implant, another important factor is the amount of joint stability that can be provided by the implant. As with ROM, stability depends on both passive and active factors that relate to the geometry of the implant, as well as contributions of the musculature surrounding the joint. Clouthier et al.[41] (2013) found that of the factors studied, including loading direction, elevation angle, elevation plane angle, humeral cup depth, glenosphere diameter, and inferior placement of the glenosphere, that the largest increase in force to dislocation was due to abduction angle. Higher abduction angles increased the force to dislocate the joint. At higher elevations the ratio of shear to compressive JCF is lower[42], because the resultant lines of action of muscle forces, especially the deltoid, point more medially as opposed to superiorly, illustrated in Figure

2.13 for the anatomic shoulder. Supporting this notion, Gutiérrez et al.[43] found that increasing compressive force had the greatest effect on increasing stability.

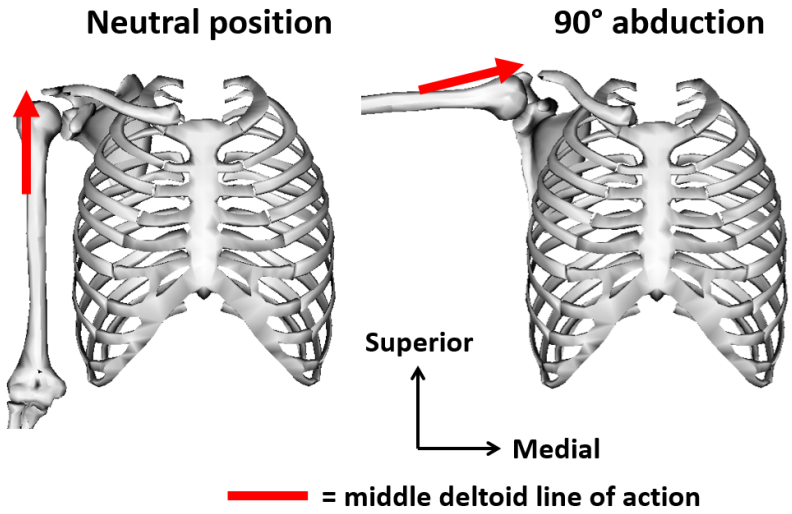

Figure 2.13. Increasing abduction angle lowers the shear to compressive JCF ratio, leading to a more stable joint, as the lines of action of the muscles are directed more medially exemplified by the middle deltoid at neutral arm position (left) and 90° of abduction (right).

Clouthier et al.[41] also concluded that inferior placement of the glenosphere increased inherent stability of the joint. A study by Kontaxis and Johnson[30], in which a musculoskeletal model was employed, found that glenosphere placement did not affect the ratio of shear to compressive joint contact forces developed during different motions. Together, these findings highlight the necessity to consider not only the inherent stability of the implant in terms of resistance to dislocation forces, but also how it performs in the context of the JCFs resulting from muscle action, which are a function of joint angles (arm position) as well.

2.4 Musculoskeletal Modeling

Musculoskeletal modeling is a valuable tool that is seeing increased use in order to evaluate internal forces in the neuromuscular system, such as muscle forces and JCFs (Figure 2.14). These forces are difficult to determine experimentally. With the ability to

determine internal forces through simulation, as opposed to experimentally, it becomes easier to identify cause-effect relationships of various conditions (i.e. what is causing a pathological gait abnormality versus what the gait abnormality is causing) as well as evaluate the efficacy of different treatments.

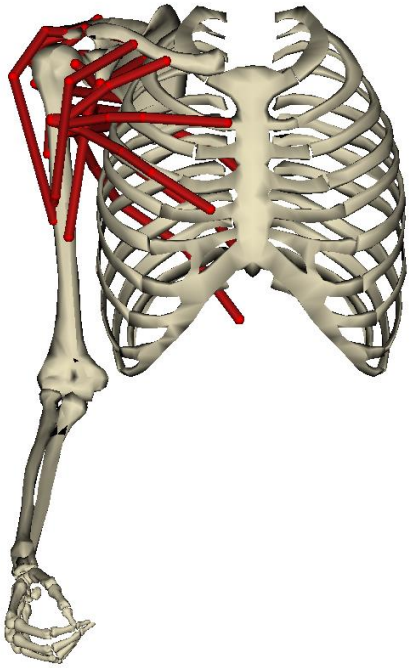

Figure 2.14. A musculoskeletal model of the upper limb developed and validated by Holzbaur et al.[24].

In the case of rTSA, where the premise behind the success of the procedure relies partially on how muscles are leveraged differently than in normal anatomy, musculoskeletal modeling is an available option for evaluating the effect of the implant design on functional outcomes in the context of muscle capability and joint stability. This necessitates a discussion of the general principles underlying musculoskeletal modeling and how they allow for calculations related to forces internal to the musculoskeletal system (i.e. muscle forces and JCFs).

2.4.1 Joints and Motion Definitions in Musculoskeletal Models

In musculoskeletal models, bones are modeled as rigid bodies that are connected by joints. Joints are defined using generalized coordinates. That is, for every degree of freedom at a joint, one ordinary differential equation is necessary. It is formulated to allow motion only in the desired direction(s). In this manner, algebraic constraints are unnecessary and solving for motions at joints is much less computationally costly than solving a system of differential-algebraic equations. Traditionally, for a one degree of freedom joint, a system of 11 equations would be solved simultaneously: one differential equation for each degree of freedom and five algebraic constraints on the degrees of freedom that are not desired. A one degree of freedom joint is defined by one ordinary differential equation corresponding to the generalized coordinate that has been prescribed. Coordinate coupler constraints can also be used to parameterize coordinates relative to another by some function. Using generalized positions (defined by the coordinates), velocities, and accelerations, as well as user-defined inertial properties, the equations of motion can be solved in order to obtain unknown generalized forces on a joint. This is known as an inverse dynamics analysis, where the motion of the system is known and the forces resulting from the motion are calculated. Forward dynamics allows for the calculation of generalized positions, velocities, and accelerations by solving the equations of motion with a known set of generalized forces to predicting what motion will result.

2.4.2 Calculating Muscle Forces with Musculoskeletal Models

Musculotendon units are force-producing actuators that span joints. Physiologically, bundles of fibers comprise the body of a muscle, each end of which is attached to a bone by a tendon at locations known as the origin and insertion.

Neuromuscular excitations lead to activation of muscle fibers, causing them to contract and generate force, which is transmitted through the tendons and manifests as torques that drive motion of a joint. The generalized torque on a joint resulting from muscle action is given by:

$$\tau_J = \sum_{m=1}^{n} F_m r_m \qquad \text{Eq. (2.1)}$$

where n is the number of muscles crossing the joint, F_m is muscle force, and r_m is muscle moment arm. As such, joint torque resulting from muscle action is based on muscle path, from which the muscle moment arm is determined as the perpendicular distance to the joint COR, and muscle force. Muscle forces required to generate a set of generalized joint torques to produce a specific joint motion or position generally cannot be determined analytically due to a problem known as muscle force redundancy. Unless a highly simplified model is used, the number of muscles spanning any joint exceeds the number of equations available to solve based on the DOF of the joint, resulting in an indeterminate system. This necessitates the use of numerical methods, which involve the optimization techniques to determine a set of muscle forces required to produce a given motion or sustain a joint position.

There are two types of optimization: dynamic and static. Dynamic optimization is a forward dynamics approach which incorporates time-dependence of both muscle force and performance criteria into the calculation of muscle force configurations. In contrast, static optimization is a time-independent, inverse dynamics approach. Dynamic optimization is computationally costly and has been shown to produce results similar to static optimization[44,45]. In static optimization, kinematics of a joint and external forces serve as inputs to an inverse dynamics analysis, from which generalized joint torques

required to maintain static joint positions (equilibrium) are extracted. Information about the muscle moment arms and physiological relationships pertaining to force production in muscles is used to find a configuration of muscle forces that produces the required generalized torque by minimizing a neurophysiologically relevant performance criterion.

Countless configurations of muscle forces could produce the same generalized joint torques, but it is likely that the nervous system selects configurations based on minimizing some expenditure required to do so, such as: energy consumption, muscle stress, muscle fatigue, etc. One such performance criterion to minimize during static optimization is given by:

$$f(F_m) = \sum_{m=1}^{n} {a_m}^p \qquad \text{Eq. (2.2)}$$

where a_m is the activation of a muscle and p is a user-defined constant. Although a multitude of performance criteria have been proposed, several studies have concluded that results are not highly sensitive to this selection, provided the order of the function is greater than one[46–50]. Van Bolhuis and Gielen[46] investigated the effect of performance criterion on muscle force prediction. They included performance criteria involving total muscle force, total muscle stress, total muscle activation, and metabolic energy consumption. Additionally, the order of each equation was varied. Of the criteria studied, any involving muscle force and metabolic energy were rejected, as they did not provide muscle activation patterns consistent with electromyographic (EMG) results. The best over-all fit to experimental data was observed using quadratic equations for performance criteria (p=2 in Eq. 2.2). In the case of isometric muscle contractions, where the joint angle and muscle lengths, are constant (as is the case in static optimization), muscle stress is essentially a measure of muscle activation. As such, performance criteria involving either factor produce similar muscle activation and force distribution patterns[46].

The minimization of a selected performance criterion must involve constraints that reflect physiologic relationships between muscle parameters and possible force production. Physiologically, the forces developed in a muscle are dictated by: activation level, length of muscle fibers, velocity of contraction or stretching of the muscle fibers, physiologic cross-sectional area (PSCA) of the whole muscle (i.e. how many fibers make up a muscle), and pennation angle, which defines the orientation of muscle fibers with respect to the tendon that connects it to a bone. These characteristics are measured experimentally and serve as inputs to analytical functions which capture musculotendon dynamics and force-generating behavior. Musculotendon units are modeled as 1-dimensional line segment entities, the dynamics and force-generation of which are represented by lumped parameter solids, known as Hill-type muscle models (Figure 2.15).

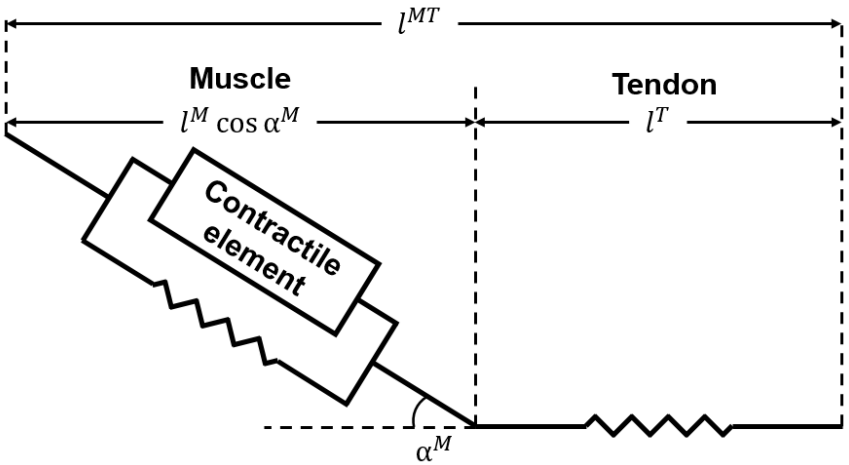

Figure 2.15. A lumped parameter muscle model.

Tendons are lumped to one side of the muscle and represented as a passive spring force. The muscle is modeled by an “active” contractile element, representing the ability of the muscle fibers to actively generate force, in parallel with a passive spring element, representing the elastic properties of the fibers. Within the contractile element is a spring and dashpot in parallel, representing the dependence of muscle force on velocity. The

behavior of each element in the lumped parameter model is dictated by either a state equation or a parameterless curve scaled based on experimentally determined values (Figure 2.16).

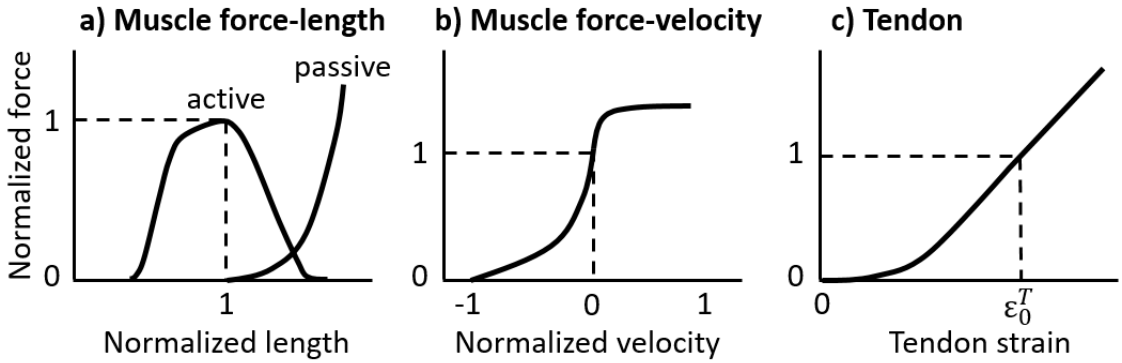

Figure 2.16. The relationships between normalized force and a) normalized length of both the active and passive components of a muscle, b) normalized velocity of a muscle, and c) tendon strain, which is a function of its length. Note: a = activation, which can range from 0 to 1.

Force is normalized to the maximum isometric force that a muscle can produce. This is determined by measuring PCSA and multiplying by specific tension. The length is normalized by optimal fiber length, which is the fiber length at which the maximum force is produced. Velocity is normalized to the maximum contraction velocity of a muscle fiber. Tendon strain is calculated using instantaneous tendon length and tendon slack length, or the length at which a tendon begins producing force if it is stretched further. PSCA, optimal fiber length, maximum contraction velocity, and tendon slack length are the experimentally determined values used to scale the parameterless curves to represent different muscles. Additionally, pennation angle is measured experimentally to enforce the relationships between the length of muscle fibers in relation to the length of the entire musculotendon unit. The differential equation representing the musculotendon dynamics, assuming the muscle and tendon are massless and that all force generated in the muscle is transmitted through the tendon, is as follows:

$$f_{iso}\left(a(u,t) * f_{CE}(l^M) * f_v(\dot{l}^M) + f_{PE}(l^M)\right)\cos\alpha - f_{iso}f_S(l^T) = 0 \quad \text{Eq. (2.3)}$$

where f_{iso} represents the isometric force in a muscle, f_{CE} and f_v represent the force-length and force-velocity relationships of the contractile element of the muscle, f_{PE} represents the force-length relationship relating to passive elasticity of the muscle, f_S represents the force-strain relationship of the tendon, and a(u,t) is the activation dynamics as a function of excitation (u) and time (t). The equation is solved for $f_v(\dot{l}^M)$, after which the force-velocity relationship is inverted, such that integration can be performed to determine musculotendon dynamics. The dynamics of a musculotendon unit dictate the relative proportions of the entire length that are accounted for by the lengths of the muscle fibers and the tendons separately. During static optimization, musculotendon dynamics are determined in order to enforce force-length and force-velocity relationships, as they affect possible force generation. In other words, a muscle can only produce its maximum force if the length of the fibers and their rate of contraction/stretching is ideal, which is generally not the case for any given joint position; static optimization can only produce realistic forces based on these factors by using them as constraints. Consequently, the static optimization objective function (Eq. 2.2) is minimized subject to:

$$\tau_J = \sum_{m=1}^{n}\left[a_m f\left(f_{iso}, l^M, \dot{l}^M\right)\right] r_m \quad \text{Eq. (2.4)}$$

2.4.3 Musculoskeletal Model of the Upper Limb

The National Center for Simulation in Rehabilitation Research has developed an open-source musculoskeletal modeling software called OpenSim[51,52], which was used in conjunction with an adapted version of a validated a musculoskeletal model of the upper limb that is freely available[24] (Figure 2.14). Three generalized coordinates are used to describe the position of the arm at any given time: elevation plane angle, elevation angle,

and internal/external rotation angle (Figure 2.3). The scapulothoracic rhythm is defined using coordinate coupler constraints, where the rotations of the scapula and clavicle with respect to the thorax are determined based on the elevation angle of the glenohumeral joint. Simplified scapulothoracic motion is included in a 2:1 rhythm. The axes for the various rotations permitted at the glenohumeral joint, as well as the regression equations used to define scapulothoracic motion, were taken from a study by de Groot and Brand[53] and are in accordance with recommendations by the International Society of Biomechanics for describing motion of the shoulder[54]. The information pertaining to the body segments required to solve the equations of motion (i.e. mass, mass center location, and inertial properties) was based on anthropometric data of a 50th percentile male.

All nine muscles that cross the joint are represented. The deltoid, pectoralis major, and latissimus dorsi are each represented by three distinct bundles due to their broad origin footprints. The deltoid has anterior, middle, and posterior sections, while the pectoralis major and latissimus dorsi have superior, middle, and inferior sections. The remaining muscles (supraspinatus, infraspinatus, subscapularis, teres minor, teres major, and coracobrachialis) are represented by one bundle each. The locations for the origins and insertions of each muscle bundle were determined based on digitized images of the bones that were represented in the model.

Muscle paths, as a function of joint position, were determined using a combination of via points and wrapping geometry. Via points, through which the path of a muscle is constrained to pass, can be fixed or moving based on prescribed coordinate change functions within the coordinate frame of a bone. Examples of fixed via points include all insertion sites, the locations of which are constant within the humeral coordinate frame.

Moving via points are sometimes utilized in order to maintain anatomic feasibility of muscle paths that would not be possible using fixed via points. In addition to via points, rudimentary wrapping geometry, around which the shortest geodesic paths are calculated, are used to represent bony anatomy. The geometries, including spheres, ellipses, cylinders, and tori are fixed within the respective coordinate frame of the bone to which they are attached and sections of muscle bundles between via points wrap over them to simulate the anatomic dependence of muscle paths on bone geometry. Holzbaur et al.[24] determined locations of fixed via points, functions for moving via points, and placement of wrapping geometries that resulted in muscle paths with moment arms that coincided with experimentally available values from literature in order to best capture force-generating capabilities. Other parameters affecting muscle force-generation, including optimal fiber length, maximum isometric force, tendon slack length, and pennation angle were taken directly, or derived from, previous experimental studies[24].

2.5 Surrogate Models

2.5.1 Response Surface Method

Inherent to the process of design optimization is computational efficiency of evaluating the objective function(s). The task of evaluating ROM and stability of rTSA within broad motion limits rendered use of the actual model(s) to evaluate the objective functions infeasible in terms of required computational time. In cases where the objective function is based on a finite set of experimental results, or the computational cost of evaluating the values and gradients of objective function numerically for a potentially large number of designs is too great, surrogate, or meta-models, have been used. In terms of design optimization, surrogate models are based on generating an explicit representation

of the objective function in terms of the design variables by fitting an equation to results from a set of pre-determined sample designs. The response surface method (RSM) is one that is used to generate linear or quadratic equations representing the objective function. Quadratic equations including linear, perfect square, and cross-product terms are most commonly used, as they capture curvature of the objective function (provided the sample points are chosen in a manner that allows this) and interactions between variables, and the general form is given by[55]:

$$J(\vec{x}) = a_0 + \sum_{i=1}^{k} a_i x_i + \sum_{i=1}^{k} a_{ii} x_i^2 + \sum_{1 \le i \le j}^{k} a_{ij} x_i x_j + \varepsilon \qquad \text{Eq. (2.5)}$$

where a_0 is a constant, x_i and x_j are design variables, *k* is the number of design variables and a_i, a_{ii}, and a_{ij} represent the coefficients of the linear, quadratic, and cross-product (interaction) terms, respectively. ε is the residual, or error associated with the surrogate model approximation of the actual function. In the RSM, where the value of the function is evaluated with the real model at a given number of designs ($\vec{x}$), the unknowns are the coefficient matrices, determined by minimizing the sum of the squares of the residual using a regression technique known as the least squares method, which is well established. In the context of this research, the RSM was used to generate surrogate models for the objective functions representing ROM and stability of rTSA in order to greatly decrease the computational cost of single and multi-objective optimization.

2.5.2 Sample Point Selection for Response Surface Method

In using the RSM, consideration must be given to the number and distribution of sample designs throughout the design space which are used for fitting the response surface. In general, choosing sample points involves a design of experiments (DoE). Various strategies exist for generating a DoE which contains a minimal number of meaningful sample points

for use in the RSM, which is advantageous in balancing computational or experimental cost of evaluating an objective function with accuracy of the resulting surrogate model. Other strategies involve full factorial designs, where all possible combinations of chosen design variable values are evaluated. The number of values for each design variable is referred to as the number of levels (L). Generally, the minimum and maximum value of each design variable are identified, and the ranges are discretized into L evenly spaced points, resulting in an L^k full factorial design (where k is the number of design variables). Each design variable must have at least three levels in order for the curvature of the objective function to be captured in the surrogate model. Problems where the number of design variables exceeds five are generally approached with strategies other than full factorial DoEs[56]. Additionally, the number of model evaluations or experiments required can quickly become too costly when the number of levels exceeds four. Therefore, a common full factorial design is 3^k, where k is less than five.

Chapter 3. Development and Validation of Computational Methods for Evaluating Factors Affecting ROM of rTSA

The ROM allowed by any given rTSA configuration depends on impingement, muscle capability, and stability. Optimizing the ROM while considering all three factors requires the development and validation of computational methods for evaluating each. Each of the following sections will outline the computational or analytical methods involved in evaluating the three ROM-limiting factors, as well as the validation procedures and validation results for the methods.

3.1 Impingement

3.1.1 Methods

3.1.1.a Computational Model Development

A computational model implanted with a representative rTSA configuration was developed and subsequently validated experimentally. Polygonal descriptions of a scapula and humerus were processed from the Holzbaur et al.[24] musculoskeletal model into stereolithographic (STL) surface files using an open-source program, Paraview[57,58]. The implant configuration was a traditional Grammont-style implant: a 36 mm diameter

hemispherical glenosphere with the COR lying directly on the bone-implant interface and a NS angle of 155°. The bones were virtually implanted based on a surgical technique guide[59] and verified for accuracy by two orthopaedic shoulder surgeons (Dr. George S. Athwal and Dr. Joseph Choi).

The glenoid was reamed with a retroversion of 35°, determined by a plane perpendicular to the ground and passing through points on the anterior and posterior rims of the glenoid. The center of the 36 mm ream was determined by fitting a 25 mm diameter circle, representing the size of the baseplate, to the inferior rim of the anatomic glenoid in the aforementioned plane that was used to determine version. The ream depth measured 3 mm from the inferior glenoid rim, which was the minimum depth to create a flat surface on which the glenosphere was placed with the COR coincident with the ream (and baseplate) center. The humerus was reamed with a retroversion of 35° and the NS angle measured from the long axis of the humeral shaft to a depth dictated by the inflection point created by the junction of the humeral head and the greater tubercle. The humeral cup, with a depth of 6 mm and overall height of 10 mm, was placed at the center of a circle fit to the edge created by the ream on the humerus. All reams and implantations were accomplished using either subtractive or additive Boolean operations, such that each portion of the joint was a monobloc including the bone and respective implant component (Figure 3.1).

The implanted shoulder was incremented through various motions using custom MATLAB scripts, which implemented the motion definitions from the Holzbaur et al.[24] musculoskeletal model. The arm was first axially rotated from the neutral position to -30°, 0°, or 30°, where negative and positive angles represent external and internal rotation, respectively. Following axial rotation, the arm was elevated in planes with angles ranging

from -90° to 120° by increments of 30°. The scapulothoracic rhythm was removed for ease of model replication during experiments. At 10° increments of elevation, custom python scripts written for the open-source program Blender checked for impingement between the humeral and scapular sides of the joint by performing intersection Boolean operations (Figure 3.1).

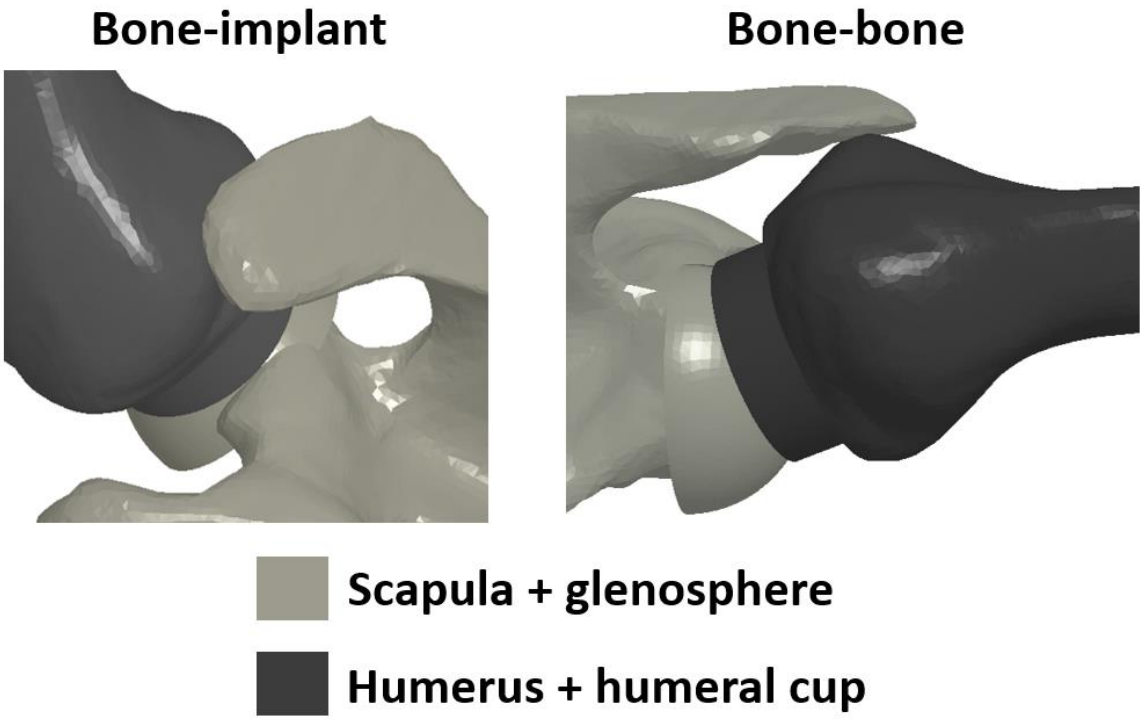

Figure 3.1. Impingement, whether bone-implant (left) or bone-bone (right) was detected by performing Boolean operations between the humeral and scapular sides of the joint, which each consisted of bone and respective implant components treated as monoblocs.

3.1.1.b Experimental Validation Procedure

The technique for predicting impingement computationally was experimentally verified using a VIVO six degree-of-freedom joint motion simulator (Advanced Mechanical Technology, Inc., Watertown, MA). The humerus and scapula were 3D printed as monoblocs out of ABS plastic with their respective implant components, as well as custom fixtures for attachment to the joint simulator (Figure 3.2), using a uPrint SE (Stratasys Ltd., Eden Prairie, MN).

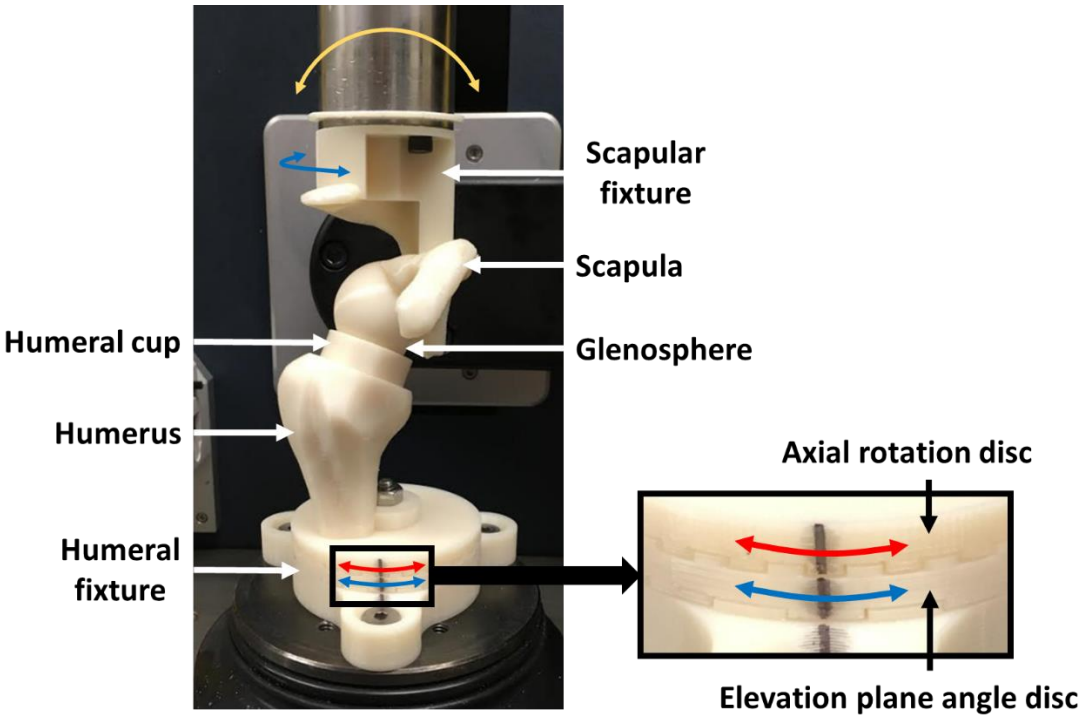

Figure 3.2. The bones/implants/attachment fixtures were 3D printed as monoblocs such that the elevation axis was pre-aligned with a rotational axis on the VIVO (left). Elevation plane angle and axial rotation angle were varied manually through the use of a series of grooved and toothed discs (right).

Manually rotating the fixtures on the machine varied elevation plane angle (rotation of humerus and scapula) and axial rotation angle (rotation of humerus only) by corresponding increments using series of grooved and toothed discs designed to rotate the components by the desired amount (Figure 3.2). The fixtures were designed such that the axis for elevation in the computational model was pre-aligned with a rotational axis on the VIVO. The same motions applied to the computational model were repeated experimentally using displacement control of the joint simulator with a 15 N compressive force on the joint. The point of first impingement was detected as a sudden change in the elevation moment measured by the VIVO and was confirmed via visual inspection. The elevation angle at which impingement first occurred was recorded for comparison with computational results.

3.1.2 Validation Results and Discussion

Table 3.1 compares impingement position predictions of the experimental and computational models for the same implant design. Note that experimental results are continuous, whereas the computer model detects impingement in discrete 10° elevation increments. Experimental and computational results showed agreement in in 54% of the cases investigated (i.e. the experimentally measured impingement angle fell within the 10° uncertainty interval of the model-predicted impingement angle 54.2% of the time). However, in roughly one third of the cases where disagreement was observed (4/11), the experimental prediction fell on the upper limit of the computational range in which impingement was detected. Additionally, the experimental prediction fell outside of the computational uncertainty interval by greater than 3° in only 8.3% of cases. Discrepancies are likely due to slight misalignment of motion axes as a result of error introduced by tolerances in the additive manufacturing techniques (± 0.2 mm) used to fabricate the components.

Table 3.1. Computational and experimental predictions for elevation angles at which impingement was first detected in a subset of motions studied. Note: impingement was checked at 10° increments computationally, and the corresponding ranges in which impingement was first detected are presented, where β represents elevation angle.

Elevation plane angle	**Rotation angle**					
	-30°		*0°*		*30°*	
	Comp.	*Exp.*	*Comp.*	*Exp.*	*Comp.*	*Exp.*
-90°	$0° \leq \beta < 10°$	10°	$10° \leq \beta < 20°$	19°	$10° \leq \beta < 20°$	23°
-60°	$0° \leq \beta < 10°$	16°	$20° \leq \beta < 30°$	36°	$30° \leq \beta < 40°$	39°
-30°	$80° \leq \beta < 90°$	90°	$100° \leq \beta < 110°$	104°	$120° \leq \beta < 130°$	124°
0°	$80° \leq \beta < 90°$	85°	$80° \leq \beta < 90°$	89°	$90° \leq \beta < 100°$	101°
30°	$80° \leq \beta < 90°$	90°	$80° \leq \beta < 90°$	84°	$80° \leq \beta < 90°$	90°
60°	$100° \leq \beta < 110°$	96°	$80° \leq \beta < 90°$	78°	$60° \leq \beta < 70°$	63°
90°	$80° \leq \beta < 90°$	84°	$60° \leq \beta < 70°$	67°	$30° \leq \beta < 40°$	37°
120°	$70° \leq \beta < 80°$	68°	$50° \leq \beta < 60°$	52°	$30° \leq \beta < 40$	34°

3.2 Muscle Capability

3.2.1 Background

Evaluating the viability of the muscles to produce a distribution of forces sufficient to maintain any given static arm position relies on the use of a musculoskeletal model and the static optimization tool in OpenSim. As outlined in section 2.4.2, the force-generating capability of any muscle is dependent on its moment arm and musculotendon dynamics, both of which are partly a function of the path a musculotendon unit takes from origin to insertion. Paths in the Holzbaur et al.[24] musculoskeletal model are determined using a combination of prescribed via points and rudimentary wrapping geometry. These were selected based on validating moment arms within the limits of the motion coordinates prescribed in the model, which were -90° to 130° for elevation plane angle, 0° to 180° for elevation angle, and -90° (external) to 20° (internal) for axial rotation angle.

Although the model performs well within these limits for the anatomic shoulder, evaluating the effect of rTSA design on muscle action presents several challenges related to capturing the effect of implantation on muscle paths. As a result of implanting rTSA, not only are there additional geometries for the muscles to wrap over, but the position of the humerus is shifted. Simply adding wrapping geometries to represent the implant and moving the via points and existing wrapping geometries associated with the humerus by the corresponding transformation does not guarantee anatomical muscle paths within the same limits of motion as the anatomic shoulder. For example, the muscles may wrap the incorrect way around the humeral shaft, or wrapping geometries representing the implant components may be ignored entirely if intersected by a via point. These types of occurrences would be impossible to regulate, especially given the automated nature of

design optimization. Additionally, in evaluating ROM of rTSA, internal rotation angles of greater than 20° should be analyzed.

These factors necessitated the development of a more reliable method of determining muscle paths throughout the comprehensive ROM resulting from implantation of variable rTSA designs without sacrificing computational efficiency such that design optimization (even using a surrogate model) became impossible. Therefore, an FE model capable of predicting muscle paths throughout the ROM in the presence of variable implant geometry was developed for use in evaluating muscle capability using static optimization in OpenSim. The model was validated based on experimental and computational moment arm data available in the literature first for the anatomic shoulder and then for one implanted with a representative rTSA configuration.

3.2.2 Methods

3.2.2.a Computational Model Development for the Anatomic Shoulder

The STL surface files from of the clavicle, scapula, and humerus used in the development of the impingement model were converted into solid geometries using SolidWorks 2014 (Dassault Systèmes, Waltham, MA). Each bone was treated as a rigid body and meshed with quadratic tetrahedral elements (C3D10M) with an average element edge length of 2.5 mm using the commercially available finite element analysis pre-processor software Abaqus/CAE 6.14 (Dassault Systèmes, Waltham, MA). The coordinate systems, initial positions and orientations of the bones, and locations of musculotendon origin and insertion points were defined as those given in the Holzbaur et al.[24] musculoskeletal model. Four muscles of the rotator cuff (supraspinatus, infraspinatus, subscapularis, and teres minor) and three deltoid bundles (anterior, middle, and posterior)

were modeled using a “string-of-pearls” representation. Each muscle consisted of a series of 15 rigid spheres, each 10 mm in diameter and meshed with quadratic tetrahedral elements (C3D10M) with an element edge length of 3 mm. Sphere centers along each muscle bundle were initially separated by 3 mm and connected by 1-D point-to-point linearly elastic springs (Figure 3.3). Each muscle bundle was pinned at its origin on the scapula (clavicle for the anterior deltoid) by constraining all translational degrees of freedom (DOF). Wrapping patterns were calculated using an explicit solver (Abaqus/Explicit). Initially, the muscle bundles were oriented in space in a manner that minimized contact between the spheres (other than the one representing the origin) and bone, and avoided contact between distinct muscle bundles. During the initial wrapping step, the free (distal) ends of each muscle were pulled to their respective insertion sites on the humerus using one-DOF translational connectors (Figure 3.3).

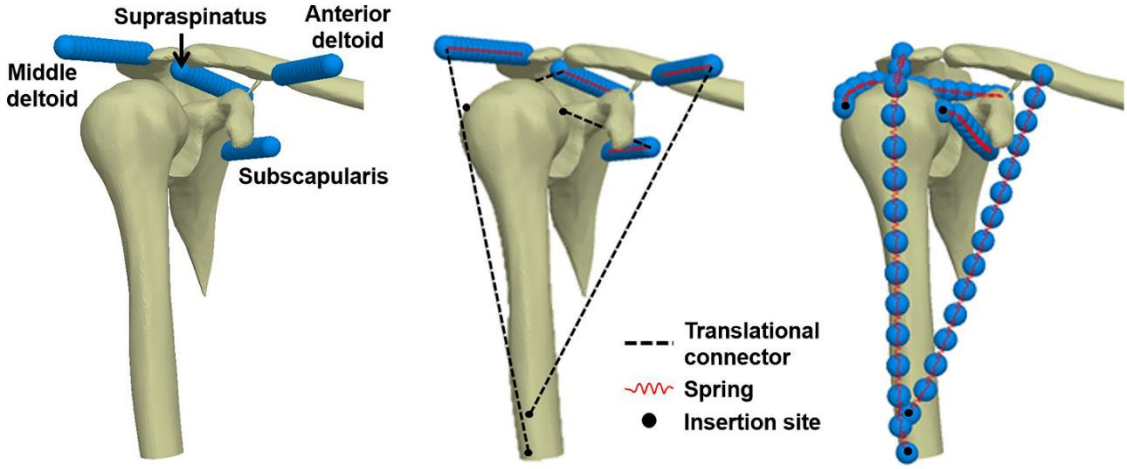

Figure 3.3. The sequence of the initial wrapping step, where “string-of-pearls” muscle representations initially attached at their origins (left) were connected at their centers by springs and pulled to their insertions by 1 degree of freedom translational connectors (middle), resulting in paths dictated by wrapping over bony geometry (right). Note: for clarity, not all modeled muscle bundles are shown.

The Abaqus default “hard” pressure-overclosure relationship for normal contact and frictional tangential contact was modeled at all sphere-bone interfaces, such that the

muscle bundles wrapped over bony geometry as their free ends were pulled to the insertion sites. To reduce computational cost, sphere-sphere contact was not considered. Variable model parameters included material properties, the spring constant of the springs connecting the contact spheres, and friction coefficient. Material properties of all bones and contact spheres were defined as that of cortical bone with a density of 2.5 mg/mm^3, an elastic modulus of 17 GPa, and Poisson's ratio of 0.3. Each spring was assigned a spring constant of 1 N/mm and the coefficient of friction between the spheres and bones was 0.15.

3.2.2.b Motions

Following the initial wrapping step, motions were applied to the FE model, the definitions of which are the same as those used in the Holzbaur et al.[24] musculoskeletal model and the computational impingement model. The sequence of motions applied to the FE model (as with the impingement model) was always in the order of axial rotation first, followed by elevation within a given elevation plane. As the shoulder was manipulated through the prescribed motions, the simulated muscle bundles continued to wrap and glide across the surfaces of the bones while spanning from origin to insertion. Elevation moment arm data was available in the literature for continuous abduction and flexion[24,60,61], as well as discrete positions of 30° and 60° of scaption[62,63], all with the arm in neutral rotation. Axial rotation moment arms were available for the arm at neutral elevation[24,60,62,64] and 30°, 60°, 90°, and 120° of abduction and flexion[65]. As such, these motions were applied to the bones in the anatomic FE model to allow for comparison.

3.2.2.c Muscle Wrapping After rTSA

The bones in the FE model were then implanted with the same representative rTSA configuration used in the impingement model (a glenosphere diameter of 36 mm and NS

angle of 155°). The muscle wrapping step was repeated as previously described for the anatomic case, and motions for which moment arm data was available after rTSA in the literature were applied. The motions included abduction and flexion[66], as well as axial rotation with the arm at neutral[64] and 30°, 60°, 90°, and 120° of abduction and flexion[67].

3.2.2.d Data Analysis: Determination of Muscle Moment Arms from FE Model Results

A custom algorithm in MATLAB 2014b was used to query FE results at a series of static positions throughout continuous motions. For any given position, the global coordinates of the center of any sphere in contact with a bone were processed into the coordinate systems of the bone with which they were in contact. The locally defined coordinates of contact spheres were used to define the locations of via points in an adapted version of the Holzbaur et al.[24] musculoskeletal model in OpenSim 3.3, which was used to calculate moment arms. For clarity, wrapping patterns were simulated in the FE model throughout continuous motions, and muscle moment arms at discrete instances within that motion were calculated in OpenSim. Abduction, flexion, and scaption were applied directly (i.e. accomplished with a single simulation), while axial rotation at varying levels of abduction and flexion was not applied directly as a continuous motion, but as a combination of motions within which the desired positions were included. In other words, the arm was first incrementally axially rotated, after which it was abducted or flexed, and the results were processed at the desired elevation levels (as opposed to elevating to the desired level and then axially rotating).

3.2.2.e Validation Approach

Moment arms computed by the current FE model-based technique were compared with previous experimental and simulation results to assess model validity. Moment arm

data that was presented graphically in previously published work was manually digitized using an open-source program (PlotDigitizer, University of Southern Alabama). Qualitative assessments were performed using graphical representations of previous and current moment arm data.

Quantitative assessments were performed between the FE model moment arm data generated using the musculoskeletal model by Holzbaur et al.[24], as well as a subset of experimental studies, namely those that provided data before and after rTSA[66,67]. Average root-mean-square (RMS) error between moment arms predicted by the current FE model and the musculoskeletal model by Holzbaur et al.[24] were calculated for the anatomic shoulder throughout abduction and flexion. An analysis of moment arm trends in the anatomic shoulder was conducted by calculating Pearson correlation coefficient values for each muscle throughout abduction and flexion between moment arms from studies by Ackland et al.[61] and moment arms from both the current FE model as well as the musculoskeletal model by Holzbaur et al.[24]. Additionally, Pearson correlation coefficient values were calculated to compare data from the current FE model to that from studies by Ackland et al.[66,67] before and after rTSA for abduction, flexion, and axial rotation at 30°, 60°, 90°, and 120° of abduction and flexion. For axial rotation at varying levels of abduction and flexion, the data comparison was consolidated by calculating a single Pearson correlation coefficient value for each muscle with the different combinations of elevation plane and pre- or post-operative status. For example, for one muscle, a total of four Pearson correlation coefficient values were calculated: anatomic abduction, anatomic flexion, implanted abduction, and implanted flexion, where all levels of elevation in each plane were included.

It should be noted that data was not available for all muscles included in the FE model for all studies. Conversely, in several studies data was reported for more than one portion of a muscle. If muscle bundles were identified, comparisons were made between whichever bundle was best represented by the present FE and musculoskeletal models. Bundles of the rotator cuff muscles represented by the current model were identified as the anterior supraspinatus, inferior infraspinatus, superior subscapularis, and inferior teres minor.

3.2.3 Validation Results and Discussion

The following sections will present and discuss the results of the FE model validation procedure and will proceed by motion type in the order of scaption, abduction, flexion, and finally axial rotation neutral, as well as varying levels of abduction and flexion. If data after rTSA implantation was available for a specific motion, it will be presented and discussed following that available for the anatomic shoulder. Finally, model limitations and conclusions pertaining to model development and validation will be discussed.

3.2.3.a Scaption

Elevation moment arms calculated for the anatomic shoulder at 30° and 60° of glenohumeral (GH) scaption for four rotator cuff muscles are shown in Figure 3.4. For comparison, ranges of previously reported values from seven experimental studies and seven computational models (reported by Gatti et al.[63] and Favre et al.[62]), as well as symbols representing each individual study are included.

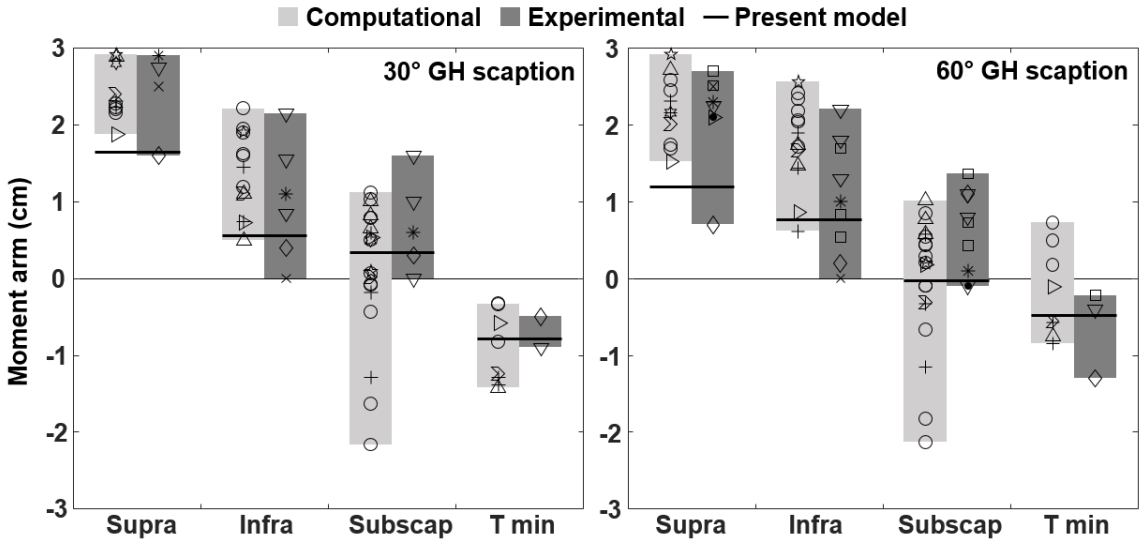

Figure 3.4. Muscle moment arms of the rotator cuff muscles predicted by the present FE model in comparison to previously published experimental and computational results at 30° (left) and 60° (right) of glenohumeral (GH) scaption. Note: each symbol represents a different study, some of which reported moment arms for multiple bundles of one muscle.

The present FE model predicted muscle paths that resulted in moment arms of the rotator cuff muscles that generally fell within the ranges of both experimental and computational studies[62,63]. The exception is the supraspinatus, which fell only in the range of experimentally determined values for both positions. The broad ranges of computational moment arms for the subscapularis at both positions are likely a result of its broad attachment footprint on the anterior portion of the scapula and the selection of the modeled or measured portion(s) in each of the studies.

3.2.3.b Abduction

Elevation moment arms for all seven muscle bundles represented in the current (anatomic shoulder) model are compared to one experimental study (Ackland et al.[61,66]) and two computational models (Holzbaur et al.[24] and Webb et al.[60]) in Figure 3.5 for abduction from 0° to 90°. Note that Webb et al.[60] included volumetric, multi-fiber representations of muscles, and therefore the range of moment arms for all fibers composing each muscle is depicted.

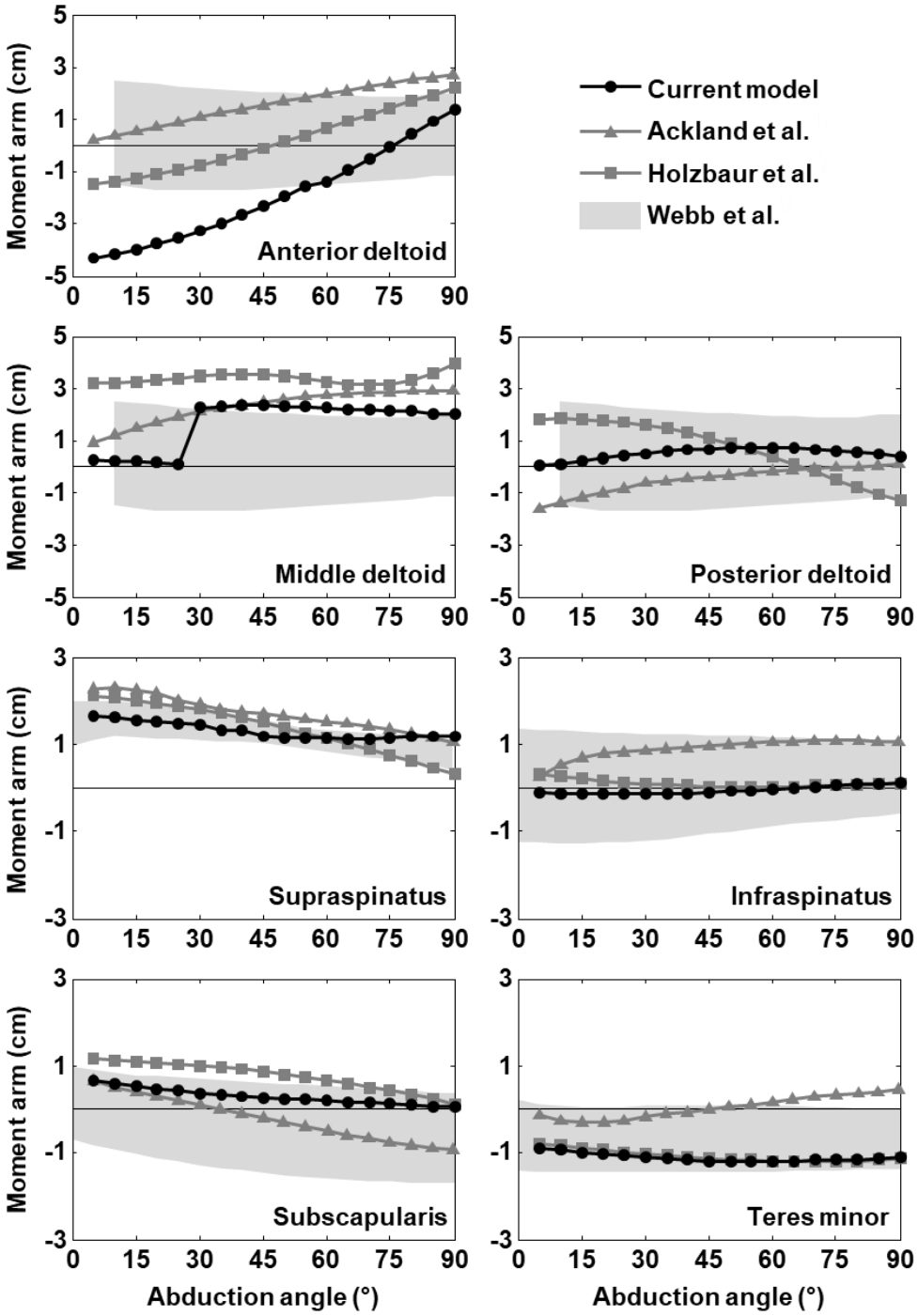

Figure 3.5. Elevation moment arms of the seven muscle bundles represented by the present FE model in comparison to previously published results[24,60,61,66] from 0° to 90° of abduction.

Pearson correlation coefficient values between data by Ackland et al.[66] and both the current FE model and the musculoskeletal model by Holzbaur et al.[24] are shown in Table

3.2 for elevation moment arms throughout abduction. The average RMS errors between the FE model predicted moment arms and the moment arms generated using the musculoskeletal model by Holzbaur et al.[24] are as follows: 2.2, 1.9, 1.2, 0.4, 0.2, 0.5, and 0.1 cm for the anterior deltoid, middle deltoid, posterior deltoid, supraspinatus, infraspinatus, subscapularis, and teres minor, respectively.

Table 3.2. Pearson correlation coefficient values comparing moment arms from Ackland et al.[66] with the current FE model for abduction and flexion of the shoulder before and after rTSA implantation as well as moment arms from the musculoskeletal model by Holzbaur et al.[24] for the anatomic shoulder through abduction and flexion. Note: '-' indicates that no data was available for the corresponding combination of muscle, motion, and implantation status.

		A. delt	M. delt	P. delt	Supsp	Infsp	Subscap	T min
Anatomic abduction	**FE model**	0.98	0.85	0.80	0.89	0.62	0.99	-0.62
	Holzbaur et al.[24]	0.99	0.25	-0.86	0.98	-0.93	0.96	-0.80
Anatomic flexion	**FE model**	-0.27	0.78	-0.98	-0.97	-0.62	-0.81	-0.94
	Holzbaur et al.[24]	-0.55	0.68	0.84	-1.00	-0.80	-0.94	-0.80
Implanted abduction	**FE model**	0.95	0.97	0.60	-	-	0.08	-
Implanted flexion	**FE model**	0.73	0.97	0.58	-	-	-0.72	-

In general abduction moment arms for all muscle bundles in the anatomic shoulder fell within, or very close to, the range of moment arms determined by Webb et al.[60], with the exception of the anterior deltoid (Figure 3.5). The present FE model predicted that the anterior deltoid was an adductor until roughly 80° of abduction. Experimental results from Ackland et al.[61] and computational results from the model by Holzbaur et al.[24] indicate that the anterior deltoid is either always an abductor, or transitions to one earlier in abduction. However, all results agree that the contribution of the anterior deltoid to abduction increases with abduction angle, evidenced by the Pearson correlation coefficient values

close to one in Table 3.2. Discrepancies in the moment arms of the anterior deltoid could be attributed to the complications in muscle wrapping imparted by the acromion on the scapula. In general, the changes in moment arms of the anatomic shoulder throughout abduction are captured well by the FE model when comparing to the experimental data by Ackland et al.[61] (Table 3.2), except for teres minor. The model by Holzbaur et al.[24] exhibits strong negative correlations for the posterior deltoid, infraspinatus, and teres minor.

Ackland et al.[66] reported abduction moment arms for three bundles of the deltoid and the subscapularis before and after rTSA implantation. Comparisons of these to the current model are shown in Figure 3.6. It should be noted that pre-operative data is the same as that presented in Figure 3.5. Pearson correlation coefficient values before and after implantation are shown in Table 3.2. Implantation of the shoulder with rTSA caused average moment arm increases of 1.2, 1.3, and 1.2 cm for the anterior, middle, and posterior deltoid, respectively in comparison to the anatomic shoulder using the current FE technique.

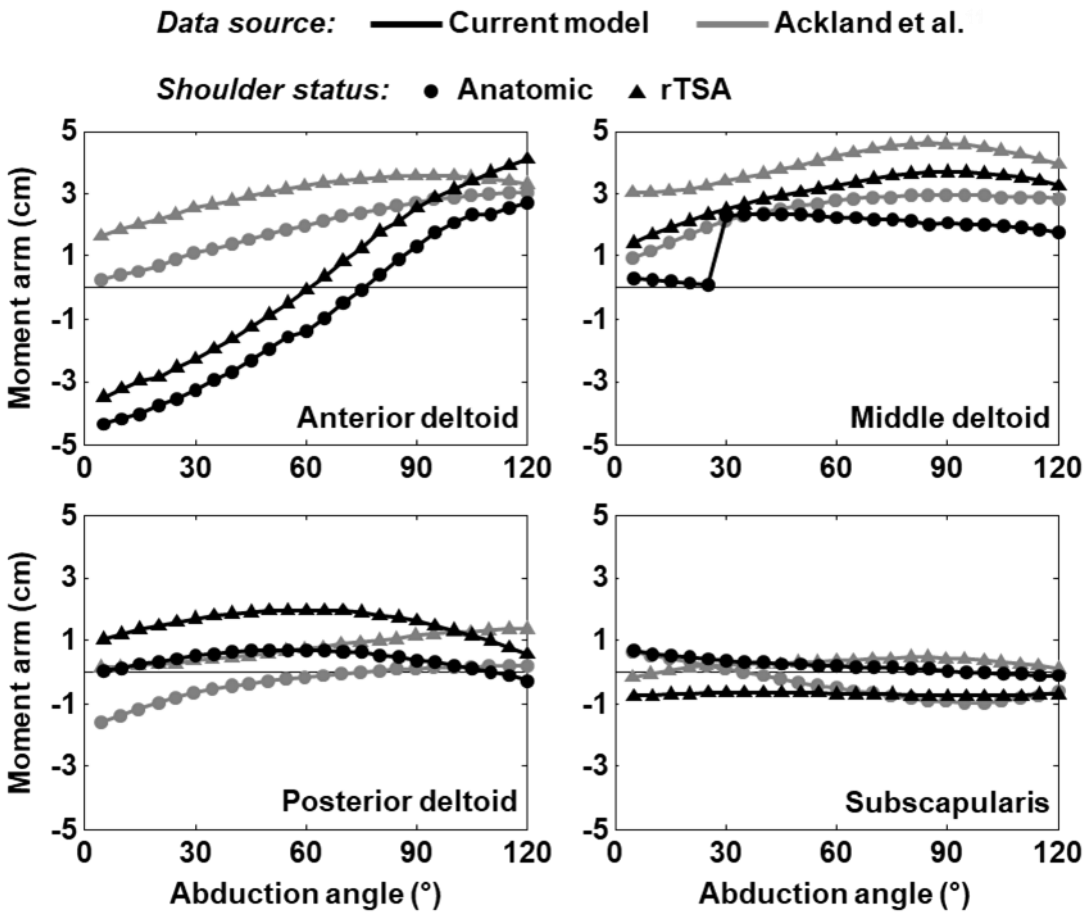

Figure 3.6. Elevation moment arms for the anterior deltoid (top left), middle deltoid (top right), posterior deltoid (bottom left), and subscapularis (bottom right) before (circles) and after rTSA implantation (triangles) during abduction. Black lines indicate predictions of the current model and grey lines represent experimental data from Ackland et al.[66].

The effects of rTSA on the abduction moment arms of the deltoid are in good agreement, where strong positive correlations and universal increases in the abduction moment arms are observed between 0°-120° of abduction (Table 3.2 and Figure 3.6). For the anterior and middle deltoid, Ackland et al.[66] observed mean moment arm increases of 1.1 and 1.6 cm, respectively, across eight cadaveric specimens after rTSA versus 1.2 and 1.3 cm increases, respectively, in the present model. These findings agree with the biomechanical premise of rTSA, where medializing the COR of the joint is meant to

increase the abduction moment arms of the deltoid, thereby reducing the required force generation.

3.2.3.c Flexion

Pearson correlation coefficient values are shown for all muscles in Table 3.2 comparing elevation moment arms during flexion from Ackland et al.[61,65] to moment arms generated using the current FE model and the musculoskeletal model by Holzbaur et al.[24] for the anatomic shoulder. Average RMS errors between the moment arms from the two computational models were 2.2, 1.3, 0.9, 0.8, 0.4, 0.2, and 0.1 cm for the anterior deltoid, middle deltoid, posterior deltoid, supraspinatus, infraspinatus, subscapularis, and teres minor, respectively.

Ackland et. al[66,67] also reported elevation moment arms of the deltoid bundles and subscapularis after rTSA implantation, for which comparisons are shown in Table 3.2 and Figure 3.7. The current model predicted average increases of 1.3, 1.2, and 0.9 cm in the flexion moment arms of the anterior, middle, and posterior deltoid, respectively, following implantation of rTSA.

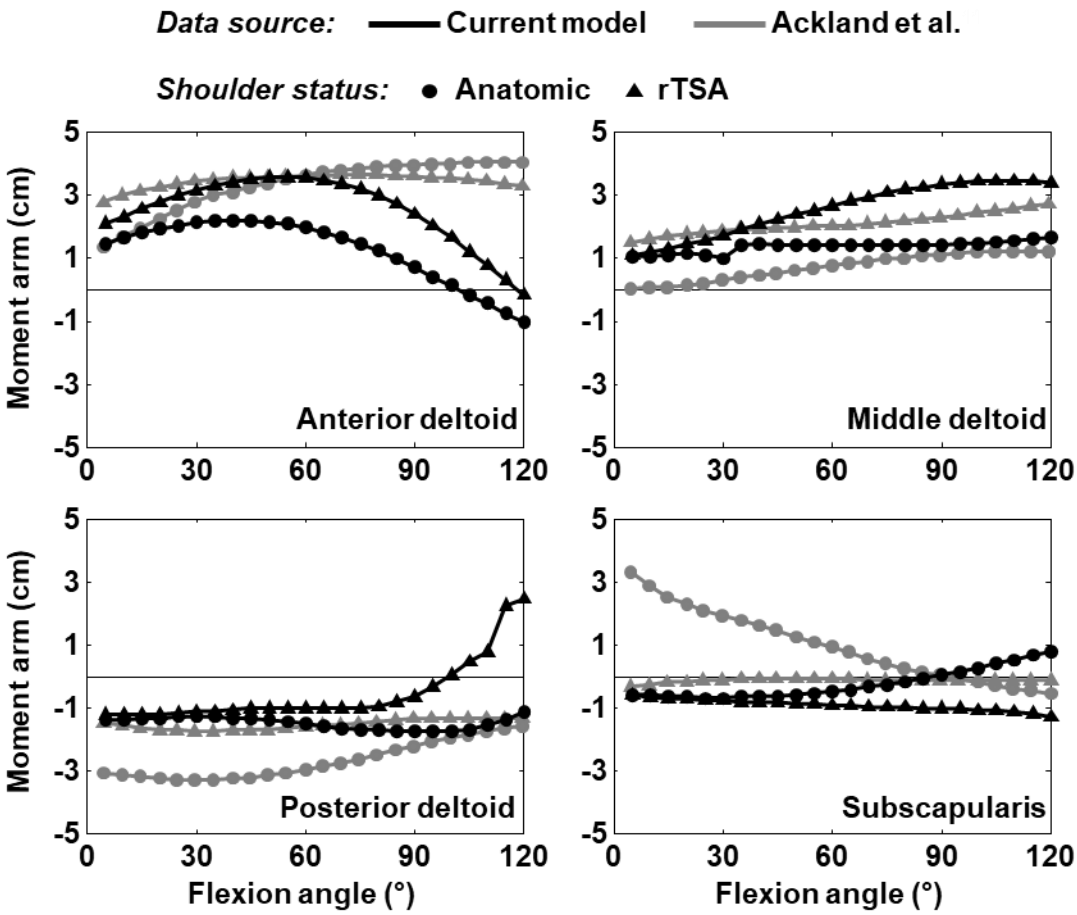

Figure 3.7. Elevation moment arms for the anterior deltoid (top left), middle deltoid (top right), posterior deltoid (bottom left), and subscapularis (bottom right) before (circles) and after rTSA implantation (triangles) during flexion. Black lines indicate predictions of the current model and grey lines represent experimental data from Ackland et al.[66].

Although some negative correlations were observed for flexion of the anatomic shoulder between Ackland et al.[61] and both the FE model and the musculoskeletal model by Holzbaur et al.[24], the RMS errors between the FE and musculoskeletal model showed reasonable agreement. Additionally, moment arm trends in flexion following rTSA were in good agreement with Ackland et al.[66] (Table 3.2). Mean increases of the middle deltoid moment arm were 1.4 and 1.2 cm in the study by Ackland et al.[66] and the present model, respectively, after rTSA. The present model indicates that there is increased contribution of the anterior deltoid to flexion throughout the motion after rTSA, whereas Ackland et

al.[66] predicts more contribution of the anterior deltoid in natural anatomy after about 60°. Both experimental and computational results indicate decreased contribution of the posterior deltoid to extension following rTSA implantation.

3.2.3.d Axial Rotation at Neutral Elevation

Axial rotation moment arms predicted by the FE model in comparison to moment arms predicted by four other computational models[24,60,62,64] are shown in Figure 3.8.

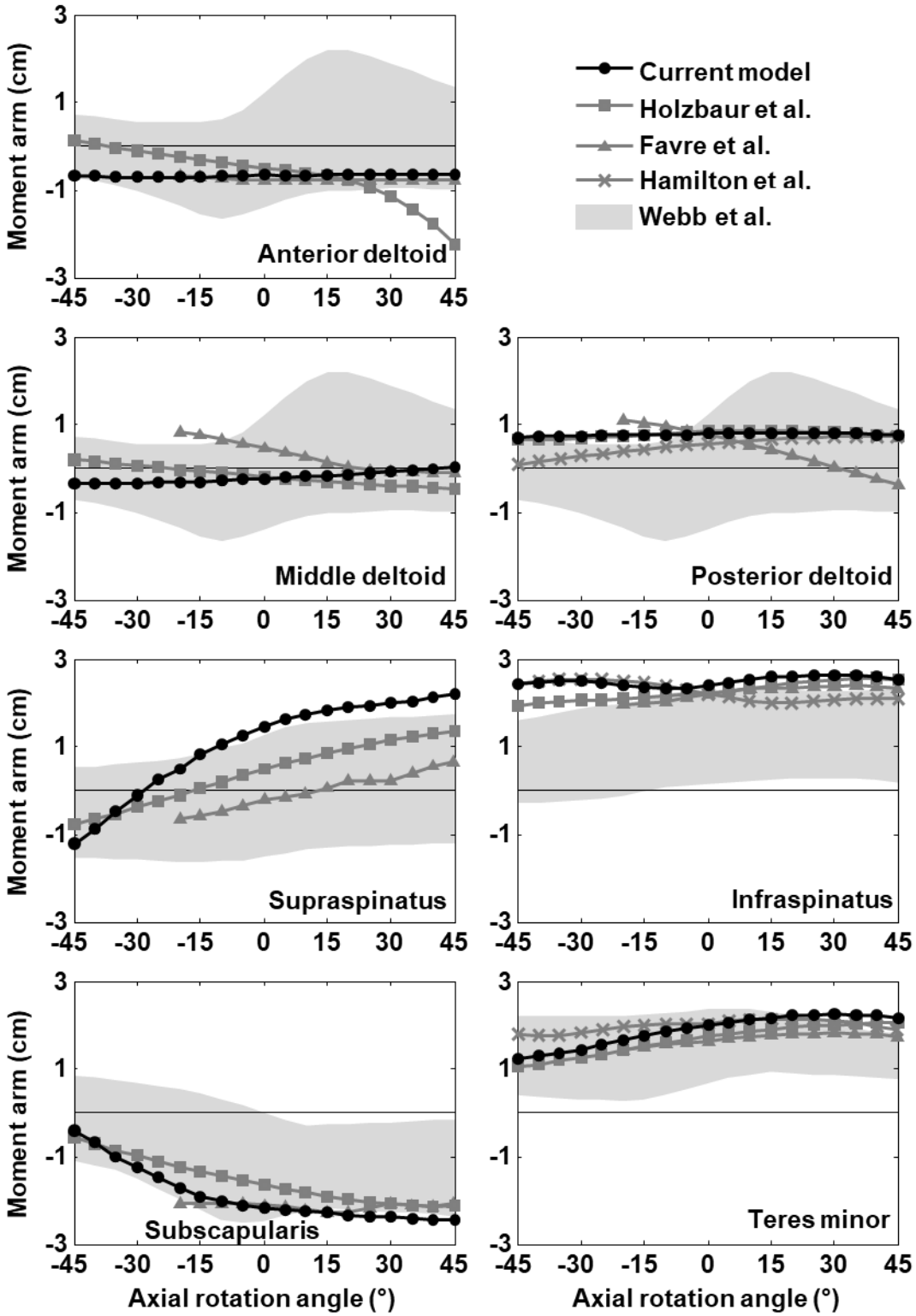

Figure 3.8. Axial rotation moment arms of the seven muscle bundles represented by the present FE model in comparison to previously published results[24,60,62,64] rom 45° internal rotation to 45° external rotation with the arm at neutral elevation. Negative joint angles and moment arms indicate internal rotation.

Hamilton et al.[64] reported axial rotation moment arms of the external rotators, namely the posterior deltoid, infraspinatus, and teres minor, before and after implantation of several different configurations of rTSA. The implant configuration that best matched the one used in this study was chosen for comparison. Moment arms before and after implantation are shown in Figure 3.9.

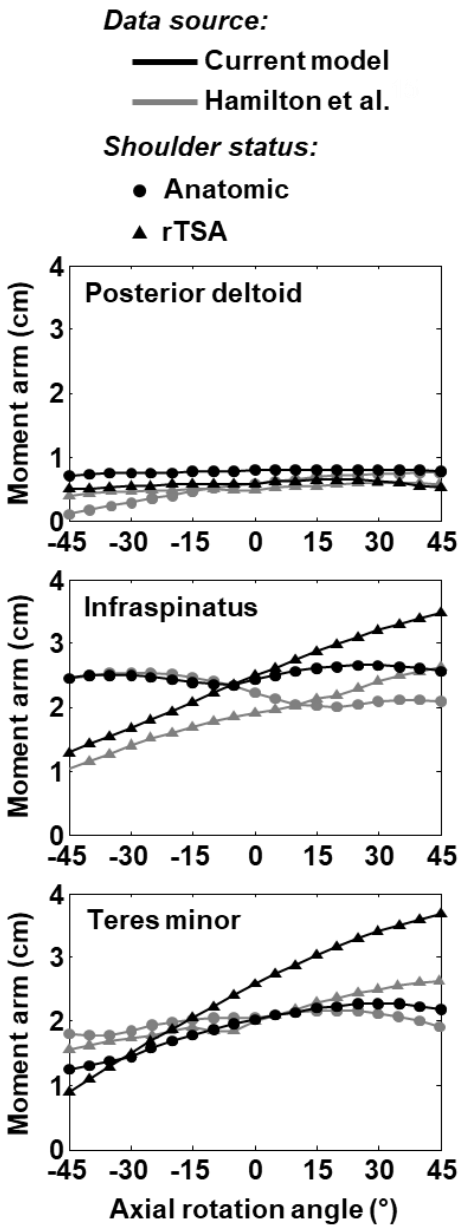

Figure 3.9. Rotation moment arms for the posterior deltoid (top), infraspinatus (middle), and teres minor (bottom) before (circles) and after rTSA implantation (triangles). Black lines indicate predictions of the current model and grey lines represent experimental data from Hamilton et al.[64]. Positive joint angles and moment arm values represent external rotation.

Similarly to abduction, axial rotation moment arms with the arm at neutral elevation of all seven muscle bundles represented by the present FE model fell within, or close to the range of moment arms presented by Webb et al.[60] (Figure 3.8). The FE model by Favre et al.[62] predicts greater changes in moment arms of the middle and posterior deltoid with

changes in joint angle than either the present model or the model by Holzbaur et al.[24]. In contrast, the Holzbaur et al.[24] model shows greater variation in the moment arm of the anterior deltoid with changes in joint angle than do the present model and that by Favre et al.[62], which both agree with findings by Webb et al.[60].

Good agreement for the infraspinatus, subscapularis, and teres minor is observed between the present model and all other models used for comparison, where the infraspinatus and teres minor are the dominant external rotators of the rotator cuff, while the subscapularis is the dominant internal rotator. All models also show that the supraspinatus transitions from an internal to external rotator between 45° of internal to external rotation, although there is disagreement regarding the position at which this happens.

A model by Hamilton et al.[64], in which muscle paths were determined by identifying contact points between muscles and bones, was used to determine rotation moment arms of the external rotators before and after rTSA implantation (Figure 3.9). The effects of rTSA on the external rotation moment arms of the posterior deltoid are small in comparison to the infraspinatus and teres minor. In both the present model and the model by Hamilton et al.[64], the contributions of the infraspinatus and teres minor to external rotation after rTSA surpass those in natural anatomy with increasing external rotation angle. However, the current model indicates that this occurs before neutral axial rotation when moving from internal to external rotation. This indicates that the efficacy of rTSA in maintaining or restoring external rotation may depend specifically on the condition the infraspinatus and teres minor, as restoration of external rotation with rTSA is a known problem[15]. This would be dependent on post-operative muscle lengths and whether they

fall within the operating range of the force-length curves, as rTSA may slacken remaining rotator cuff muscles by medializing the COR.

3.2.3.e Axial Rotation at Varying Levels of Abduction and Flexion

Pearson correlation coefficient values are shown in Table 3.3 for FE model predicted moment arms versus those reported by Ackland et al.[66,67] in experimental studies reporting axial rotation moment arms at varying levels of abduction and flexion before and after implantation of rTSA.

Table 3.3. Pearson correlation coefficient values comparing FE model and experimental[66,67] rotation moment arms from 45° internal rotation to 90° external rotation at elevation angles of 30°, 60°, 90°, and 120° of flexion and abduction for anatomic and implanted configurations. Note: for consolidation, rotation moment arms at all degrees of elevation in the respective elevation planes were concatenated and then analyzed.

		A. delt	**M. delt**	**P. delt**	**Supsp**	**Infsp**	**Subsc**	**T min**
Anatomic	**Abd**	-0.28	0.64	0.73	0.30	0.63	-0.21	-0.38
	Flex	0.53	-0.35	0.47	0.89	0.90	0.52	0.90
Implanted	**Abd**	0.35	0.77	0.09	0.86	0.28	0.77	0.22
	Flex	0.45	0.07	0.81	0.62	0.69	0.83	0.45

As shown in Table 3.3, the present model shows good correlation with results presented by Ackland et al.[65,67] regarding axial rotation moment arms of the shoulder muscles before and after rTSA with the arm at varying levels of abduction and flexion. Differing trends, represented by negative Pearson correlation coefficient values, were observed in the anterior deltoid, subscapularis, and teres minor during abduction, as well as the middle deltoid during flexion in the anatomic shoulder. In all other cases, positive correlations were observed for both the anatomic and implanted conditions, indicating that the present model was producing changes in moment arms consistent with the experimental data during axial rotation at varying degrees of abduction and flexion.

3.2.4 Validation Conclusions

Two possible sources for discrepancies in moment arms across the studies used for validation include size and shape variation of bony geometry. The model by Holzbaur et al.[24], from which the bone geometry for the present model was taken, used bones representative of a subject with the height of a 50th percentile male, or roughly 170 cm. Studies that used bony geometry from a cohort of subjects in which this specific demographic was not well represented may have determined resulted in different moment arm values. The present technique could easily be adapted to use bone geometries representing other subject populations to determine differences in muscle paths and moment arms resulting from both variable bone geometry and implantation.

The limitations of this model are inherent to using a line segment representation of muscle bundles, where it is not possible to capture variable contributions of an entire muscle. The rotator cuff muscles were represented by single bundles, because modeling multiple bundles per muscle would greatly decrease the computational efficiency of the model. However, given that the intended use of this technique is directly related to rTSA, the muscle of highest importance is the deltoid, which was represented by three bundles. Although muscle-bone interactions of individual fibers are likely close to frictionless, support that would be provided by surrounding fibers was simulated using frictional contact in order to constrain unrestricted slipping of muscle bundles over bony surfaces during motion, however large changes in moment arms were observed with small changes in joint angle in a limited number of scenarios where a muscle bundle first lost contact with a bone during a motion (i.e. the middle deltoid in Figure 3.5). In the interest of computational efficiency, interactions between different muscle fibers was not modeled,

when in reality, muscle paths may be affected (i.e. the deltoid must wrap over top of the rotator cuff). In the future, the effects of including these interactions should be studied.

The presented FE model provides a viable solution to predicting muscle paths throughout the complex motion of the shoulder in both the anatomic shoulder and one implanted with a reverse shoulder. The model shows acceptable agreement with results available in the literature for muscle moment arms of an anatomic and implanted shoulder and is easily adapted to incorporate varying bone and implant geometries. In the context of the objectives of this research, a tool was developed to allow for the evaluation of muscle capability in the context of ROM.

3.3 Stability

3.3.1 Background

In addition to the impingement model and the FE model from which muscle paths can be used in static optimization to determine the capability of the muscles, a tool to characterize the stability of the implant in the context of the JCFs resulting from muscle action was necessary. An analytical model to predict the amount of shear force required to dislocate a ball-and-socket geometry was validated both experimentally and with and FE model in order to ensure that it could be applied to the evaluation of joint stability in the context of physiologic muscle forces.

3.3.2 Methods

3.3.2.a Analytical Model

The analytical model, which is a modified version of one originally developed to assess stability of conventional TSA[43,68], relates shear force to dislocation (FTD) to

geometric parameters of ball-and-socket geometries (Figure 3.10), friction coefficient, and compressive force and is given by:

$$FTD = F_N * \frac{\tan(\theta)+\mu}{1-\mu*\tan(\theta)} \quad \text{Eq. (3.1)}$$

where F_N is the compressive force, θ is the incidence angle between the ball and the socket, and μ is the coefficient of friction between the materials. The incidence angle is given by:

$$\theta = \operatorname{atan}\left(\frac{\sqrt{\frac{2d}{R}-\left(\frac{d}{R}\right)^2}}{\left(1-\frac{d}{R}\right)}\right) \quad \text{Eq. (3.2)}$$

where d is the depth of the socket, and R is the matching radius of the ball and socket.

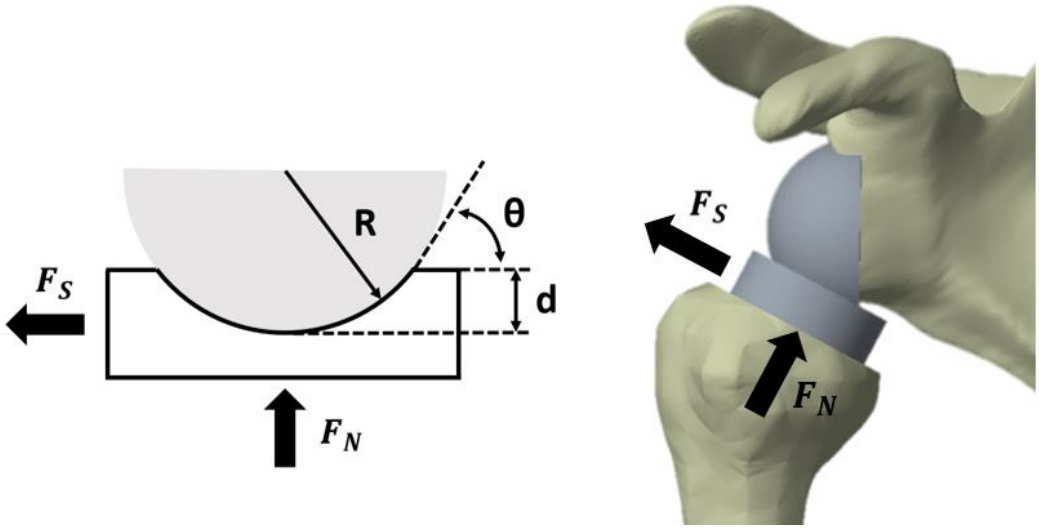

Figure 3.10. The parameters used in the analytical model to calculate the shear force require to dislocate the joint (F_S) as a function of compressive force and implant geometry.

3.3.2.b Validation Approach

Although the analytical model was validated by Gutiérrez et al.[43] for compressive loads up to 200 N, several studies have since found that compressive JCFs after rTSA may exceed this level, especially when lateralizing the joint COR[69-70]. Therefore, experimental and FE model validation was performed to ensure the validity of the mathematical model in the presence of compressive loads up to 600 N. Experimentally, a 38.1 mm diameter

stainless steel ball was mounted to a threaded rod, the protruding end of which was used for attachment to the VIVO. UHMWPE sockets with depths of 6, 9, and 12 mm were machined to match the curvature of the ball and attached to the VIVO using a custom fixture. Compressive loads ranging from 50-200 N in 50 N increments, as well as a 600 N load, were applied using deionized water to lubricate bearing surfaces. At each compressive loading level, pure shear displacements were applied to the socket in four orthogonal directions (Figure 3.11). Maximum shear force measured by the load cells on the VIVO was recorded. The shear FTD was taken as the average of the maximum shear forces across the four trials.

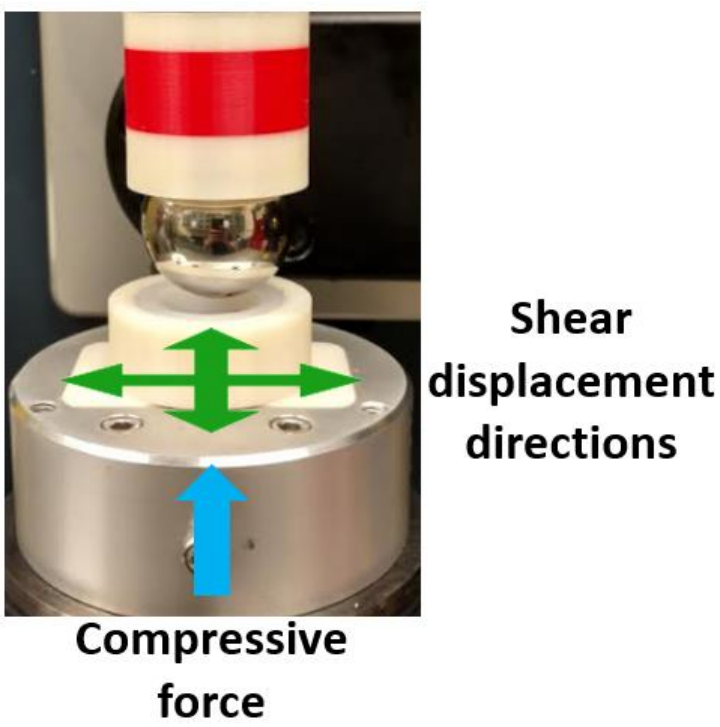

Figure 3.11. The experimental setup where varying levels of compressive force were applied and the socket was displaced in four orthogonal, pure shear directions.

An FE model replicating the experimental set-up was developed in Abaqus 6.14, where geometries were meshed with quadratic tetrahedral elements (C3D10M) with an average element edge length of 3 mm. Material properties of the ball were assigned as that

of 304 stainless steel: an elastic modulus of 200 GPa and Poisson's ratio of 0.29[71]. The UHMWPE cup was assigned an elastic modulus of 830 MPA and Poisson's ratio of 0.4[72]. The Abaqus "hard" normal pressure-overclosure and frictional contact with a coefficient of 0.05, that between polished stainless steel and UHMWPE lubricated with water[73], were used. The varying levels of compressive loads applied experimentally were simulated as a pressure applied to the flat surface of the socket opposite the articulating surface directed toward the ball. The socket was displaced in a pure shear direction and shear FTD was taken as the sum of nodal reaction forces in that direction.

The analytical equation was used to calculate shear FTD for the various geometrical configurations and loading levels and results were compared across all methods by calculating intra-class correlation (ICC) coefficients using a two-way mixed model checking for absolute agreement in SPSS 25 and percent differences.

3.3.3 Validation Results and Discussion

Results from all methods are shown in Figure 3.12. Average measures ICC coefficients were 0.94, 0.987, 0.981 and between the analytical and experimental, analytical and FE model, experimental and FE model results, respectively. Analyzing all three methods concurrently yielded an ICC coefficient of 0.98. The average percent differences in shear FTD across all loading levels between the analytical predictions and experimental results were 15.0 ± 10.7%, 18.0 ± 13.1%, and 23.5 ± 18.9% for 6, 9, and 12 mm socket depths, respectively. Similarly, average percent differences between experimental results and FE model predictions were 5.9 ± 4.9%, 9.4 ± 6.9%, and 11.8 ± 10.3% for 6, 9, and 12 mm socket depths, respectively.

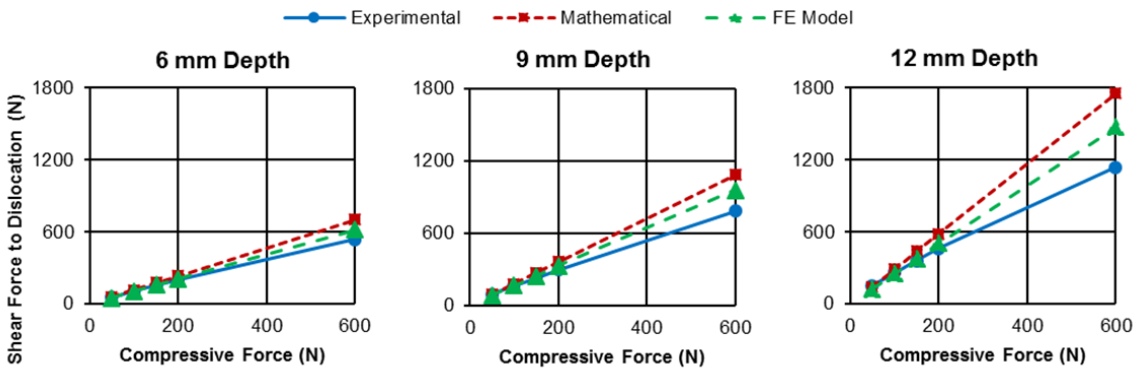

Figure 3.12. Shear FTDs predicted by the analytical and FE models and measured in the experiment at various compressive loading levels for sockets with depths of 6 mm (left), 9 mm (middle), and 12 mm (right).

Analytically predicted shear FTDs showed strong correlations with experimental and FE model results at all socket depths, with an ICC coefficient of 0.98 when analyzing all three methods concurrently. With a 6 mm socket depth, which was used for the implants investigated in this study, average differences of 15.0 ± 10.7% were observed across all compressive loading levels between mathematical and experimental results. FE model results were nearly always bounded by the alternate methods of shear FTD prediction (Figure 3.12), indicating that the mathematical model may not account for the effect of localized elastic deformation of the UHMWPE socket at the contact site, which is exacerbated at higher compressive loading levels.

Chapter 4. Development and Implementation of a Novel Metric for Characterizing Implant Performance Related to ROM

Subsequent to the development and validation of computational methods capable of analyzing impingement, muscle capability, and implant stability at variable arm positions, a metric to characterize ROM of any given implant configuration was developed. After conceptual development of the metric and implementation of the validated computational methods in its evaluation, it was calculated for a subset of variable implant parameters. This was to ensure that the metric (as well as the computational pipeline used in its determination) was sensitive to changes in implant design, such that it could be implemented in design optimization as the objective function.

4.1 Methods

4.1.1 ROM Metric

4.1.1.a Conceptual Development

The ROM of any given implant configuration is based on articulating the implanted bones through a set of continuous motions comprising the ROM of an anatomic shoulder and determining which portions of the motion envelope are eliminated by impingement, muscle incapability, or instability. The humerus is first axially rotated to angles between

90° internal and 90° external by increments of 15° at neutral elevation. At each rotation angle, the humerus is then elevated in planes with angles ranging from -90° (extension) to 120° by increments of 30°. Feasibility of static positions at 10° increments of elevation in each plane and rotation angle is determined based on each of the three arm position feasibility criteria.

For a given internal/external (IE) rotation angle, a map of the ROM can be generated on a unit sphere by plotting binary data indicative of feasibility at spherical coordinates corresponding to arm positions, where longitude represents elevation plane angle and latitude represents elevation angle[23]. Points at which the arm positions are feasible are connected to form regions, illustrated with an anatomic shoulder in Figure 4.1. The percent surface area of the sphere covered by the feasible region is calculated.

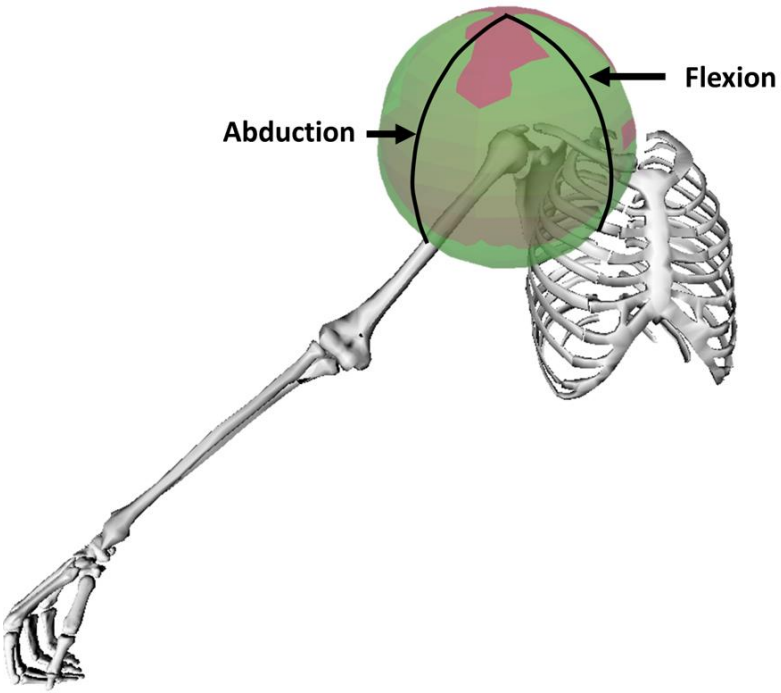

Figure 4.1. Maps of feasible ROM at different IE rotation angles are generated by connecting coordinates of feasible arm positions to form regions on the surface of a sphere, represented by green.

The percent surface area of the sphere covered by the feasible region is calculated. The same procedure is repeated at all IE rotation angles. Global circumduction ROM (GC-ROM) of an implant configuration is defined as the average feasible ROM across all rotation angles (Figure 4.2).

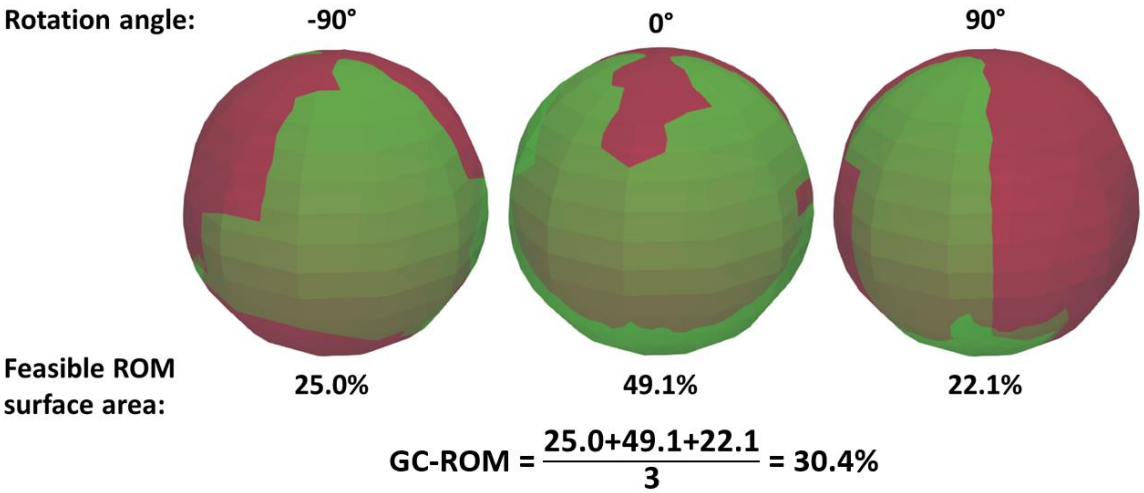

Figure 4.2. Global circumduction ROM (GC-ROM) is calculated as the average surface area covered by feasible regions, represented in green, across all IE rotation angles (90° internal and 90° external by increments of 15°).

For any implant configuration, a baseline ROM, that of the anatomic shoulder, is first narrowed by positions where impingement occurs. Within the maximum impingement-free limits, positions are then evaluated based on muscle capability and subsequently, stability. In other words, positions where impingement occurs are not evaluated based on any other criteria, and positions where the muscles are incapable of generating sufficient forces are not evaluated for stability. The general workflow for determining the ROM is shown in Figure 4.3.

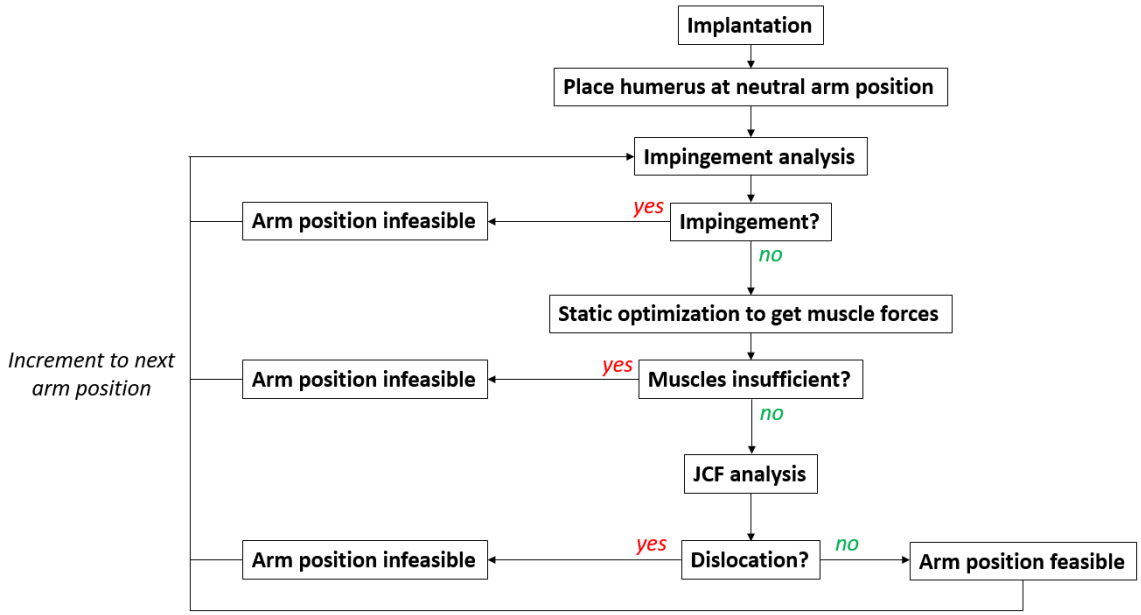

Figure 4.3. A flow chart outlining the progression through the various analyses implemented to determine ROM of any given implant configuration.

4.1.1.b Implementation of Validated Computational Methods in Determination of Arm Position Feasibility

The impingement criterion is evaluated via a straightforward implementation of the model described in section 3.1.1, where intersection Boolean operations are performed at each static position to check for interference.

Muscle capability is evaluated using the FE-to-musculoskeletal model technique described in section 3.2.1 to determine muscle paths at any given arm position. Once muscle paths from the FE model are implemented in an adapted version of the Holzbaur et al. musculoskeletal model, muscle forces are evaluated using the static optimization tool in OpenSim 3.3.

It should be noted that the muscle model implemented in the original Holzbaur et al.[24] model was the Schutte 1993 model[74], which does not account for force-velocity relationships. Therefore, the Millard 2012 Equilibrium muscle model[75], which offers improved formulations of force-length-velocity relationships, was substituted, but

physiologic scaling parameters (i.e. max isometric force, etc.) were consistent with the Holzbaur et al.[24] model.

Reserve actuators were used on each motion coordinate (elevation plane angle, elevation angle, and rotation angle) during static optimization. Reserve actuators are capable of producing torque, in addition to that from muscle action, in order to mitigate possible model "weaknesses" and torque imbalances at a joint that result from using line-segment representations of volumetric muscles. The muscle capability criterion is based on distinguishing which positions require excessive extra torque contribution in addition to what the muscles are able to provide. Any given arm position is considered infeasible if: the elevation angle reserve actuator contributes more than 5% of the total elevation joint torque, or either the elevation plane angle or axial rotation reserve actuators individually contribute more than 10% of the total elevation joint torque.

Joint stability of a given arm position is determined using Eq. 3.1 and Eq. 3.2 outlined in section 3.3.1. The sufficient muscle force configurations are used in conjunction with tools in OpenSim to conduct a JCF analysis. The JCFs are resolved into shear and compressive components in relation to the implant geometry/position. Using the compressive force, implant geometry parameters, and a coefficient of friction of 0.05 (UHMWPE on cobalt-chrome), the shear FTD is calculated. If the actual shear force component is greater than the calculated shear force required to initiate dislocation, then the corresponding arm position in considered infeasible.

4.2 Results: ROM metric for a subset of implant configurations

GC-ROM of nine candidate implant configurations was evaluated. The implant configurations consisted of combinations of three glenoid lateralizations (GLat) of 0, 5,

and 10 mm and three neck-shaft (NS) angles of 135°, 145°, and 155°, shown in Figure 4.4. GC-ROM was then calculated for each configuration based on the order in which the criteria were evaluated, i.e. impingement only, impingement and muscle capability, and impingement, muscle capability, and stability. As rTSA is most commonly performed to mitigate issues caused by a cuff tear, the subscapularis was the only rotator cuff muscle simulated when analyzing the active criteria, meaning that all other rotator cuff muscles had maximum isometric forces of zero in the musculoskeletal model. Fiber lengths and maximum forces of the middle deltoid and subscapularis were calculated with the arm in the neutral position, the purpose of which was two-fold: ensure the sensitivity of the computational pipeline for determining muscle forces to changes in implant design and to aid in assessing validity of trends in GC-ROM results. ROM in abduction and flexion through all rotations angles was plotted for one implant configuration (0 mm GLat, 155° NS angle) based on each limiting factor to illustrate the effect of rotation angle in a single elevation plane.

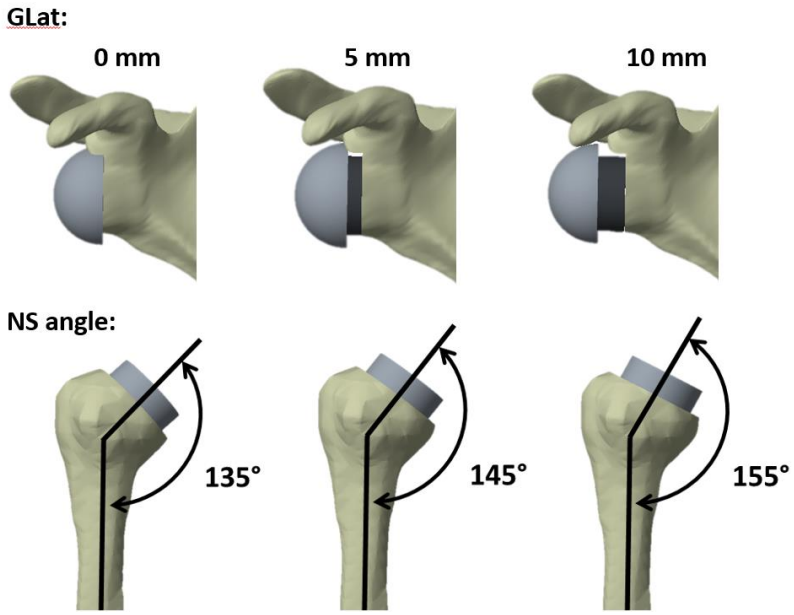

Figure 4.4. Nine implant configurations consisting of combinations of three glenoid lateralizations (top row) and three neck-shaft angles (bottom) row were evaluated for post-operative ROM.

Normalized fiber lengths and maximum possible forces for middle deltoid and subscapularis with the arm in the neutral position are shown in Table 4.1, as a function of implant configuration. Increasing GLat by 5 mm caused average increases of 9 N and 116 N in the maximum possible forces of the middle deltoid and subscapularis, respectively. Similarly, increasing NS angle by 5° caused an average increase of 13 N and decrease of 57 N for the maximum middle deltoid and subscapularis forces, respectively.

Table 4.1. Normalized fiber lengths and maximum possible force of the middle deltoid and subscapularis with the arm in the neutral position for the various implant configurations.

NS	***GLat = 0 mm***				***GLat = 5 mm***				***GLat = 10 mm***			
	M. deltoid		*Subscap.*		*M. deltoid*		*Subscap.*		*M. deltoid*		*Subscap.*	
	L_N	F_{max}	L_N	F_{max}	L_N	F_{max}	L_N	F_{max}	L_N	F_{max}	L_N	F_{max}
135°	91%	1,022 N	70%	887 N	92%	1,031 N	74%	1,018 N	94%	1,044 N	79%	1,071 N
145°	93%	1,039 N	68%	817 N	94%	1,046 N	72%	971 N	95%	1,056 N	77%	1,045 N
155°	95%	1,051 N	65%	733 N	95%	1,057 N	70%	887 N	96%	1,064 N	74%	1,015 N

The effect of the successive addition of ROM criteria on GC-ROM is shown in Figure 4.5. GC-ROM values were averaged across all IE rotation angles (13) that were simulated, and as such, the corresponding standard deviations were also calculated. GC-

ROM based on impingement ranged from 36.6 ± 13.1% to 43.8 ± 11.3%. Increasing GLat from 0 to 5 mm and 5 to 10 mm caused average increases in GC-ROM of 4.2% and 2.5%, respectively. There were no universal effects of varying NS angle on impingement-free ROM that were independent of GLat; in other words, the effect of NS angle was dependent on the value of GLat. However, including muscle capability and stability as ROM criteria results in distinguishable effects of varying NS angle, independent of GLat, and variable effects of GLat depending on NS angle. When all three criteria were considered simultaneously, GC-ROMs ranged from 5.1 ± 3.7% to 11.9 ± 5.5% with an average increase of 2.3% when increasing the NS angle by 10°. Increasing GLat from 0 to 5 mm resulted in an average GC-ROM increase of 2.0%. The effect of increasing GLat from 5 to 10 mm was dependent on NS angle, where a decrease in GC-ROM was observed in combination with a NS angle of 145°.

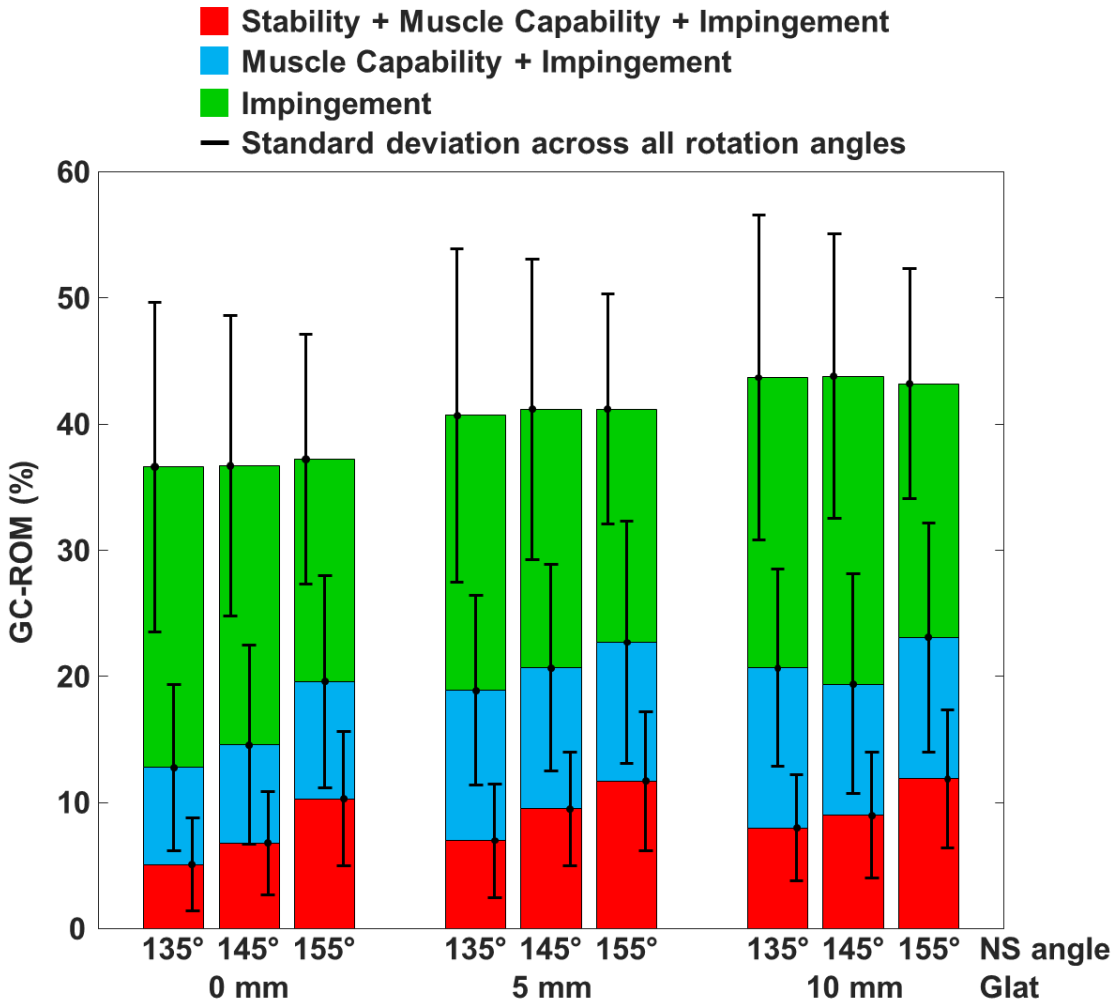

Figure 4.5. Average GC-ROM values and standard deviations across all rotation angles of the various implant configurations based on the successive addition of arm position feasibility criteria.

The effect of axial rotation angle within representative single-plane motions (abduction and flexion) is illustrated in Figure 4.6 for a representative implant configuration (GLat = 0 mm, NS angle = 155°), where arm positions are represented as boxes comprising a grid; infeasible positions are shaded based on which ROM criterion was the limiting factor. It should be noted that positions where impingement occurred were not evaluated for either of the other criteria, and positions where muscles were insufficient were not evaluated based on stability. For abduction and flexion, respectively, 71% and

45% of arm positions were feasible. Of the allowable positions, 45% and 53% fell between 30° of internal and external rotation for abduction and flexion, respectively.

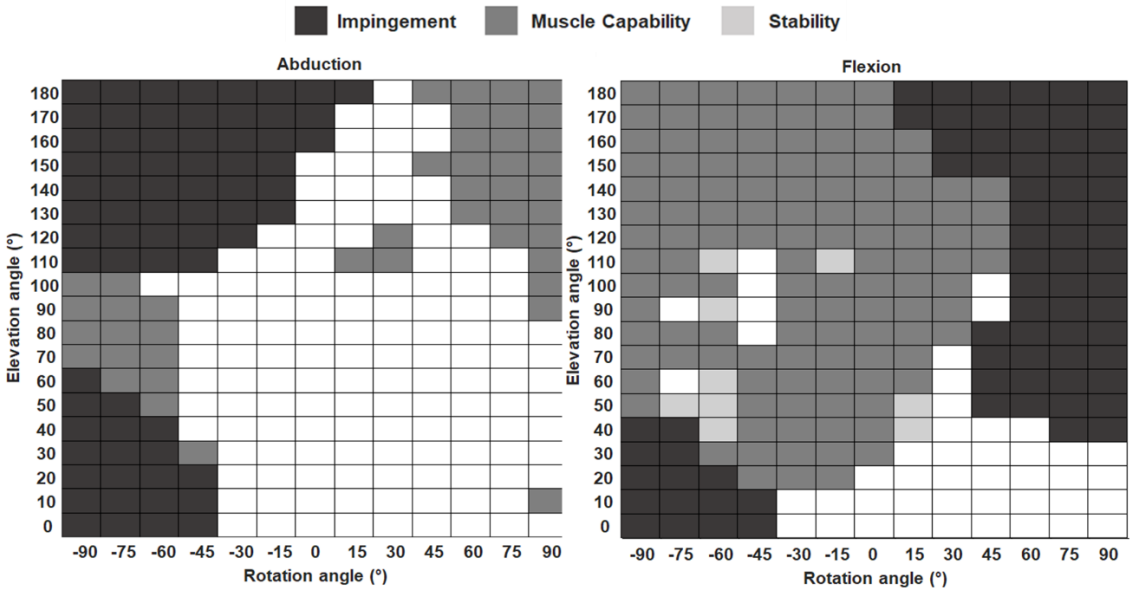

Figure 4.6. ROM in abduction (left) and flexion (right) at all rotation angles of the implant configuration having a GLat of zero mm and NS angle of 155° based on the different feasibility criteria. Negative rotation angles indicate external rotation. Note: any position where impingement occurred was not evaluated for any other criterion, and positions where muscles were incapable were not evaluated for stability.

4.3 Discussion

The concept of GC-ROM was developed to provide a single metric representative of post-operative implant performance encompassing passive and active factors that are considered within the comprehensive ROM of the joint. The basis of GC-ROM is similar to the "globe system" described by Doorenbosch et al.[23], where elevation plane angle and elevation angle are represented by spherical coordinates on a globe with its center corresponding to the COR of the shoulder; this is analogous to the convention adopted for joint angle descriptions in the Holzbaur et al.[24] musculoskeletal model. The concept has been adapted to represent GC-ROM, where there can be a different globe for each axial rotation angle, and allowable ROM at each axial rotation angle is represented by surface

regions on the globe representing feasible arm positions, the areas of which can be calculated for a quantitative description of ROM. Averaging the values for allowable ROM across all rotation angles thus provides a single metric characterizing shoulder mobility, which for the purposes of this research is determined specifically for investigating candidate rTSA designs, but is not limited to only this application. Previous studies related to ROM of rTSA generally characterize ranges of motions that are contained within single paths (i.e. abduction, flexion, axial rotation), where the most common metrics are the limits of the motions studied. However, conclusions pertaining to implant performance drawn from a subset of investigated motions may be misleading: trade-offs between increasing ranges of certain motions (abduction/adduction, and scaption), while decreasing ranges of others (flexion/extension and IE rotation) have been reported[32–37,40]. GC-ROM, which condenses the analysis of a broader range of motion, provides a single, generalized performance metric by which candidate rTSA designs are easily compared.

Considering impingement only, increasing lateralization increases GC-ROM (Figure 4.5), which is in agreement with previous studies that have reported increases in abduction/adduction, flexion/extension, and IE rotation ROM[32,33,35,36,38,69]. Although the impact of NS angle was much less than that of varying GLat, variable relationships between NS angle and GC-ROM appear to depend on the level of GLat. Configurations with NS angles of 155° were the best and worst performing designs at GLat levels of 0 mm and 10 mm, respectively, highlighting the importance of considering the combined effects of multiple implant parameters simultaneously throughout the comprehensive joint ROM. This is supported by Virani et al.[35], who showed that different implant designs maximized the impingement-free range of different motions.

Upon including muscle capability as a criterion along with impingement, the effect of varying GLat remains: increasing GLat increases GC-ROM (Figure 4.4). GLat did not appear to have a substantial effect on middle deltoid length or maximum possible force with the arm in neutral position (Table 4.1), where increasing Glat by 5 mm increased maximum possible force production by an average of only 9 N. Several studies have reported increases in JCFs with increasing GLat, which can be attributed to higher deltoid force production required to compensate for decreases in elevation muscle moment arms[69,70,76–78]. Together, these factors indicate that increases related to elevation are not likely a cause for the increases in GC-ROM.

Increasing GLat by 5 mm results in an average increase of 116 N in force capacity of the subscapularis due to muscle lengthening, which may increase GC-ROM due to effects on axial rotation capacity. Similar relationships between GLat and muscle length have been reported for the external rotators, the infraspinatus and teres minor[64,79,80], which could mean further increases in GC-ROM with increasing GLat, depending on the level of damage to these muscles. On the other hand, increasing NS angle, and therefore distalizing the humerus, could tension the deltoid in a manner that is advantageous in elevation. This may come at the cost of compromising IE rotation capacity of the rotator cuff muscles, which can be mitigated by increasing GLat (Table 4.1).

Adding stability into the calculation of GC-ROM decreased the effect of increasing GLat, especially at lower NS angles, and amplified that of increasing NS angle (Figure 4.5). Costantini et al.[69] reported an increase in JCFs with increasing GLat, manifesting mostly as higher compressive forces on the glenosphere, with some increase in shear as well. The decomposition of these JCFs into compressive and shear dislocation forces

between the humeral cup and glenosphere is dependent on NS angle. Langohr et al.[81] concluded that contact patterns on the articular surface of the humeral cup were shifted from centrally to inferomedially located with increasing NS angle during abduction. This is indicative of a higher compressive/shear ratio with higher NS angles, which is related to a more stable joint, a relationship that would be predicted by the analytical equation used to assess the stability criterion in the calculation of GC-ROM. GC-ROM evaluates stability in all planes of motion included, where some motions may result in a generally lower compressive/shear ratio due to the resultant directions of JCFs, which are also affected by IE rotation angle[37] (Figure 4.6) and implant design.

The increases in GC-ROM as a result of increasing both GLat and NS angle can be understood based on the biomechanical changes resulting from varying the implant design, and are consistent with previous studies that have reported similar trends for subsets of motions. Additionally, while GC-ROM is indicative of average implant performance across all rotation angles, standard deviations (Figure 4.5) may provide insight into which implants may perform well at some rotation angles, but poorly at others. The standard deviations calculated in this study are essentially a measure of circumduction ROM variability at different IE rotation angles. A given implant configuration likely has a larger ROM at 0° of rotation than at 90° of external rotation (Figure 4.6), and standard deviations (Figure 4.5) are indicative of the magnitude of that difference. Considering all three feasibility criteria, implant configurations with a 155° NS angle have lower standard deviations than those with 135° and 145° NS angles at the corresponding GLat level. This indicates that the configurations with a 155° NS angle may have higher GC-ROM values due to more consistent performance across all rotation angles. In the future, the technique

of evaluating GC-ROM could be adapted to emphasize ROM within ranges that activities of daily living most frequently occur to determine if the effects of implant design are similar to those observed in this study for the comprehensive ROM.

The limitations of this study are inherent to using computational modeling in the prediction of functional outcomes of rTSA. Firstly, due to the way in which motions of the shoulder were defined in the musculoskeletal and FE models with scapulothoracic motion based on humeral elevation, GC-ROM does not include an analysis of adduction from neutral arm position. Inferior impingement and scapular notching are known problems following rTSA[8,11,82–84]. However, the placement of the glenosphere in this study resulted in inferior overhang from the glenoid, which has been shown to decrease the occurrence of inferior impingement[16,32,36].

Another limitation is related to the method of determining muscle capability, which essentially seeks to distinguish potential physiologic muscle weakness from model weaknesses, which can result from modeling muscles as line-segment entities (a well-established challenge in musculoskeletal modeling). Although this criterion was not validated, the OpenSim user manual recommends a maximum of 10% joint torque contribution by reserve actuators, which was the maximum threshold for determining muscle sufficiency in this study. The effect of implant parameters on factors such as muscle length are consistent with previous studies. Additionally, the method of determining arm position feasibility based on muscle capability is consistent across all scenarios, allowing the elucidation of the effect of implant design.

Limitations in evaluation of stability relate to using an analytical equation to predict shear FTD. Although the FE model may provide a more accurate measure of shear FTD

(Figure 3.12), its computational inefficiency is outweighed by that fact that there are likely stabilizing contributions of other soft tissues, such as the ligaments and joint capsule which are not accounted for in the mathematical model and may lead to a more stable joint than predicted. As such, it is an acceptable method for determining joint stability in the context of comparing GC-ROM, and therefore implant performance, as the method is also consistent across all scenarios.

In conclusion, GC-ROM represents a metric that was developed to evaluate passive and active factors related to the ROM of rTSA within the comprehensive range of shoulder motion. It facilitates the comparison of variable implant configurations in terms of a functional outcome. It was shown using GC-ROM that increasing glenoid lateralization and neck-shaft angle both affect ROM to varying degrees, depending on the criteria included in the evaluation of arm position feasibility, and that trends between implant design variations and resulting ROM could be explained by the biomechanical changes they imparted. Although the potential applications of GC-ROM are numerous, for the purposes of this research it is considered only as a viable metric for implementation in design optimization to determine rTSA configurations that maximize post-operative functional ROM.

Chapter 5. Maximizing Overall ROM vs. ROM for ADL

Chapters 3 and 4 focused on the development, validation, and implementation of computational methods and a metric, GC-ROM, to assess ROM of any given rTSA implant configuration. Chapter 5 continues the natural progression toward the end goal of MOO considering ROM and joint stability by leveraging GC-ROM in single-objective optimization to maximize overall ROM, as well as envelopes of motion within which ADL are most frequently performed. The following sections discuss methodologies related to: the general formulation of the optimization problem, the selection and parameterization of design variables, the use of surrogate modeling for objective function evaluation, and the modification of the objective function to optimize for different envelopes of motion. Finally, the designs that maximize the various ROM envelopes studied are presented and discussed.

5.1 Methods

5.1.1 Optimization Problem Formulation

The optimization problem was formulated as follows:

$$\text{Minimize: } J(\boldsymbol{x}) = -J_{GC-ROM}(\boldsymbol{x}) \qquad \text{Eq. (5.1)}$$

$$\text{Subject to: } \boldsymbol{x}_{min} \leq \boldsymbol{x} \leq \boldsymbol{x}_{max} \qquad \text{Eq. (5.2)}$$

where $\boldsymbol{x}$ is a vector of selected implant and surgical parameters and $\boldsymbol{x}_{max}$ and $\boldsymbol{x}_{min}$ are vectors representing the upper and lower bounds of the design variables, respectively. Optimization was performed using the Optimization Toolbox in MATLAB, as was done by Willing and Kim[85] to optimize knee implant kinematics, where the Sequential quadratic programming (SQP) algorithm was used in conjunction with *fmincon*, which finds the minimum of constrained, nonlinear, multivariate functions. GC-ROM was determined based on IE rotation angles of -90°, 0°, and 90°. The only rotator cuff muscle modeled was the subscapularis. The upper and lower bounds of the design parameters were determined such that the implant configurations generated by the optimization algorithm were physically realistic (i.e. a glenosphere that doesn't contact the glenoid is not realistic). Additionally, the entire process of calculating GC-ROM was automated.

5.1.2 Selection and Parameterization of Design Variables

Four variables were chosen: GLat, NS angle, inferior offset of the glenosphere (COR_{inf}), and humeral lateralization (HLat), which are shown in Figure 5.1. Together, they represent of range of both design and surgical placement parameters. It should be noted that humeral lateralization was not introduced in Chapter 2, as its effects on functional outcomes are relatively less understood in comparison to the other design parameters.

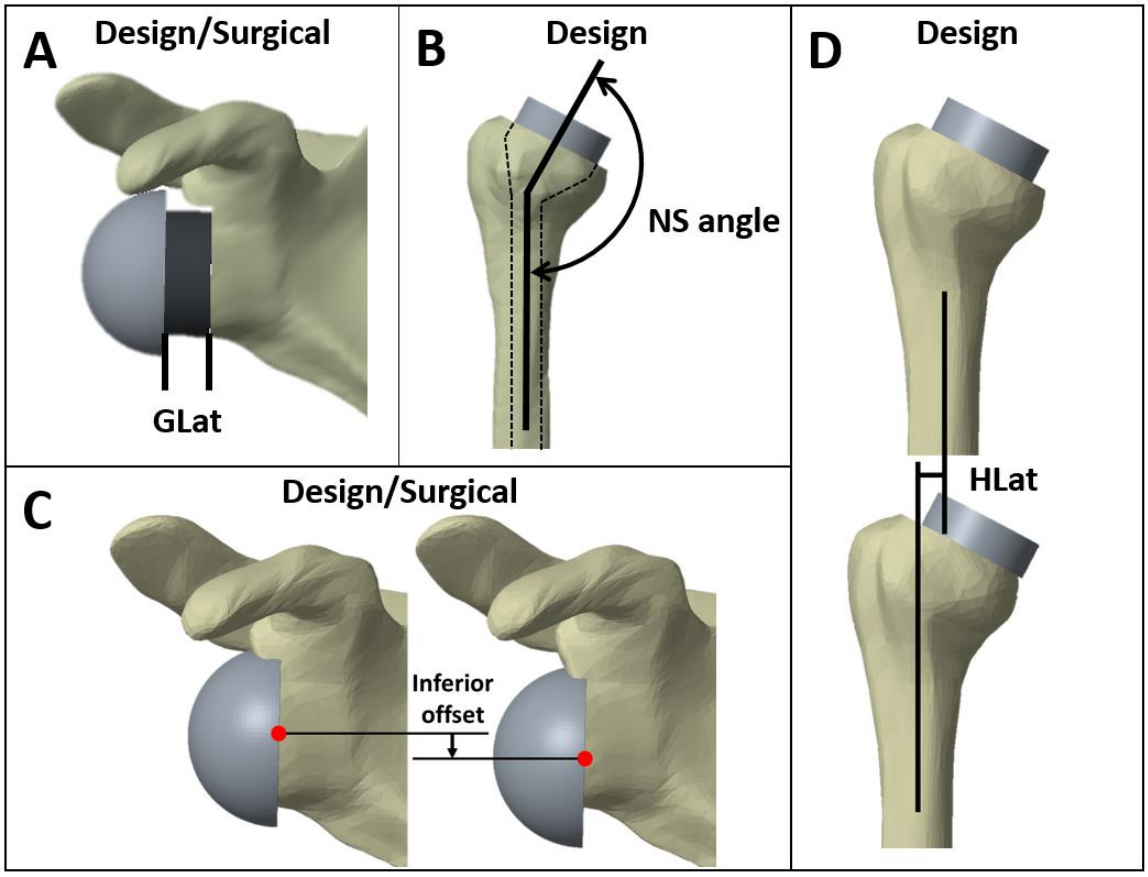

Figure 5.1. The four design variables included in design optimization were A) glenoid lateralization (GLat), B) neck-shaft (NS) angle, C) inferior offset of the glenosphere (COR_{inf}), and D) humeral lateralization (HLat). The classification of each variable in terms of implant design or surgical placement is shown.

For all implant configurations, a hemispherical glenosphere with a diameter of 36 mm was used in conjunction with a humeral cup depth of 6 mm. The following subsections outline the parameterization of the variables chosen for incorporation into the optimization problem.

5.1.2.a Scapular Variables

The parameterization of GLat and COR_{inf} were both dependent on a baseline COR. The baseline COR was determined by manually fitting a 25 mm diameter circle, representing the diameter of a baseplate, to the inferior rim of the anatomic glenoid in a plane defined by points on the anterior and posterior rims and reaming perpendicularly

toward the glenoid to the minimum depth creating a flat surface (Figure 5.2). The center of the circle projected onto this surface served as the baseline COR.

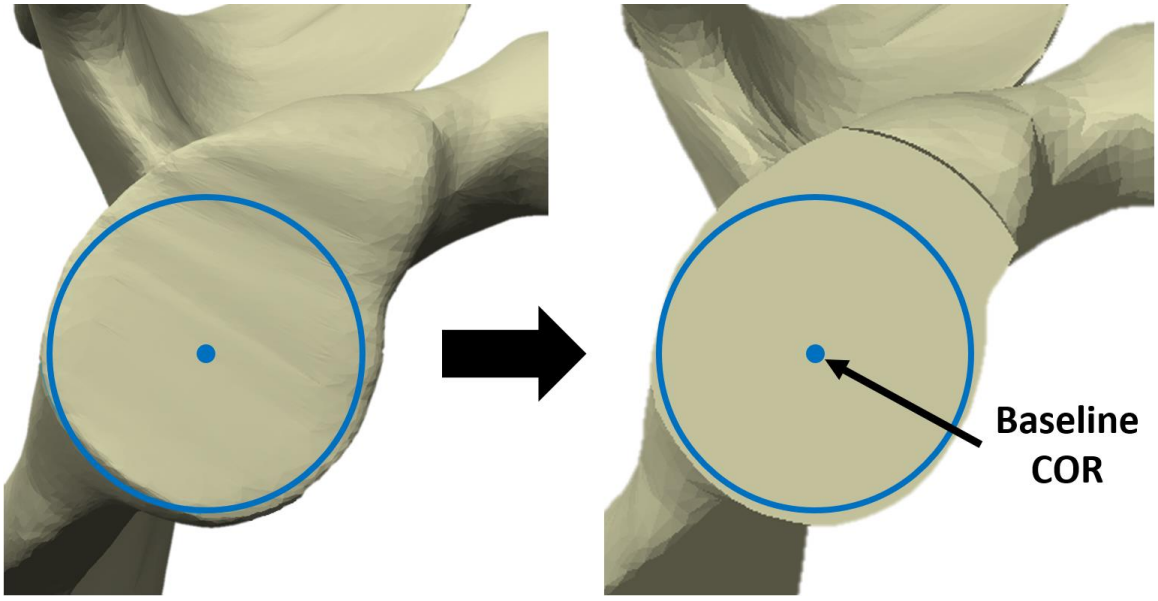

Figure 5.2. The process by which the baseline COR was determined where a 25 mm diameter circle was fit to the inferior rim of the glenoid, after which the glenoid was virtually reamed to achieve a flat surface.

Values of 0 mm for both GLat and COR_{inf} result in a typical grammont-style rTSA configuration with no COR lateralization and inferior overhang. GLat was accomplished with spacers, as demonstrated previously in Chapter 4 (Figure 4.4). It should be noted that surgically, GLat may be measured from the anatomic glenoid, however, the convention for selecting the point from which to measure varies from surgeon to surgeon. To eliminate ambiguity, GLat was measured from the reamed surface and corresponded directly to spacer thickness. The lower and upper limits of GLat were selected as 4.8 mm and 16 mm, respectively (Figure 5.3). This was based on the assumption that at least some level of GLat would be beneficial, which has been concluded by numerous previous studies[16,29,32,39,70,79,80,86–88].

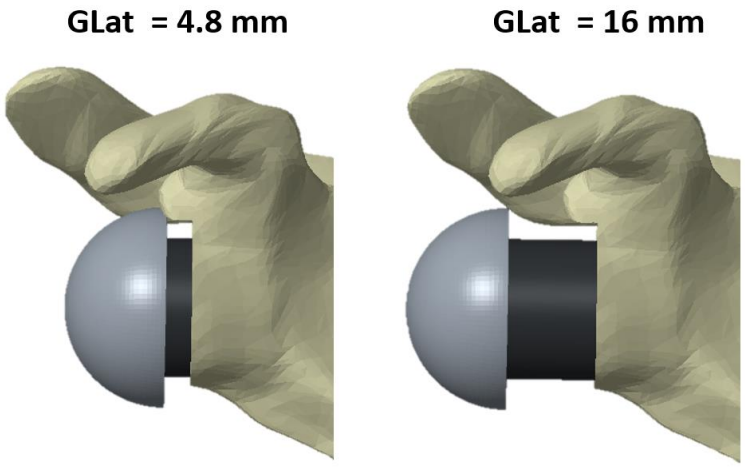

Figure 5.3. The upper and lower bounds of GLat were 4.8 mm (left) and 16 mm (right), respectively.

Inferior (or superior) offset of the glenosphere (COR_{inf}) was also measured from the baseline COR in a direction defined by connecting the centers of 25 mm and 29 mm circles fit to the anatomic inferior rim. The 25 mm circle was the same used in the definition of the baseline COR, and 29 mm is another common baseplate size. With this method, the direction in which the glenosphere was offset was based on glenoid anatomy, rather than traditional anatomic directions (Figure 5.4). The upper and lower limits for COR_{inf} were 4 and -4 mm, respectively (Figure 5.5), such that fixation to the glenoid would still be feasible.

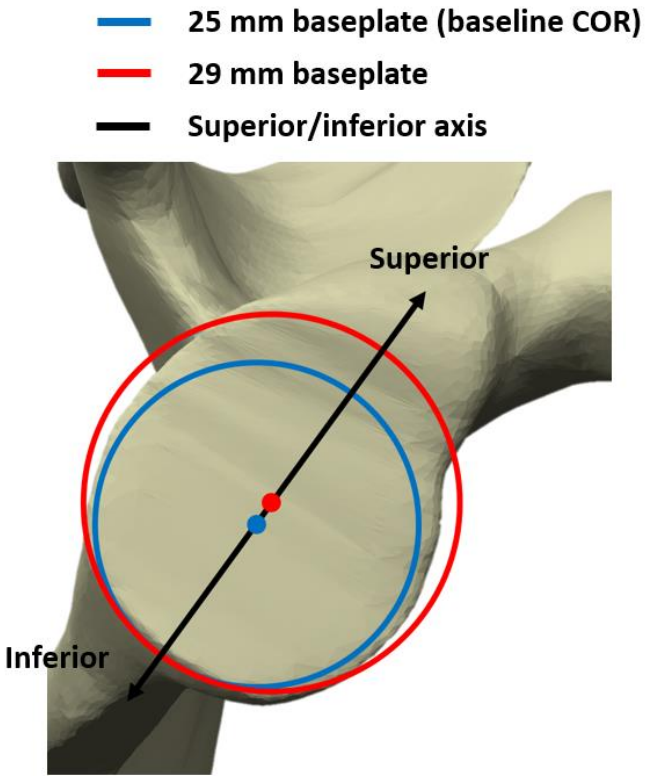

Figure 5.4. The method of defining the direction in which the glenosphere was translated to accomplish superior/inferior offset as advised by an orthopaedic shoulder surgeon.

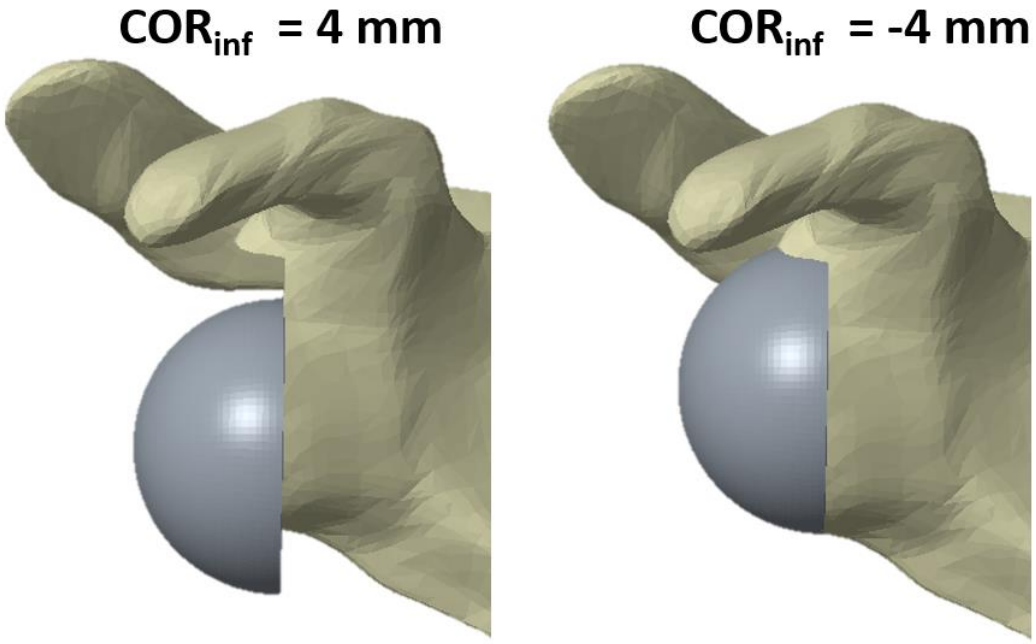

Figure 5.5. The upper and lower bounds for inferior offset of the COR were 4 mm (left) and -4 mm (right).

5.1.2.b Humeral Variables

NS angle was measured from the long axis of the humerus, which was taken as being perpendicular to ground with the arm at neutral elevation (as defined in the Holzbaur et al. musculoskeletal model). The version of the humeral component matched that of the glenoid component in magnitude, but was in the opposite direction (i.e. the glenoid component was anteverted and the humeral retroverted, as measured from anatomic planes with the arm in neutral position). The baseline ream depth for a given NS angle was determined by the inflection point at the junction between the humeral head and the greater tuberosity, as directed by an orthopaedic shoulder surgeon. The baseline position of the humeral cup was determined by centering it with a circle fit to the outer edge of the ream. The upper and lower limits of NS angle were selected as 130° and 170°, respectively, which in greater than the range of commercially available implants.

Using a traditional Grammont-style onlay humeral cup (that which has been depicted thus far), the humerus could be lateralized along the direction dictated by NS angle. This would also involve distalizing the humerus and would affect muscle lengths, moment arms, and torque generation[89]. Since the same factors are affected by NS angle (Table 4.1), a method of lateralizing the humerus was adopted to eliminate as much interdependence of the variables as possible. The ream depth itself was adjusted to lateralize the humerus without affecting the superior/inferior offset of the humerus at neutral arm position. Measured from the baseline position of the humerus for a given NS angle, the upper and lower limits of HLat were selected as 3 and -3 mm, respectively, illustrated in Figure 5.6. For clarity, HLat is a measure of humeral translation. Positive

values indicate humerus lateralization (medialization of humeral cup on the ream) and negative values indicate humerus medialization (lateralization of humeral cup on the ream).

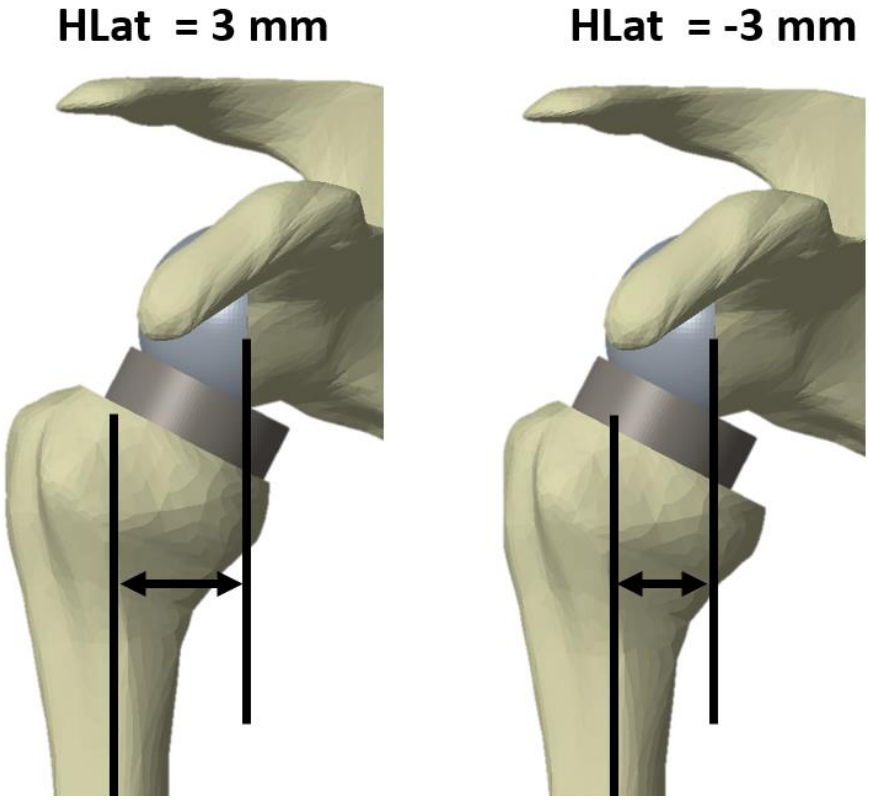

Figure 5.6. The upper and lower bounds for HLat were 3 mm (left) and -3 mm (right), which was accomplished by adjusting the ream depth to account for the corresponding lateralization of the humerus. Recall increasing HLat moves the humerus away from the scapula, while decreasing moves it toward.

5.1.3 Calculation of the Objective Function Using Surrogate Models

5.1.3.a Surrogate Model Fitting for GC-ROM

After selecting and parameterizing implant design variables for the optimization problem and the entire computational pipeline to calculate GC-ROM was automated, the calculation of GC-ROM using an Intel® Core™ i7-4790 @ 3.60 GHz processor took over two and a half hours for any given implant configuration. Due to the unpredictable nature of optimization in terms of the number of required function evaluations, computational efficiency was of high concern. For this reason, the RSM, outlined in section 2.5.1, was

used to generate analytical, quadratic representations of GC-ROM including all terms (linear, perfect-square, and interaction) for use in optimization. The sample points for fitting the surrogate model(s) were based on 3^4 full factorial design. The full computational pipeline was used to evaluate every rTSA design resulting from selecting one of three prescribed values (levels) for each of the four design variables, for total of 81 sample points. The levels for NS angle, COR_{inf}, and HLat were selected based on the upper and lower bounds prescribed as part of the optimization problem formulation, as well as the midpoint (NS angle = 130°, 150°, 170°; COR_{inf} = -4 mm, 0 mm, 4 mm; HLat = 3 mm, 0 mm, -3 mm). GLat levels were selected as 4.8, 9.6, and 16 mm. Each variable was normalized to have values of -1, 0, and 1. Normalized variables and corresponding objective function values (GC-ROM) of each design were used in conjunction with the least squares method to solve for the coefficients of quadratic equation given by Eq. 2.5 in MATLAB, resulting in an analytical representation of GC-ROM.

5.1.3.b GC-ROM Surrogate Model Assessment

The efficacy of the surrogate model in predicting optimal rTSA designs was assessed in multiple ways. A surrogate model was fit to the GC-ROM values for a subset of sample points, namely the nine implant configurations generated by combinations of all three levels of GLat and NS angle with COR_{inf} and HLat both equal to zero. The surface representation of the surrogate model was plotted in conjunction with design parameters and objective function values for the optimal design(s), as well as the sample points used for model fitting. This was to ensure that surrogate modeling is a suitable method in conjunction with numerical methods for determining optimum designs as they relate to maximizing outcomes of rTSA.

Additionally, the average absolute and root-mean-square (RMS) errors between surrogate model predictions and full model predictions were calculated when using all 81 sample points to generate the response surface. Similarly, errors between surrogate and full model predictions were calculated for a group of 15 random test designs. More importantly for application in optimization, the trends in GC-ROM predicted by the surrogate model as a result of variations in rTSA design were evaluated using Pearson correlation coefficient values.

5.1.4 Optimizing Overall ROM vs ROM for Activities of Daily Living

GC-ROM represents the general, overall ROM, which includes IE rotation angle from 90° external to 90° internal, and elevation plane angles from -90° to 120°. The rTSA design which maximizes this may differ from one that maximizes motions that are performed more frequently in ADL. Therefore, the calculation of GC-ROM was modified to include varying envelopes within the comprehensive ROM and optimization was repeated to investigate the relationships between optimum design and type(s) of motion maximized. The different motion envelopes included combinations of negative and positive IE rotation and elevation plane angles, for a total of nine (Table 5.1). For example, calculating GC-ROM including only IE rotation and elevation plane angles greater than or equal to zero would result in an optimized design that maximizes forward/side reaching motions.

Table 5.1. The different motion envelopes that were maximized included various combinations of negative and positive IE rotation and elevation plane angles.

IE rotation angle (γ)	*ElvP angle (α)*
$-90° \leq \gamma \leq 90°$	$-90° \leq \alpha \leq 120°$
	$\alpha \geq 0°$
	$\alpha \leq 0°$
$\gamma \geq 0°$	$-90° \leq \alpha \leq 120°$
	$\alpha \geq 0°$
	$\alpha \leq 0°$
$\gamma \leq 0°$	$-90° \leq a \leq 120°$
	$\alpha \geq 0°$
	$\alpha \leq 0°$

In order to maximize different envelopes of motion, the calculation of GC-ROM was discretized by positive and negative IE rotation and elevation plane angles (Figure 5.7) for each sample point, and surrogate models were fit to each of the six sub-portions of the ROM. In this manner, the linear sum of the predictions of each surrogate model is equal to GC-ROM. Using this method, different motion envelopes were maximized by selecting different combinations of surrogate models used in the calculation of the objective function (Table 5.1).

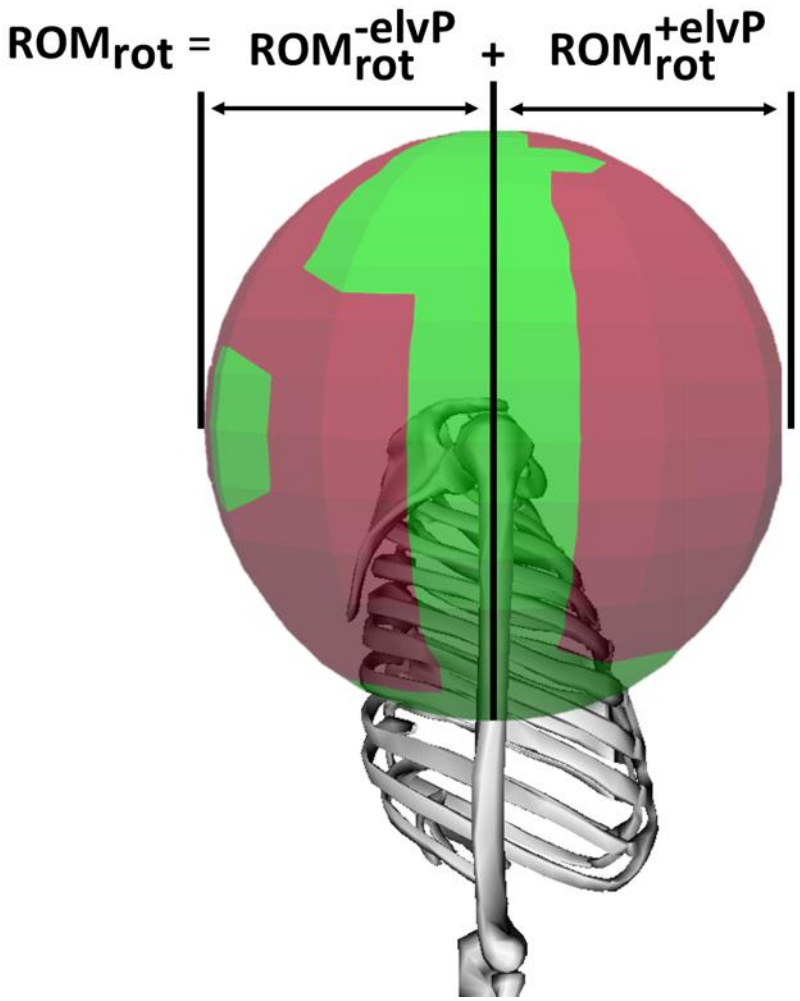

Figure 5.7. The calculation of overall ROM (GC-ROM) can be discretized by both rotation angle, each represented by a different sphere, and ± elevation plane angles. In this manner variable portions of the ROM can be optimized based on the selection of which portions are included in the objective function calculation.

For every motion envelope, optimization was performed using 100 random start points to increase the likelihood of finding the global optimum. Resulting optimum designs were compared by quantifying sacrifices in alternate portions of the ROM (those not included in the respective objective function).

5.2 Results

5.2.1 Surrogate Model Assessment

The response surface generated based on varying a subset of design variables (GLat and NS angle) is shown in Figure 5.8. The equation for the response surface was employed as the objective function in optimization. The resulting optimum designs correspond to the local (pink dot) and global (green square) maxima within the design variable intervals. The design that produced the global maximum had a GLat of 16 mm and a NS angle of 145.4°.

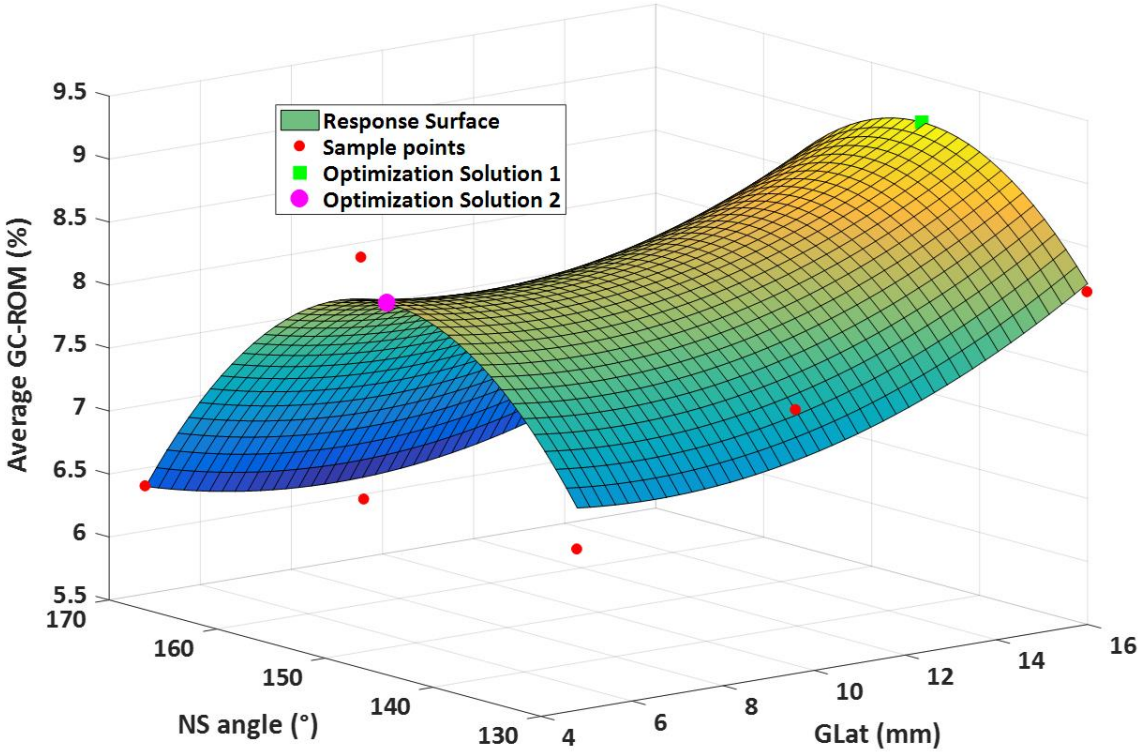

Figure 5.8. A plot showing a response surface fit to a set of nine sample points (3 GLat levels X 3 NS angles) and the optimal designs resulting from its implementation in optimization. Optimization solutions 1 and 2 are global and local maxima, respectively.

Full model versus surrogate model predictions of GC-ROM for the full set of 81 samples points are shown in Figure 5.9. The Pearson coefficient, or correlation, between the two prediction methods was 0.95 ($p < 0.001$). Error in the magnitude of predictions between the two models was quantified. Considering the sample points only, the mean

absolute and RMS errors were 0.4% and 0.7%, respectively, between the full and surrogate models. Similarly, in predicting GC-ROM of 15 sample points that were not used to train the model, absolute mean and RMS were 0.8% and 0.6%, respectively.

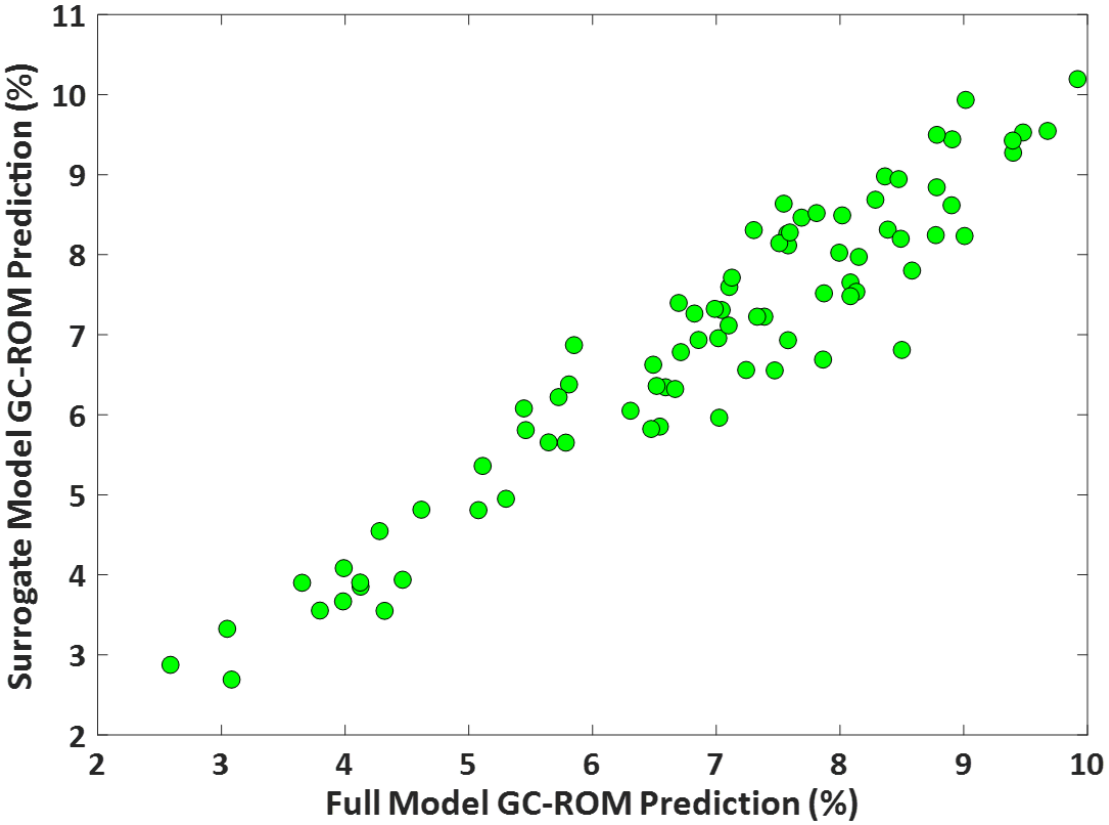

Figure 5.9. A plot showing the GC-ROM predictions of the full and surrogate models for the 81 sample points used to fit the response surface.

5.2.2 Optimum rTSA designs for overall ROM vs ROM for ADL

Table 5.2 shows the designs that optimized different portions of the ROM.

Table 5.2 Optimal rTSA designs that maximize the overall ROM, as well as various motion envelopes within. Upper and lower bounds for each design variable were: 4.8 mm ≤ GLat ≤ 16 mm; 130° ≤ NS angle ≤ 170 °; -4 mm ≤ COR_{inf} ≤ 4 mm; -3 mm ≤ HLat ≤ 3 mm.

ROM Envelope Maximized		**Optimum Design**			
IE rotation angle (γ)	***ElvP angle (α)***	***GLat (mm)***	***NS angle (°)***	***COR_{inf} (mm)***	***HLat (mm)***
-90° ≤ γ ≤ 90°	-90° ≤ α ≤ 120°	4.8	154.4	4	-3
	α ≥ 0°	11.3	170	4	-3
	α ≤ 0°	4.8	145.4	4	-1
γ ≥ 0°	-90° ≤ α ≤ 120°	4.8	154.6	4	-3
	α ≥ 0°	10.1	170	4	-3
	α ≤ 0°	4.8	146.6	4	-1.4
γ ≤ 0°	-90° ≤ *α* ≤ 120°	4.8	170	4	-3
	α ≥ 0°	16	170	4	-3
	α ≤ 0°	6.2	148.5	4	-0.9

In the case of maximizing variable envelopes within the overall ROM, the motions most commonly involved in ADL are those in the forward elevation planes, according to a study by Langhor et al.[90], who reported that over 80% of time was spent in elevation planes with angles greater than -30° for patients with rTSA. As such, the two designs that optimized overall ROM and ROM in forward elevation planes (Figure 5.10), including all IE rotation angles, were compared for performance in all other motion envelopes studied. Additionally, they were analyzed with the full computational pipeline to ensure accuracy of the conclusions drawn using the surrogate models. The results are shown in Table 5.3.

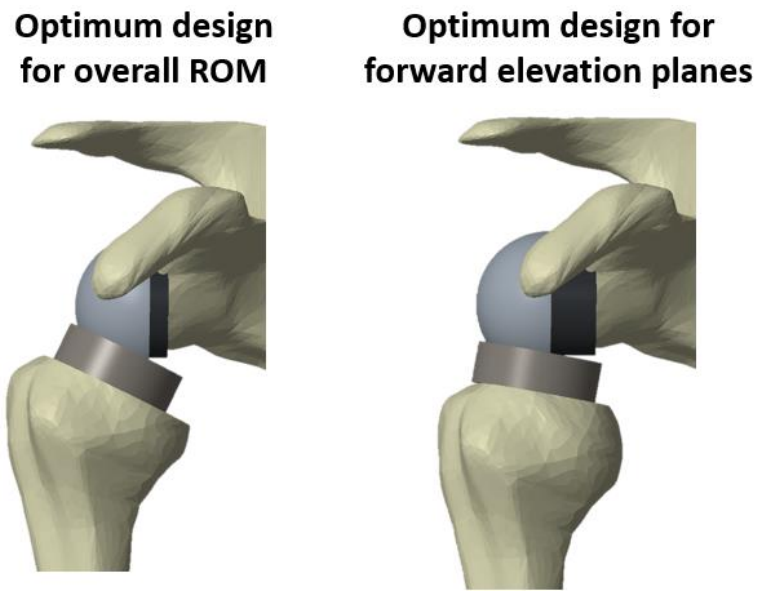

Figure 5.10. The design that maximized overall ROM, including all elevation planes (left), versus that which maximized motion in forward elevation planes (right).

Table 5.3. A comparison of the performance of designs maximizing overall ROM and ROM for ADL in the context of other motion envelopes. Note: performance metrics are presented as the raw sum of the percent surface area covered by the feasible ROM on each corresponding sphere (IE rotation angle). This is in opposition to averaging the percent surface area across all spheres, but allows for a more direct comparison of values in the context of variable elevation plane angles included in the calculation.

ElvP angles (α) optimized for	**Optimum Design**				**Optimum Design Performance: Surrogate model**			**Optimum Design Performance: Full model**		
	GLat (mm)	*NS angle (°)*	*COR_{inf} (mm)*	*HLat (mm)*	*ElvP angles analyzed:*					
					$-90° \le \alpha \le 120°$	*$\alpha \ge 0°$*	*$\alpha \le 0°$*	*$-90° \le \alpha \le 120°$*	*$\alpha \ge 0°$*	*$\alpha \le 0°$*
$-90° \le \alpha \le 120°$	4.8	154.4	4	-3	29.9%	17.6%	12.3%	28.3%	15.1%	13.2%
$\alpha \ge 0°$	11.3	170	4	-3	26.6%	19.1%	7.5%	27.4%	19.9%	7.5%

5.3 Discussion

5.3.1 Surrogate Model Assessment

Although, the results from Figure 4.5 indicate that designs with NS angles of 155° should perform better than the optimum design resulting from employing a surrogate model, clear conclusions can still be drawn. In other words, surrogate models may sacrifice absolute accuracy of optimum designs, but their use is justified in terms of analyzing

trends. It is clear from Figure 5.8 that the extreme values of NS angle will not optimize the ROM; the same conclusion would be drawn without the aid of a visual representation. Additionally, the computational efficiency of surrogate modeling allows for comprehensive searches of the design space in terms of starting points for the optimization algorithm, thereby increasing the chance of finding the global minimum within the design variable limits.

Pearson coefficient values close to 1 exemplify very strong positive relationships between data sets. In this context, a strong positive correlation is exemplary of the efficacy of the surrogate model in predicting changes in GC-ROM as a result of variable rTSA design configurations. A very low p-value rejects the null hypothesis that there is no correlation between the two data sets (prediction methods), i.e. there is statistically significant correlation. This supports that surrogate modeling is capable of being used in conjunction with numerical methods to find optimum designs of rTSA because it 1) captures trends in GC-ROM due to changes in implant design and 2) shows acceptable agreement in predicting magnitudes of the objective function.

5.3.2 Optimum rTSA Designs for Variable Motion Envelopes

Among all optimum designs for all motion envelopes maximized, there is universal agreement that maximizing inferior placement of the COR is beneficial. Increasing COR_{inf} increases impingement-free ROM[16,33,36] and may be advantageous in tensioning the deltoid for improved torque-generating capabilities.

Lower levels of GLat and mid-range values for NS angle generally maximize ROM regardless of which IE rotation angles are included when 1) all elevation plane angles are included and 2) only negative elevation plane angles are included in the objective function

calculation. This follows Grammont's original idea that medializing the COR of the joint to increase deltoid moment arms and using non-anatomic NS angles/inferiorly offsetting the COR to tension deltoid fibers allows rTSA to restore ROM to the joint[8]. It is interesting to note that the results appear contradictory to those presented in Figure 4.5, where increasing GLat increased ROM. This highlights the importance of considering the effects of multiple design parameters simultaneously, as their combined effects may differ than those of varying each individually.

Maximizing motions within the forward elevation planes tends to require increasing GLat. This is likely a result of modeling the subscapularis as the only functioning rotator cuff muscle: it contributes mainly to internal rotation, but the superior portion can act as an elevator in forward planes as well, especially at higher elevation angles[91]. Since increasing GLat decreases moment arms of the deltoid, and increases necessary force production[69,70,77,78,86], functioning rotator cuff muscles may aid the deltoid in elevation motions in corresponding planes. For example, the subscapularis may aid deltoid with elevation in forward planes. However, in order to do so they must be sufficiently tensioned, which can potentially be accomplished by increasing GLat[79] (Table 4.1). Additionally, the higher levels of GLat are always in combination with higher NS angles, which tension the deltoid and increase possible force production (Table 4.1).

Particularly interesting observations are related to the implant parameter involving lateralization of the humerus. All optimum designs involve shifting the humerus medially (i.e. decreasing HLat). Previous studies have concluded that increasing HLat increases deltoid moment arms, which decreases required deltoid force and JCFs[39,70,91–93], which should effectively improve ROM. However, a medially offset humerus, which places the

cup on the superolateral portion of the humeral ream, may improve impingement-free ranges of elevation by avoiding contact between the greater tuberosity on the humerus and the inferior acromion.

5.3.3 Optimum rTSA Designs for Overall ROM versus ROM for ADL

While design optimization may not necessarily afford the elucidation of individual cause-effect relationships related to varying design parameters, the benefit lies in the ability to determine the optimum *combination* of design variable values. In the case of maximizing variable envelopes within the overall ROM, the motions most commonly involved in ADL are those in the forward elevation planes. This is according to a study by Langhor et al.[90], who reported that over 80% of time was spent in elevation planes with angles greater than -30° for patients with rTSA. The design that maximizes overall ROM versus that which maximizes forward elevation motions (considering all IE rotation angles) differ in terms of GLat and NS angle (Figure 5.4), which begs the question, which design is the "best"? The answer is highly subjective based on a range of factors, but quantifying the relative sacrifices of a design within portions of the ROM other than that which was maximized may provide some insight.

As hypothesized, maximizing the ranges of motions within the forward elevation planes comes at the cost of a sacrifice in terms of the backward elevation planes, which correlates to worse "overall" performance of the design to maximize ROM for ADL. Analogous conclusions can be drawn from the data generated using both the surrogate and full models. Optimizing for overall ROM requires less of a sacrifice in forward elevation planes as compared to the sacrifice in backward elevation planes necessary to maximize ROM for ADL (forward planes). However, the clinical significance of these relative

sacrifices is unknown and it is possible that the "optimal" design could be chosen based on factors that are not considered as functional outcomes within the calculation of ROM. For example, increasing GLat results in increased torque and micromotion at the bone-implant interface[94–96], a topic which we have recently studied and published results for[94]. In the case of increased micromotion, fixation and long-term survivorship of the implant are a concern. Therefore, increasing the likelihood of implant survivorship may outweigh the gains in ROM for ADL afforded by lateralized designs. These are the types of relationships that should be considered in choosing rTSA configurations that maximize ROM (i.e. if stability is not a concern).

Chapter 6. Multi-objective Design Optimization of rTSA

The final objective of this research was to quantify trade-offs between competing functional outcomes of rTSA, namely ROM and stability. Thus far, stability has been considered as a ROM limiting criterion; for any given arm position to be considered feasible, JCFs resulting from muscle action alone could not dislocate the joint. In this manner, stability was essentially a constraint built into the assessment of the objective function used to maximize ROM. Stability should also be considered in the context of the efficacy of implant designs in resisting dislocation when subjected to additional JCFs, which could result from interaction with the environment. For example, additional shear forces on the joint could result from lifting an object from the ground. This type of *functional stability* should be maximized, but may come at the cost of sacrificing ROM, the trade-offs between which are characterized by the Pareto front resulting from MOO. The following sections will discuss the objective function used to characterize stability, formulate the general problem for MOO, and finally MOO results will be presented and discussed.

6.1 Methods

6.1.1 Development of an Objective Function to Characterize Stability of rTSA

As previously mentioned, the stability of rTSA in the context of potentially increased JCFs, relative to those resulting from muscle action alone, should be maximized. Along those lines, at any given arm position, the worst-case scenario in terms of potential joint instability would be the addition of a pure shear force in the same direction as the shear component of the JCF resulting from muscle action. Elucidating an average measure of additional shear force required to dislocate the joint within the ROM is inherently coupled with the size of the feasible ROM envelope, which is not ideal for optimization objective functions. The measure of stability for a given implant configuration was characterized by the percentage of its ROM that was lost when an additional shear force was included in the calculation of the ROM. Feasible positions within the ROM were reevaluated and subsequently eliminated if the shear JCF plus an additional shear force (the magnitude of which will be discussed next), was greater than the shear FTD calculated using Eq. 3.1. GC-ROM was then recalculated and percent difference with respect to the original value (not including the extra shear force) represented a metric for stability that was uncoupled from the objective representing ROM. A response surface was fit in order to predict the value of the stability objective function for any given design in the same manner as described for the ROM objective in Chapter 5.

The magnitude of extra shear force (F_{shear}) was chosen to be 100 N. This was based on the results of a sensitivity analysis relating the percent ROM lost as a function of extra shear force magnitude for randomly selected designs within the set of 81 sample points used to train the surrogate model (Figure 6.1).

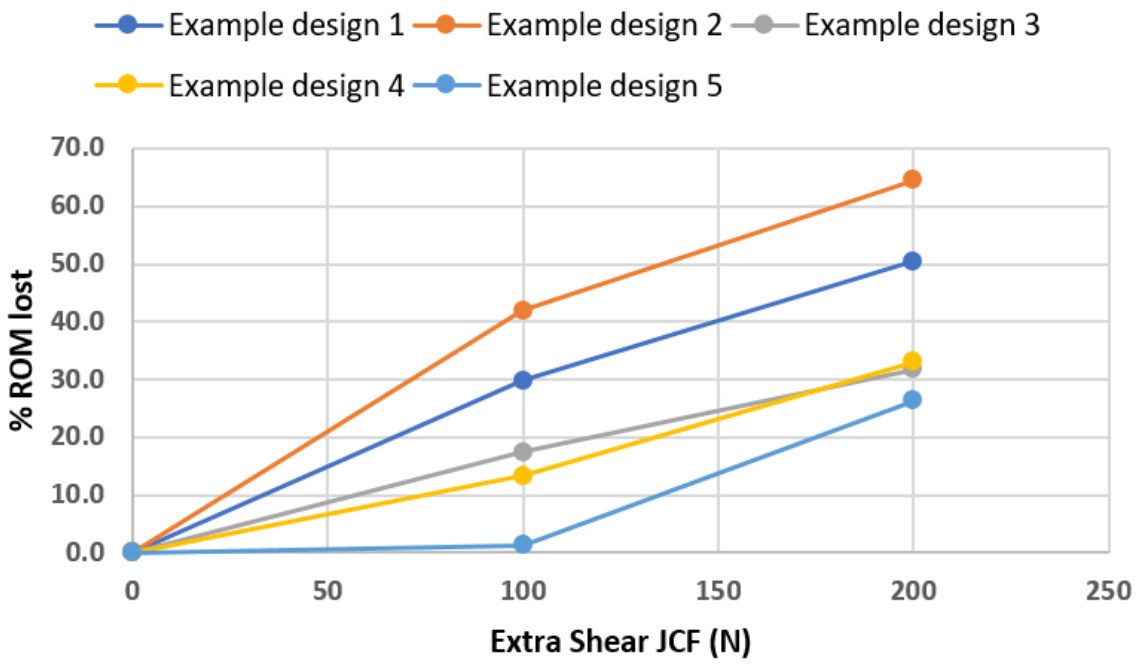

Figure 6.1. The percent ROM lost as a function of increasing additional shear JCF for randomly selected designs within the 81 surrogate model training points. Each line represents results for a different rTSA configuration.

The goal was to choose the magnitude of F_{shear} such that differences in the ROM lost as a result were distinguishable among variable implant designs. Too high of an additional shear force would cause all implant designs to lose 100% ROM, while a magnitude too low would suffer from the opposite. A F_{shear} of 100 was chosen; Figure 6.1 shows that at this level of additional shear force, even five random designs display variation in terms of the stability metric (% ROM lost). In this regard, maximizing stability would equate to minimizing the metric in MOO.

6.1.2 Optimization Problem Formulation

Any bi-objective MOO problem can be formulated as a single objective optimization problem by using the weighted sum technique. The general formulation for MOO considering ROM and stability is as follows:

$$\text{Minimize: } J(\boldsymbol{x},\ w) = w * -J_{ROM}(\boldsymbol{x}) + \ (1-w) * J_{Stab}(\boldsymbol{x}) \qquad \text{Eq. (6.1)}$$

$$\text{Subject to: } \boldsymbol{x}_{min} \ \leq \boldsymbol{x} \ \leq \ \boldsymbol{x}_{max} \qquad \text{Eq. (6.2)}$$

where J_{ROM} and J_{Stab} characterize the performance of a given design, $\boldsymbol{x}$. The design variables, their respective parameterizations, as well as upper and lower bounds ($\boldsymbol{x}_{min}$ & $\boldsymbol{x}_{max}$) remained consistent with the previous chapter. J_{ROM} was calculated for any given implant configuration as described in Chapters 4 and 5 using all IE rotation and elevation plane angles (i.e. generalized, overall ROM was considered in MOO).

By performing optimization with variable values of the weighting factor (*w*), which is indicative of the relative "importance" of each objective, the trade-offs between the two objectives was characterized using a Pareto front. When *w* is equal to zero, the resulting optimum design maximizes stability without considering ROM. Similarly, when *w* is equal to one, the resulting optimum design maximizes ROM without regard for stability. These two designs represent the anchor points on the Pareto front and were used to scale each function output between zero and one, such that neither dominated the calculation of Eq. 6.1. Points between the anchor points were characterized by the performance of optimum designs resulting from varying the value of *w* between zero and one by increments of 0.05. At each level of weighting factor, the algorithm was initialized using 100 random designs as start points, increasing the likelihood of arriving at Pareto optimal designs (i.e. finding global optimums along the design variable intervals).

6.2 MOO Results and Discussion

Figure 6.2 shows the Pareto curve resulting from MOO considering ROM and stability. Since the goal is to maximize the ROM metric and minimize the stability metric, the ROM objective was plotted to represent sacrificing ROM moving from left to right along the x-axis. This resulted in a more typical Pareto curve that would be representative

of minimizing both objectives. The utopia point, at which both functional outcomes could be simultaneously maximized (virtually unachievable if the objective functions are competing), would be at the origin. Dominated designs, those that can be improved in terms of at least one objective without detriment to the other, have performances above or to the right of the Pareto front.

As was hypothesized, the depicted Pareto front represents a clear trade-off between maximizing either ROM or stability. It is worth investigating which designs resulted in some of the key points along the front (Figure 6.2). The designs maximizing ROM without regard for stability, and vice versa, are at opposite ends of the spectrum in terms of both GLat and COR_{inf}. Both minimize HLat and have NS angles in the upper half of the range. To maximize stability or ROM separately, the values of GLat and NS angle should be increased (maximizes stability) or decreased (maximizes ROM) simultaneously. Moving from maximizing stability to maximizing ROM involves moving the glenosphere from a superiorly to inferiorly located position; all except one of the non-dominated points on the Pareto front with stability objective function values below 10 (i.e. less than 10% of the ROM is sacrificed with the addition of extra shear force) maximized superior placement of the glenosphere. Similarly, all but one point with ROM objective function values above 8% maximized inferior placement of the glenosphere. This could be a result of the fact that unstable positions are not part of the ROM to begin with when a superiorly place glenosphere is used, and are consequently not lost when additional shear JCFs are considered.

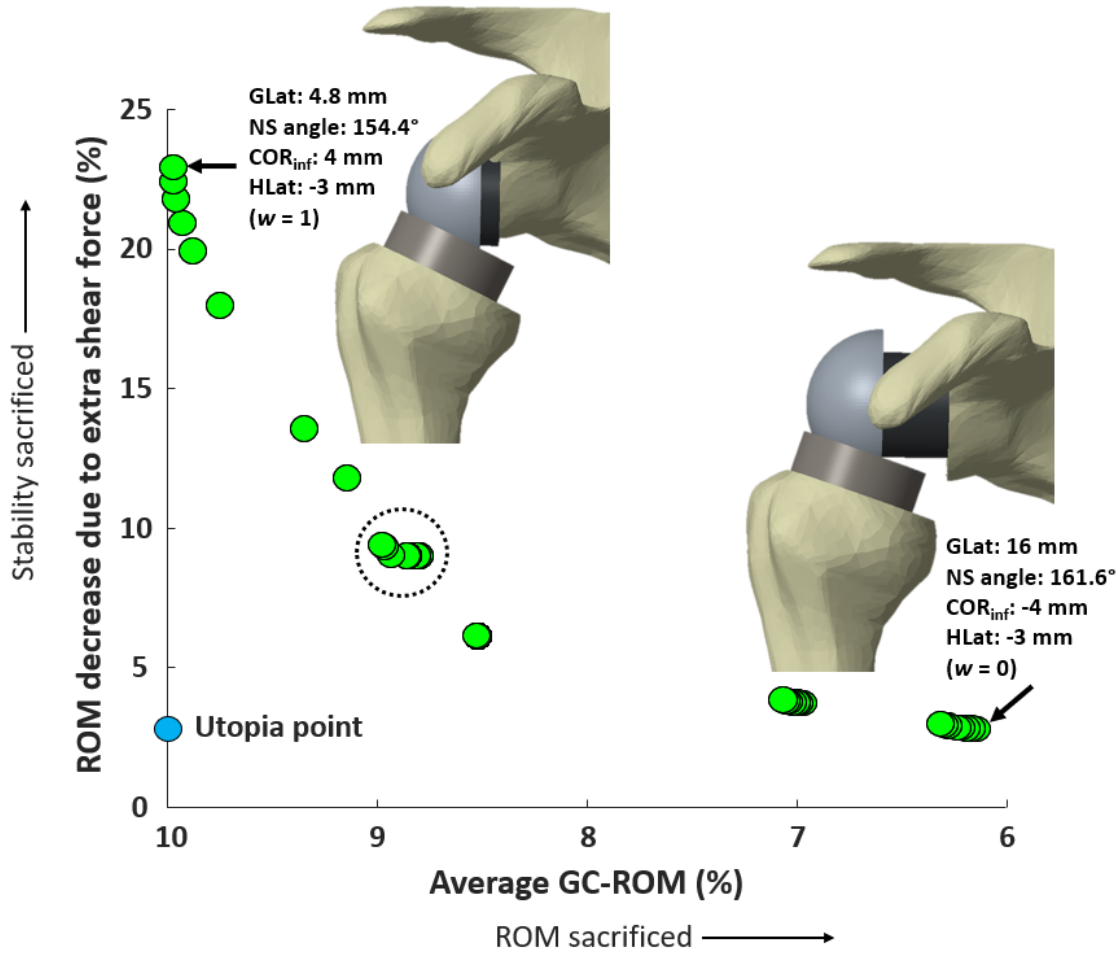

Figure 6.2. The Pareto front with the dominated designs removed and showing design configuration details for the anchor points, which maximize each objective separately. Design configuration details for points enclosed within the dashed circle are shown in Table 6.1.

The design configurations that resulted in intermediate performance of both objectives (represented by the dashed circle in Figure 6.2) are shown in Table 6.1. All designs have maximum COR_{inf} and mid-range NS angles. Interestingly, GLat is either maximized or minimized and values of HLat span from the upper to lower bounds of the variable. In both designs where GLat is minimized, HLat is also minimized, but designs where GLat was maximized, performance was insensitive to HLat (i.e. similar performance for various values of HLat).

Table 6.1. Design configurations that result in intermediate performance for both objectives (those whose performance is represented by the points on the Pareto front within the dashed circle shown in Figure 6.2)

GLat (mm)	*NS angle (°)*	*COR_{inf} (mm)*	*HLat (mm)*
4.8	158.3	-4.0	-3.0
4.8	157.8	-4.0	-3.0
16.0	157.4	-4.0	3.0
16.0	157.4	-4.0	3.0
16.0	154.1	-4.0	-0.3
16.0	154.6	-4.0	0.4
16.0	154.8	-4.0	0.6

As was the case with single objective optimization, it is difficult to elucidate cause-effect relationships of individual design variables in MOO; this is compounded by the multi-faceted nature of GC-ROM, where both passive and active ROM criteria are included. However, general conclusions can be drawn from the results in terms of insight into which combinations of design variables maximize the functional outcomes of rTSA. To maximize stability or ROM separately, the values of GLat and NS angle should be increased or decreased simultaneously. When it comes to central performance in terms of both objectives, it is possible that surgeons are able to choose from multiple implant configurations that are likely to maximize factors such as implant fixation and durability (wear) without sacrificing performance in terms of ROM or stability. It should be noted that factors such as fixation and (wear) were not considered in the present analyses and future work characterizing the effect of implant design on these factors could further inform surgeons' decisions regarding implant selection.

Chapter 7. Summary and Conclusions

In pursuit of the final goal of MOO of rTSA to characterize trade-offs between functional outcomes of the procedure, several precursory objectives were completed, each of which have contributions of their own.

7.1 Development and Validation of Computational Methods Capable of Evaluating Factors Affecting ROM of rTSA

7.1.1 Impingement

Since ROM and stability of rTSA are affected by both passive and active factors, computational methods capable of assessing each were developed and/or validated. The computational model to predict impingement-free ROM was based on performing intersection Boolean operations between the humeral and scapular sides of the joint at any given arm position. Impingement-free ranges predicted by the computational model were experimentally validated for a subset of motions using 3D printed components mounted on a VIVO joint motion simulator.

7.1.2 Muscle Capability

This is the most impactful portion of this objective, as it addresses a limitation in the field of musculoskeletal modeling. Evaluating active factors related to muscle action required the development of an FE model capable of accurately predicting anatomically feasible muscle paths as a function of joint (implant) geometry. Currently, a common

method of determining muscle paths involves calculating the shortest path around rudimentary wrapping geometries representing bony anatomy (i.e. cylinders, spheres, etc.)[97–100]. Although this previous method is more computationally efficient than the presented FE model, using it in an automated setting would be unreliable, where resulting muscle paths may not necessarily always be anatomical feasible within the broad ROM of the shoulder. This is a major drawback related to using this method in conjunction with techniques such as design optimization.

Therefore, the FE model was developed and validated for both an anatomic shoulder and one implanted with rTSA across a range of motions for which data was available in the literature. This ensured that the method was applicable in situations where wrapping geometry is variable and the ranges of motion are broad. Although the method was specifically developed for the purposes of evaluating muscle forces in variable rTSA configurations, it could be applied to analyze other joints/procedures as well. The method may be preferable for situations in which motions/wrapping geometries are complicated and consequently not conducive to using simple wrapping geometries reliably.

7.1.3 Dislocation

The analytical equation adopted for use in evaluating stability of rTSA relates implant geometry, friction coefficient, and compressive force to the shear force required to dislocate the joint. It was previously validated for compressive loading levels of to 200 N. As JCFs in the shoulder have been reported to be higher, the analytical predictions were validated using experimental and FE methods at higher loading levels.

7.2 Development and Implementation of a Novel Metric for Characterizing Implant Performance Related to ROM

Previous methods of characterizing ROM of rTSA have generally relied on the inclusion of motions along a subset of specified paths, for example abduction or flexion, in the context of a single factor passive or active factor. In order to optimize the ROM, a comprehensive metric, GC-ROM, was developed to compare the performance of variable implant configurations in the context of all three limiting factors (impingement, muscle insufficiency, and dislocation) throughout a broad range of motions.

As elevation plane angle and elevation angle are represented by spherical coordinates, binary data representing the feasibility of each position investigated is easily mapped to a sphere. The previously developed computational methods to evaluate each ROM limiting criteria were implemented to determine feasibility of arm positions. The feasible positions were connected to form regions, and GC-ROM was calculated as the average percent surface area of these regions across all included IE rotation angles, each of which was represented by a different sphere.

To ensure the sensitivity of the metric to changes in implant design, GC-ROM was calculated for a subset of implant configurations resulting from combinations of three NS angles and three levels of GLat. Trends in GC-ROM resulting from the successive addition of ROM feasibility criteria were consistent with previous literature, where increasing GLat and NS ultimately increases ROM. It was concluded that a novel, comprehensive metric to characterize implant performance in the context of ROM was developed.

7.3 Maximizing Overall ROM vs ROM for ADL

The natural progression toward MOO was to perform single optimization to maximize ROM of rTSA using the developed computational methods and metric. The selected design variables, GLat, NS angle, COR_{inf} and HLat, were parameterized. Subsequently, the computational pipeline for calculating GC-ROM for a candidate implant design was automated.

Following automation of the pipeline, a single evaluation of the objective function took over two and a half hours, limiting the use of the entire pipeline in optimization. To increase computational efficiency, a surrogate model based on 81 sample designs evaluated using the full model was fit using the response surface method.

In order to characterize potential trade-offs between maximizing different types of motion, the calculation of GC-ROM was broken into six portions, each representing a different motion envelope, and separate surrogate models were fit for each. In this manner, the sum of model predictions was equal to overall GC-ROM (i.e. including all IE rotation and elevation plane angles), but the selection of different combinations of models for use in the optimization problem elucidated designs that maximized different portions of the ROM. It was concluded that similar designs maximized ROM when all elevation plane angles and only negative elevation plane angles were included, regardless of IE rotation angle inclusion.

However, a generally different design maximized motions in forward elevation planes, and required more sacrifices in other envelopes of the overall ROM. This highlights the potential differences in using ROM along certain paths, as the majority of previous studies have done, versus a metric representative of the comprehensive ROM to evaluate

and optimize functional outcomes of rTSA. Different optimum solutions would result from variable methods of characterizing ROM, which should be a consideration in future work.

7.4 Multi-objective Optimization of rTSA

Subsequent to the completion of research objectives 1-3, the only missing piece required to perform MOO was an objective function to characterize stability. Functional stability was defined as the ability of the implant to resist dislocation in the presence of shear JCFs additional to those developed as a result of muscle action. This was defined by calculating the percent of the ROM lost with the inclusion of an extra shear JCF.

The Pareto front was generated using the weighted sum method, varying the weights between 0 and 1 by increments of 0.05, and repeating optimization with 100 random start points at each weight. This resulted in a Pareto front that clearly demonstrated a trade-off between ROM and stability of rTSA, which was hypothesized to exist. Designs maximizing either one of the objectives without regard for the other were similar with regard to two of the design variables, and at opposite ends of the spectrum for the remaining two. Interestingly, the designs which resulted in intermediate performance with respect to both objectives were also variable.

7.5 Limitations and Future Work

7.5.1 Validation of Computational Methods used to Evaluate ROM

Using computational methodologies to assess the ROM of rTSA inherently requires assumptions and simplifications, especially when computationally efficiency is a concern. In the cases related impingement and dislocation resistance (ROM limiting stability), computational models were developed and validated experimentally. Error between the analytical equation, FE model, and experimental predictions of force to dislocation was

amplified at higher compressive loading levels. It appears that the analytical equation leads to an overstated prediction of required force to dislocate a joint. However, given that the method was kept consistent across all scenarios, and additional stabilizing forces would be provided by soft-tissues such as the joint capsule and ligaments, the method was deemed acceptable in terms of analyzing trends in ROM as a function of varying implant design.

The FE model was developed to aid in the prediction of muscle forces by determining muscle paths. The model was validated against available experimental and computational muscle moment arm data for both magnitude and trends as a result of changing joint angle. Although small-scale sensitivity analyses were performed pertaining to selection of model parameters during development, more rigorous investigations of the effect of these selections are warranted. Selections, such as the number and size of the contact spheres, were loosely based on findings in previous work[101,102], but in order to ensure better accuracy of the model, especially in terms of moment arm magnitudes, the effect of such parameters should be studied further.

7.5.2 The Use of Surrogate Models in Objective Function Prediction

The computational cost of evaluating the objective function for ROM of a single candidate rTSA design was too great to implement the full computational pipeline in optimization. Hence, surrogate models were fit to the results from a selection of sample designs representative of the range of each design variable to greatly increase computational efficiency of evaluating the objective function. Using surrogate models in optimization, in lieu of more computationally expensive evaluations, has both benefits and drawbacks. Clearly, the accuracy of the prediction of the real objective function using surrogate models is of concern. A surrogate model was fit to a subset of two implant

parameters and implemented in optimization. Similar analyses should be performed including different combinations of design parameters. Additionally, more sample points could be used to train the model.

The benefit of using surrogate models is that the computational efficiency allows for a comprehensive search of the design space in terms of starting designs for the optimization algorithm. It would be possible to implement the full model in optimization, however it would more difficult to guarantee that globally optimum designs within the ranges of the variables are found in a reasonable timeframe.

7.5.3 Clinical Significance of Objective Functions

The objective functions for characterizing ROM and stability of the joint allowed for the elucidation of trade-offs between the two functional outcomes, but the objective function for stability was highly simplified. Additionally, the clinical significance of differences in performance of varying designs is unclear. However, Simovitch et al.[103] concluded that patients receiving rTSA require less improvement in functional outcomes in order for the procedure to be considered a success, as opposed to those receiving conventional replacements. Future work is warranted in developing a characterization for stability that is more easily interpreted, as well as assess the clinical significance of changes in the objective functions.

7.5.4 Considerations Related to Generalizations Drawn from Results

There are several factors that could affect application of the results presented in this body of work regarding overgeneralized recommendations for optimum rTSA designs. Only a single shoulder was used within the computational pipeline and there is variability in bony anatomy, particularly for the scapula, across different patients[104–106]. Anatomical

variations could have several effects. Smaller scapulae may require the selection of smaller implant components, e.g. the glenosphere, which has been shown to decrease ROM in both abduction and IE rotation[33,107]. Additionally, variations in anatomic measurements such as the tilt of the acromion with respect to the glenoid would likely affect impingent-free motion. It is possible that differences of these sorts may affect the optimum implant design for ROM.

There is also variability in terms of the degree of deficiency in the rotator cuff among different patients, where tears may be full or partial thickness of one or more of the tendons[108]. The remaining functionality of the rotator cuff affects the performance of rTSA, and could potentially influence the relationships between implant design and functional outcomes[29,64,79]. Along the same lines, variable plastic deformation of soft tissues, such as the joint capsule and ligaments, was not accounted for and may affect performance of rTSA, specifically joint stability. The mechanics of the joint, related to the scapulothoracic rhythm, are altered after rTSA[109,110]. The contribution of scapulothoracic motion to arm elevation is increased, and smaller glenohumeral articulations have been observed in comparison to natural anatomy or conventional TSA. However, the underlying mechanisms are not yet well understood. Altered joint mechanics would likely affect the ROM, and potentially stability, of the joint. It is unclear whether this would affect the relative performance of different implant configurations, or the optimum design(s).

Additionally, only a subset of design and surgical parameters were considered. Future work should focus on 1) classifying the effects of variable patient bone geometry and degrees of rotator cuff variability on trade-offs between functional outcomes, 2) investigating the effect of abnormal joint mechanics, and 3) incorporating more design

variables to increase the chances of finding the true optimum design(s). It should be noted however, that the presented computational framework could be adapted to incorporate the effects of the aforementioned uncertainties.

7.6 Conclusions

This work is the first to apply MOO techniques to characterize the trade-offs between functional outcomes of rTSA using a Pareto curve. It was confirmed that there is in fact a previously unconfirmed competing relationship between ROM and stability, such that moving along designs where performance of one metric cannot be improved without detriment to the other.

In order to perform MOO, several sub-objectives were completed, each of which addressed relevant challenges and has future implications. The development of the FE muscle wrapping model allows for prediction of muscle paths and moment arms in the presence of variable joint geometry throughout a broad, complex ROM. It mitigates the unreliably and insensitivity of the most commonly used method of determining muscle path as the shortest geodesic path around simple wrapping geometries. The methodology employed in the FE is widely applicable and could be used to answer a range of clinical questions for which the answers rely partially on muscle paths, moment arms, and forces.

GC-ROM represents a comprehensive metric to characterize performance of rTSA. It allows for the evaluation of rTSA designs throughout the comprehensive ROM considering multiple limiting factors, whereas previous studies have generally characterized implant performance based on single paths of motion in the context of one, sometimes two, of limiting criteria. The use of GC-ROM in maximizing the ranges of various motion envelopes showed that different optimal designs exist based on the desired

motions to be maximized. In other words, the design that maximizes motions most frequently performed in ADL differs from that which maximizes the general, overall ROM.

The computational methodologies and pipeline that were developed to achieve the end goal of MOO may be easily adapted to accommodate 1) variable bone geometries, 2) varying degrees of pre-operative rotator cuff deficiencies, and 3) an expanded list of included implant design and surgical parameters. Thus, a robust basis for future investigations pertaining to rTSA designs that maximize functional outcomes of the procedure in the presence of a wide variety of scenarios is provided.

Bibliography

1. Westermann RW, Pugely AJ, Martin CT, Gao Y, Wolf BR, Hettrich CM. Reverse Shoulder Arthroplasty in the United States: A Comparison of National Volume, Patient Demographics, Complications, and Surgical Indications. *Iowa Orthop J*. 2015;35:1-7.

2. Schairer WW, Nwachukwu BU, Lyman S, Craig E V., Gulotta L V. National utilization of reverse total shoulder arthroplasty in the United States. *J Shoulder Elb Surg*. 2015;24(1):91-97. doi:10.1016/j.jse.2014.08.026.

3. Lippitt SB, Vanderhooft JE, Harris SL, Sidles J a., Harryman DT, Matsen F a. Glenohumeral stability from concavity-compression: A quantitative analysis. *J Shoulder Elb Surg*. 1993;2(1):27-35. doi:10.1016/S1058-2746(09)80134-1.

4. Lippitt SB, Matsen F a. Mechanisms of glenohumeral joint stability. *Clin Orthop Relat Res*. 1993;291:20-28.

5. Speer KP. Anatomy and pathomechanics of shoulder instability. *Clin Sports Med*. 1995;14(4):751-760.

6. Flatow EL, Harrison AK. A history of reverse total shoulder arthroplasty. *Clin Orthop Relat Res*. 2011;469(9):2432-2439. doi:10.1007/s11999-010-1733-6.

7. Jazayeri R, Kwon YW. Evolution of the reverse total shoulder prosthesis. *Bull NYU Hosp Jt Dis*. 2011;69(1):50-55. doi:10.1097/YCO.0000000000000159.

8. Boileau P, Watkinson DJ, Hatzidakis AM, Balg F. Grammont reverse prosthesis: Design, rationale, and biomechanics. *J Shoulder Elb Surg*. 2005;14(1):S147-S161. doi:10.1016/j.jse.2004.10.006.

9. Baulot E, Sirveaux F, Boileau P. Grammont's idea: The story of paul grammont's functional surgery concept and the development of the reverse principle. In: *Clinical Orthopaedics and Related Research*. Vol 469. ; 2011:2425-2431. doi:10.1007/s11999-010-1757-y.

10. Jain NB, Yamaguchi K. The contribution of reverse shoulder arthroplasty to utilization of primary shoulder arthroplasty. *J Shoulder Elb Surg*. 2014;23(12):1905-1912. doi:10.1016/j.jse.2014.06.055.

11. Favard L, Levigne C, Nerot C, Gerber C, De Wilde L, Mole D. Reverse prostheses in arthropathies with cuff tear are survivorship and function maintained over time? *Clin Orthop Relat Res*. 2011;469(9):2469-2475. doi:10.1007/s11999-011-1833-y.

12. Smith CD, Guyver P, Bunker TD. Indications for reverse shoulder replacement: A systematic review. *Bone Joint J*. 2012;94-B(5):577-583. doi:10.1302/0301-620X.94B5.27596.

13. Russo R, Della Rotonda G, Ciccarelli M, Cautiero F. Analysis of complications of reverse total shoulder arthroplasty. *Joints*. 2015;3(2):62-66. doi:10.11138/jts/2015.3.2.062.

14. Zumstein M a., Pinedo M, Old J, Boileau P. Problems, complications, reoperations, and revisions in reverse total shoulder arthroplasty: A systematic review. *J Shoulder Elb Surg*. 2011;20(1):146-157. doi:10.1016/j.jse.2010.08.001.

15. Cheung E, Willis M, Walker M, Clark R, Frankle MA. Complications in Reverse Total Shoulder Arthroplasty. *Jounral Am Acad Orthop Surg*. 2011;19(7):439-449.

16. Roche C, Flurin PH, Wright T, Crosby LA, Mauldin M, Zuckerman JD. An evaluation of the relationships between reverse shoulder design parameters and range of motion, impingement, and stability. *J Shoulder Elb Surg*. 2009;18(5):734-741. doi:10.1016/j.jse.2008.12.008.

17. Shoulder Replacement Vs. Reverse Shoulder Replacement. http://durhamorthopedic.ca/1207-2/. Published 2017.

18. Boileau P, Watkinson D, Hatzidakis AM, Hovorka I. Neer Award 2005: The Grammont reverse shoulder prosthesis: Results in cuff tear arthritis, fracture sequelae, and revision arthroplasty. *J Shoulder Elb Surg*. 2006;15(5):527-540. doi:10.1016/j.jse.2006.01.003.

19. Werner CM, Steinmann PA, Gilbart M, Gerber C. Treatmeant of painful pseudoparesis due to irreparable rotator cuff dysfunction with the Delta III reverse-ball-and-socket prosthesis. *J Bone Jt Surg*. 2005;87(7):1476-1486.

20. Favre P, Loeb MD, Helmy N, Gerber C. Latissimus dorsi transfer to restore external rotation with reverse shoulder arthroplasty: A biomechanical study. *J Shoulder Elb Surg*. 2008;17(4):650-658. doi:10.1016/j.jse.2007.12.010.

21. Kiet TK, Feeley BT, Naimark M, et al. Outcomes after shoulder replacement: Comparison between reverse and anatomic total shoulder arthroplasty. *J Shoulder Elb Surg*. 2015;24(2):179-185. doi:10.1016/j.jse.2014.06.039.

22. Human Anatomy Planes. http://baldaivirtuves.info/human-anatomy-planes/human-anatomy-planes-3-anatomical-planes-of-the-human-body-4-health/.

23. Doorenbosch CAM, Harlaar J, Veeger D (H. EJ. The globe system: An

unambiguous description of shoulder positions in daily life movements. *J Rehabil Res Dev*. 2003;40(2):149. doi:10.1682/JRRD.2003.03.0149.

24. Holzbaur KRS, Murray WM, Delp SL. A model of the upper extremity for simulating musculoskeletal surgery and analyzing neuromuscular control. *Ann Biomed Eng*. 2005;33(6):829-840. doi:10.1007/s10439-005-3320-7.

25. Shoulder muscles that move the arm. http://digikalla.info/muscles-shoulder/muscles-shoulder-muscles-that-move-the-arm/.

26. Matsen F. Shoulder Arthritis/Rotator Cuff Tears: causes of shoulder pain. http://shoulderarthritis.blogspot.com/2011/08/rotator-cuff-2-clinical-considerations.html. Published 2011.

27. Katz D, O'Toole G, Cogswell L, Sauzieres P, Valenti P. A history of the reverse shoulder prosthesis. *Ijss*. 2007;1(4):108-113.

28. Neer CSI. *Shoulder Reconstruction*. Philadelphia: Saunders; 1990.

29. Middernacht B, Van Tongel A, De Wilde L. A Critical Review on Prosthetic Features Available for Reversed Total Shoulder Arthroplasty. *Biomed Res Int*. 2016;2016:1-9. doi:10.1155/2016/3256931.

30. Kontaxis A, Johnson GR. Clinical Biomechanics The biomechanics of reverse anatomy shoulder replacement – A modelling study. *Clin Biomech*. 2009;24(3):254-260. doi:10.1016/j.clinbiomech.2008.12.004.

31. Nyffeler RW, Werner CML, Gerber C. Biomechanical relevance of glenoid component positioning in the reverse Delta III total shoulder prosthesis. *J Shoulder Elb Surg*. 2005;14(5):524-528. doi:10.1016/j.jse.2004.09.010.

32. Gutiérrez S, Levy JC, Frankle MA, et al. Evaluation of abduction range of motion and avoidance of inferior scapular impingement in a reverse shoulder model. *J Shoulder Elb Surg*. 2008;17(4):608-615. doi:10.1016/j.jse.2007.11.010.

33. Gutiérrez S, Comiskey CAI, Luo ZP, Pupello DR, Frankle M. Range of impingement-free abduction and adduction deficit after reverse shoulder arthroplasty. *J Bone Jt Surg*. 2008;90(12):2606-2615.

34. Gutiérrez S, Luo ZP, Levy J, Frankle MA. Arc of motion and socket depth in reverse shoulder implants. *Clin Biomech*. 2009;24(6):473-479. doi:10.1016/j.clinbiomech.2009.02.008.

35. Virani NA, Cabezas A, Gutiérrez S, Santoni BG, Otto R, Frankle M. Reverse shoulder arthroplasty components and surgical techniques that restore glenohumeral motion. *J Shoulder Elb Surg*. 2013;22(2):179-187. doi:10.1016/j.jse.2012.02.004.

36. De Wilde LF, Poncet D, Middernacht B, Ekelund A. Prosthetic overhang is the most effective way to prevent scapular conflict in a reverse total shoulder prosthesis. *Acta Orthop*. 2010;81(6):719-726. doi:10.3109/17453674.2010.538354.

37. Oh JH, Shin SJ, McGarry MH, Scott JH, Heckmann N, Lee TQ. Biomechanical effects of humeral neck-shaft angle and subscapularis integrity in reverse total shoulder arthroplasty. *J Shoulder Elb Surg*. 2014;23(8):1091-1098. doi:10.1016/j.jse.2013.11.003.

38. Werner BS, Chaoui J, Walch G. The influence of humeral neck shaft angle and glenoid lateralization on range of motion in reverse shoulder arthroplasty. *J Shoulder Elb Surg*. 2017;26(10):1726-1731. doi:10.1016/j.jse.2017.03.032.

39. Keener JD, Patterson BM, Orvets N, Aleem AW, Chamberlain AM. Optimizing reverse shoulder arthroplasty component position in the setting of advanced arthritis with posterior glenoid erosion: a computer-enhanced range of motion analysis. *J Shoulder Elb Surg*. 2018;27(2):339-349. doi:10.1016/j.jse.2017.09.011.

40. Gutiérrez S, Levy J, Lee WE, Keller TS, Maitland ME. Center of rotation affections abduction range of motion of reverse shoulder arthroplasty. *Clin Orthop Relat Res*. 2007;458:78-82.

41. Clouthier AL, Hetzler M a., Fedorak G, Bryant JT, Deluzio KJ, Bicknell RT. Factors affecting the stability of reverse shoulder arthroplasty: A biomechanical study. *J Shoulder Elb Surg*. 2013;22(4):439-444. doi:10.1016/j.jse.2012.05.032.

42. Favre P, Sussmann PS, Gerber C. The effect of component positioning on intrinsic stability of the reverse shoulder arthroplasty. *J Shoulder Elb Surg*. 2010;19(4):550-556. doi:10.1016/j.jse.2009.11.044.

43. Gutiérrez S, Keller TS, Levy JC, Lee WE, Luo ZP. Hierarchy of stability factors in reverse shoulder arthroplasty. *Clin Orthop Relat Res*. 2008;466(3):670-676. doi:10.1007/s11999-007-0096-0.

44. Anderson FC, Pandy MG. Static and dynamic optimization solutions for gait are practically equivalent. *J Biomech*. 2001;34(2):153-161. doi:10.1016/S0021-9290(00)00155-X.

45. Lin Y-C, Dorn TW, Schache AG, Pandy MG. Comparison of different methods for estimating muscle forces in human movement. *Proc Inst Mech Eng Part H J Eng Med*. 2011;226(2):103-112.

46. van Bolhuis BM, Gielen CC. A comparison of models explaining muscle activation patterns for isometric contractions. *Biol Cybern*. 1999;81(3):249-261. doi:10.1007/s004220050560.

47. Crowninshield RD, Brand RA. A phyisiologically based criterion of muscle force

prediction in locomotion. *J Biomech*. 1981;14(11):793-801.

48. Collins JJ. The redundant nature of locomotor optimization laws. *J Biomech*. 1995;28(3):251-267.

49. Li G, Kaufman KR, Chao EY, Rubash HE. Prediction of antagonistic muscle forces using inverse dynamic optimization during flexion/extension of the knee. *J Biomech Eng*. 1999;121(3):316-322.

50. Raikova RT, Prilutsky BI. Sensitivity of predicted muscle forces to parameters of the optimization-based human leg model revealed by analytical and numerical analyses. *J Biomech*. 2001;34(10):1243-1255. doi:10.1016/S0021-9290(01)00097-5.

51. Delp SL, Anderson FC, Arnold AS, et al. OpenSim: Open source to create and analyze dynamic simulations of movement. *IEEE Trans Biomed Eng*. 2007;54(11):1940-1950. doi:10.1109/TBME.2007.901024.

52. Seth A, Sherman M, Reinbolt JA, Delp SL. OpenSim: A musculoskeletal modeling and simulation framework for in silico investigations and exchange. *Procedia IUTAM*. 2011;2:212-232. doi:10.1016/j.piutam.2011.04.021.

53. De Groot JH, Brand R. A three-dimensional regression model of the shoulder rhythm. *Clin Biomech*. 2001;16(9):735-743. doi:10.1016/S0268-0033(01)00065-1.

54. Wu G, Van Der Helm FCT, Veeger HEJ, et al. ISB recommendation on definitions of joint coordinate systems of various joints for the reporting of human joint motion - Part II: Shoulder, elbow, wrist and hand. *J Biomech*. 2005;38(5):981-992. doi:10.1016/j.jbiomech.2004.05.042.

55. Bezerra MA, Santelli RE, Oliveira EP, Villar LS, Escaleira LA. Response surface methodology (RSM) as a tool for optimization in analytical chemistry. *Talanta*. 2008;76(5):965-977. doi:10.1016/j.talanta.2008.05.019.

56. Alvarez L. Design Optimization based on Genetic Programming. 2000.

57. Ahrens J, Law C, Geveci B, James Ahrens, Charles L. B. Geveci. Paraview: An end user tool for large data visualization. *Vis Handb*. 2005;836:717-731. doi:10.1016/B978-012387582-2/50038-1.

58. Ayachit U. *The ParaView Guide: A Parallel Visualization Application*. USA: Kitware, Inc.; 2015.

59. DePuy Synthes Joint Reconstruction. Delta Xtend Reverse Shoulder System Surgical Technique. 2013. http://synthes.vo.llnwd.net/o16/LLNWMB8/INT Mobile/Synthes International/Product Support Material/legacy_DePuy_PDFs/DPEM-ORT-1112-0336_9072-78-065_LR.pdf.

60. Webb JD, Blemker SS, Delp SL. 3D Finite Element Models of Shoulder Muscles for Computing Lines of Actions and Moment Arms. *Comput Methods Biomech Biomed Engin*. 2014;17(8):829-837. doi:10.1111/j.1747-0285.2012.01428.x.Identification.

61. Ackland DC, Pak P, Richardson M, Pandy MG. Moment arms of the muscles crossing the anatomical shoulder. *J Anat*. 2008;213(4):383-390. doi:10.1111/j.1469-7580.2008.00965.x.

62. Favre P, Gerber C, Snedeker JG. Automated muscle wrapping using finite element contact detection. *J Biomech*. 2010;43(10):1931-1940. doi:10.1016/j.jbiomech.2010.03.018.

63. Gatti CJ, Dickerson CR, Chadwick EK, Mell AG, Hughes RE. Comparison of model-predicted and measured moment arms for the rotator cuff muscles. *Clin Biomech*. 2007;22(6):639-644. doi:10.1016/j.clinbiomech.2007.02.001.

64. Hamilton MA, Roche CP, Diep P, Flurin PH, Routman HD. Effect of prosthesis design on muscle length and moment arms in reverse total shoulder arthroplasty. *Bull NYU Hosp Jt Dis*. 2013;71(SUPPL. 2):31-35.

65. Ackland DC, Pandy MG. Moment arms of the shoulder muscles during axial rotation. *J Orthop Res*. 2011;29(5):658-667. doi:10.1002/jor.21269.

66. Ackland DC, Roshan-Zamir S, Richardson M, Pandy MG. Moment Arms of the Shoulder Musculature After Reverse Total Shoulder Arthroplasty. *J Bone Jt Surgery-American Vol*. 2010;92(5):1221-1230. doi:10.2106/JBJS.I.00001.

67. Dc A, Richardson M, Mg P. Axial Rotation Moment Arms of the Shoulder after Reverse Total Arthroplasty. *J Bone Jt Surg*. 2012;94:1886-1895. doi:10.2106/JBJS.J.01861.

68. Anglin C, Wyss UP, Pichora DR. Shoulder prosthesis subluxation: Theory and experiment. *J Shoulder Elb Surg*. 2000;9(2):104-114. doi:10.1067/mse.2000.105139.

69. Costantini O, Choi DS, Kontaxis A, Gulotta L V. The effects of progressive lateralization of the joint center of rotation of reverse total shoulder implants. *J Shoulder Elb Surg*. 2015;24(7):1120-1128. doi:10.1016/j.jse.2014.11.040.

70. Giles JW, Langohr GDG, Johnson JA, Athwal GS. Implant Design Variations in Reverse Total Shoulder Arthroplasty Influence the Required Deltoid Force and Resultant Joint Load. *Clin Orthop Relat Res*. 2015;473(11):3615-3626. doi:10.1007/s11999-015-4526-0.

71. AISI Type 304 Stainless Steel. http://asm.matweb.com/search/SpecificMaterial.asp?bassnum=mq304a.

72. Kurtz SM. *The UHMWPE Handbook: Ultra-High Molecular Weight Polyethylene in Total Joint Replacement*. Elsevier Science & Technology Books; 2004.

73. Corporation RP. REDCO UHMW. https://www.redwoodplastics.com/brochures/uhmw-engineering-data.pdf.

74. Schutte LM, Rodgers MM, Zajac FE, Glaser RM. Improving the efficacy of electrical stimulation-induced leg cycle ergometry: an analysis based on a dynamic musculoskeletal model. *IEEE Trans Rehabil Eng*. 1993;1:109-125.

75. Millard M, Uchida T, Seth A, Delp SL. Flexing computational muscle: modeling and simulation of musculotendon dynamics. *J Biomech Eng*. 2013;135(2):21005. doi:10.1115/1.4023390.

76. Hoenecke HR, Flores-Hernandez C, D'Lima DD. Reverse total shoulder arthroplasty component center of rotation affects muscle function. *J Shoulder Elb Surg*. 2014;23(8):1128-1135. doi:10.1016/j.jse.2013.11.025.

77. Liou W, Yang Y, Petersen-Fitts GR, Lombardo DJ, Stine S, Sabesan VJ. Effect of lateralized design on muscle and joint reaction forces for reverse shoulder arthroplasty. *J Shoulder Elb Surg*. 2017;26(4):564-572. doi:10.1016/j.jse.2016.09.045.

78. Henninger HB, Barg A, Anderson AE, Bachus KN, Burks RT, Tashjian RZ. Effect of lateral offset center of rotation in reverse total shoulder arthroplasty: a biomechanical study. *J Shoulder Elb Surg*. 2012;21(9):1128-1135. doi:10.1016/j.jse.2011.07.034.

79. Greiner S, Schmidt C, König C, Perka C, Herrmann S. Lateralized reverse shoulder arthroplasty maintains rotational function of the remaining rotator cuff shoulder. *Clin Orthop Relat Res*. 2013;471(3):940-946. doi:10.1007/s11999-012-2692-x.

80. Greiner S, Schmidt C, Herrmann S, Pauly S, Perka C. Clinical performance of lateralized versus non-lateralized reverse shoulder arthroplasty: a prospective randomized study. *J Shoulder Elbow Surg*. 2015;24(9):1397-1404. doi:10.1016/j.jse.2015.05.041.

81. Langohr GDG, Willing R, Medley JB, Athwal GS, Johnson JA. Contact mechanics of reverse total shoulder arthroplasty during abduction: The effect of neck-shaft angle, humeral cup depth, and glenosphere diameter. *J Shoulder Elb Surg*. 2016;25(4):589-597. doi:10.1016/j.jse.2015.09.024.

82. Lévigne C, Boileau P, Favard L, et al. Scapular notching in reverse shoulder arthroplasty. *J Shoulder Elb Surg*. 2008;17(6):925-935. doi:10.1016/j.jse.2008.02.010.

83. Nicholson GP, Strauss EJ, Sherman SL. Scapular Notching: Recognition and

Strategies to Minimize Clinical Impact. *Clin Orthop Relat Res*. 2011;469(9):2521-2530. doi:10.1007/s11999-010-1720-y.

84. Nyffeler RW, Werner CML, Simmen BR, Gerber C. Analysis of a retrieved Delta III total shoulder prosthesis. *J Bone Jt Surg*. 2004;86(8):1187-1191. doi:10.1302/0301-620X.86B8.15228.

85. Willing R. Multiobjective design optimization of total knee replacements considering UHMWPE wear and kinematics. 2010;NR65119(April):232. http://search.proquest.com/docview/762223723?accountid=37552.

86. Jr HRH, Flores-Hernandez C, Lima DDD, Hoenecke HR, Flores-Hernandez C, D'Lima DD. Reverse total shoulder arthroplasty component center of rotation affects muscle function. *J Shoulder Elb Surg*. 2014;23(8):1128-1135. doi:10.1016/j.jse.2013.11.025.

87. Boileau P, Moineau G, Roussanne Y, O'Shea K. Bony increased-offset reversed shoulder arthroplasty minimizing scapular impingement while maximizing glenoid fixation. *Clin Orthop Relat Res*. 2011;469(9):2558-2567. doi:10.1007/s11999-011-1775-4.

88. Athwal GS, MacDermid JC, Reddy KM, Marsh JP, Faber KJ, Drosdowech D. Does bony increased-offset reverse shoulder arthroplasty decrease scapular notching? *J Shoulder Elb Surg*. 2015;24(3):468-473. doi:10.1016/j.jse.2014.08.015.

89. Chan K, Langohr GDG, Mahaffy M, Johnson JA, Athwal GS. Does Humeral Component Lateralization in Reverse Shoulder Arthroplasty Affect Rotator Cuff Torque? Evaluation in a Cadaver Model. *Clin Orthop Relat Res*. 2017;475(10):2564-2571. doi:10.1007/s11999-017-5413-7.

90. Langohr GDG, Haverstock JP, Johnson JA, Athwal GS. Comparing daily shoulder motion and frequency after anatomic and reverse shoulder arthroplasty. *J Shoulder Elb Surg*. 2018;27(2):325-332. doi:10.1016/j.jse.2017.09.023.

91. Hamilton MA, Diep P, Roche C, et al. Effect of reverse shoulder design philosophy on muscle moment arms. *J Orthop Res*. 2015;33(4):605-613. doi:10.1002/jor.22803.

92. Henninger HB, King FK, Tashjian RZ, Burks RT. Biomechanical comparison of reverse total shoulder arthroplasty systems in soft tissue – constrained shoulders. *J Shoulder Elb Surg*. 2014;23(5):e108-e117. doi:10.1016/j.jse.2013.08.008.

93. Walker DR, Kinney AL, Wright TW, Banks SA. How sensitive is the deltoid moment arm to humeral offset changes with reverse total shoulder arthroplasty? *J Shoulder Elb Surg*. 2016;25(6):998-1004. doi:10.1016/j.jse.2015.10.028.

94. Elwell J, Choi J, Willing R. Quantifying the competing relationship between

adduction range of motion and baseplate micromotion with lateralization of reverse total shoulder arthroplasty. *J Biomech*. 2017;52:24-30. doi:10.1016/j.jbiomech.2016.11.053.

95. Harman M, Frankle M, Vasey M, Banks S. Initial glenoid component fixation in "reverse" total shoulder arthroplasty: A biomechanical evaluation. *J Shoulder Elb Surg*. 2005;14(1):S162-S167. doi:10.1016/j.jse.2004.09.030.

96. Hettrich CM, Permeswaran VN, Goetz JE, Anderson DD. Mechanical tradeoffs associated with glenosphere lateralization in reverse shoulder arthroplasty. *J Shoulder Elb Surg*. 2015;24(11):1774-1781. doi:10.1016/j.jse.2015.06.011.

97. Garner BA, Pandy MG. The Obstacle-Set Method for Representing Muscle Paths in Musculoskeletal Model. *Comput Methods Biomech Biomed Engin*. 2000;3(1):1-30.

98. Delp SL, Loan JP. A Computational Framework for Simluating and Analyzing Human and Animal Movement. *Comput Sci Eng*. 2000;2(5):46-55.

99. Steenbrink F, de Groot JH, Veeger HEJ, van der Helm FCT, Rozing PM. Glenohumeral stability in simulated rotator cuff tears. *J Biomech*. 2009;42(11):1740-1745. doi:10.1016/j.jbiomech.2009.04.011.

100. Charlton IW, Johnson GR. Application of spherical and cylindrical wrapping algorithms in a musculoskeletal model of the upper limb. *J Biomech*. 2001;34(9):1209-1216. doi:10.1016/S0021-9290(01)00074-4.

101. Scholz A, Sherman M, Stavness I, Delp S, Kecskeméthy A. A fast multi-obstacle muscle wrapping method using natural geodesic variations. *Multibody Syst Dyn*. 2016;36(2):195-219. doi:10.1007/s11044-015-9451-1.

102. Meyer DC, Rahm S, Farshad M, Lajtai G, Wieser K. Deltoid muscle shape analysis with magnetic resonance imaging in patients with chronic rotator cuff tears. *BMC Musculoskelet Disord*. 2013;14(1):1. doi:10.1186/1471-2474-14-247.

103. Simovitch R, Flurin P-H, Wright T, Zuckerman JD, Roche CP. Quantifying success after total shoulder arthroplasty: the minimal clinically important difference. *J Shoulder Elb Surg*. 2018;27(2):298-305. doi:10.1016/j.jse.2017.09.013.

104. Torrens C, Corrales M, Gonzalez G, Solano A, Cáceres E. Cadaveric and three-dimensional computed tomography study of the morphology of the scapula with reference to reversed shoulder prosthesis. *J Orthop Surg Res*. 2008;3(1):1-8. doi:10.1186/1749-799X-3-49.

105. von Schroeder HP, Kuiper SD, Botte MJ. Osseous anatomy of the scapula. *Clin Orthop Relat Res*. 2001;383:131-139.

106. Middernacht B, De Roo PJ, Van Maele G, De Wilde LF. Consequences of scapular anatomy for reversed total shoulder arthroplasty. *Clin Orthop Relat Res*. 2008;466(6):1410-1418. doi:10.1007/s11999-008-0187-6.

107. Berhouet J, Garaud P, Favard L. Influence of glenoid component design and humeral component retroversion on internal and external rotation in reverse shoulder arthroplasty: A cadaver study. *Orthop Traumatol Surg Res*. 2013;99(8):887-894. doi:10.1016/j.otsr.2013.08.008.

108. Patte D. Classification of rotator cuff lesions. *Clin Orthop Relat Res*. 1990;254:81-86.

109. Mahnic J, Toledo D, Fagundes J, et al. Clinical Biomechanics Kinematic evaluation of patients with total and reverse shoulder arthroplasty during rehabilitation exercises with different loads. *JCLB*. 2012. doi:10.1016/j.clinbiomech.2012.04.009.

110. Favard L, Guery J, Bicknell Rbacle G, Berhouet J. A radiokinematic study of the Grammont reverse shoulder prosthesis. In: Walch G, Boileau P, Mole D, Favard L, Levigne C, Sirveaux F, eds. *Reverse Shoulder Arthroplasty*. Montpellier, France: Sauramps Medical; 2006:57-68.